Dynamics and Control of a Piano Action Mechanism

by

Adel Izadbakhsh

A thesis
presented to the University of Waterloo
in fulfilment of the
thesis requirement for the degree of
Master of Applied Science
in
Systems Design Engineering

Waterloo, Ontario, Canada, 2006

I hereby declare that I am the sole author of this thesis.

I authorize the University of Waterloo to lend this thesis to other institutions or individuals for the purpose of scholarly research.

I further authorize the University of Waterloo to reproduce this thesis by photocopying or by other means, in total or in part, at the request of other institutions or individuals for the purpose of scholarly research.

Abstract

The piano action is the mechanism that transforms the finger force applied to a key into the motion of a hammer that strikes a piano string. This thesis focuses on improving the fidelity of the dynamic model of a grand piano action which has been already developed by Hirschkorn et al. at the University of Waterloo. This model is the state-of-the-art dynamic model of the piano in the literature and is based on the real components of the piano action mechanism (key, whippen, jack, repetition lever, and hammer). Two main areas for improving the fidelity of the dynamic model are the hammer shank and the connection point between the key and the ground.

The hammer shank is a long narrow wooden rod and, by observation with a high-speed video camera, the flexibility of this part has been confirmed. In previous work, the piano hammer had been modelled as a rigid body. In this work, a Rayleigh beam model is used to model the flexible behaviour of the hammer shank. By comparing the experimental and analytical results, it turns out that the flexibility of the hammer shank does not significantly affect the rotation of the other parts of the piano mechanism, compared with the case that the hammer shank has been modelled as a rigid part. However, the flexibility of the hammer shank changes the impact velocity of the hammer head, and also causes a greater scuffing motion for the hammer head during the contact with the string.

The connection of the piano key to the ground had been simply modelled with a revolute joint, but the physical form of the connection at that point suggests that a revolute-prismatic joint with a contact force underneath better represents this connection. By comparing the experimental and analytical results, it is concluded that incorporating this new model significantly increases the fidelity of the model for the blows.

In order to test the accuracy of the dynamic model, an experimental setup, including a servo motor, a load cell, a strain gauge, and three optical encoders, is built. The servo motor is used to actuate the piano key. Since the purpose of the motor is to consistently mimic the finger force of the pianist, the output torque of the motor is controlled. To overcome the problem associated with the motor torque control method used in previous work, a new torque control method is implemented on a real-time PC and a better control of the motor torque output is established.

Adding a more realistic model of the piano string to the current piano action model and

finding a better contact model for the contacts that happen between the surfaces that are made of felt (or leather), are two main areas that can be worked on in the future research. These two areas will help to further increase the fidelity of the present piano action model.

Acknowledgements

First, I would like to especially thank my supervisors Prof. John McPhee and Prof. Stephen Birkett, for granting me such a great opportunity to come to the University of Waterloo, work on this fantastic project, and for providing great support throughout.

I would like to thank *Steinway and Sons*, New York, for collaborating on the project.

Mr. Martin Hirschkorn is thanked for his generous help and technical support throughout my Master's program.

Tanya Matthews is acknowledged for her efforts in expediting my admission process. Without her, the start of my Master's program would have probably been postponed for one term.

Finally, I'd like to thank my family and Niloufar for their support, who always kept me inspired for constant pursuit of knowledge.

To Niloufar

Contents

List of Tables

List of Figures

Chapter 1

Introduction and Literature Review

1.1 Introduction

The piano action is the mechanism that transforms the finger force applied to a key, into a motion of a hammer that strikes a piano string. Besides carrying the force from the key to the string, this mechanism allows the pianists to control the amount of force they want to transfer to the piano string. The action mechanisms of the different brands of pianos have the same basic shape, but the material that has been used in them and their dimensions are slightly different. The feel and performance of a typical piano, to a great extent, is related to the design of its piano action. To identify the important geometric and material parameters of the action and their effects on the feel and performance of a typical piano, the piano maker of that piano needs a high-fidelity design tool for the action mechanism. By keeping the identified important parameters of the action mechanism constant in the manufacturing process, all of the manufactured pianos (with the same brand) will have the same feel and performance. Therefore, a high-fidelity design tool for the action mechanism is pivotal for piano makers. A very good mechanistic dynamic model of the piano action mechanism has been developed by Hirschkorn et al. [1] at the University of Waterloo. Their model was based on an action mechanism of the Boston GP-178 grand piano, which is depicted in Figure 1.1. There is still some room for improvement in their model, particularly the flexibility of the hammer shank and the connection of the piano key to the ground, which this thesis addresses.

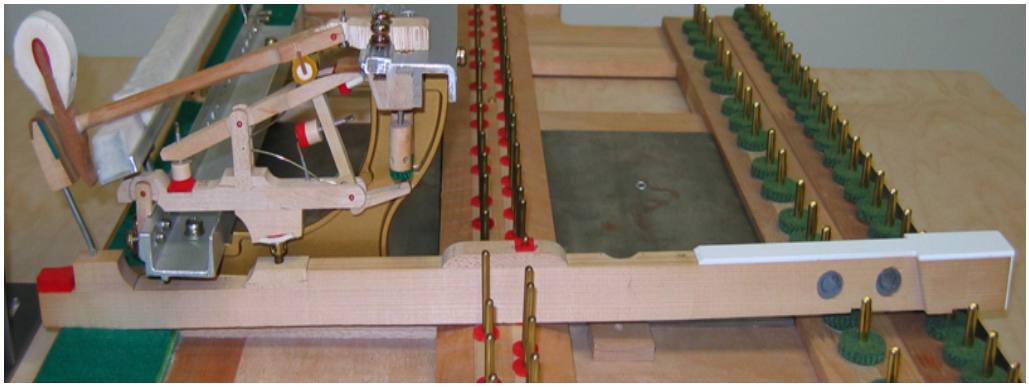

Figure 1.1: Action Mechanism of the Boston GP-178 Grand Piano

Including the biomechanical aspect to the dynamic model of the piano action is also important and in order to take the first step toward that purpose, the pianist finger force, as the input to the piano action model, is replaced by the displacement of the last bone of the fingertip.

Since the input of the piano action model is the pianist finger force, in the previous experimental setup used to validate the piano model [2], the motor is run in the torque control mode. Since there were some problems associated with that torque control method [32], a new method[1] for running the motor in the torque control mode on a real-time PC is developed.

1.2 Action Mechanism

An exploded view of the piano action mechanism, used in this thesis, is shown in Figure 1.2. The key, whippen, jack, repetition lever, and hammer are the five main parts of the mechanism. The key rests on a balance rail at its middle.

As shown in Figure 1.3 (a), for each key, there is a vertical peg attached to the balance rail that passes through the hole in the key. For the key to freely rotate around the balance rail, there is enough backlash between the peg and the key hole. Also, as shown in Figure 1.3 (b), to minimize the lateral motion of the key, another vertical peg at the front rail

[1]Explained in Section 2.5.

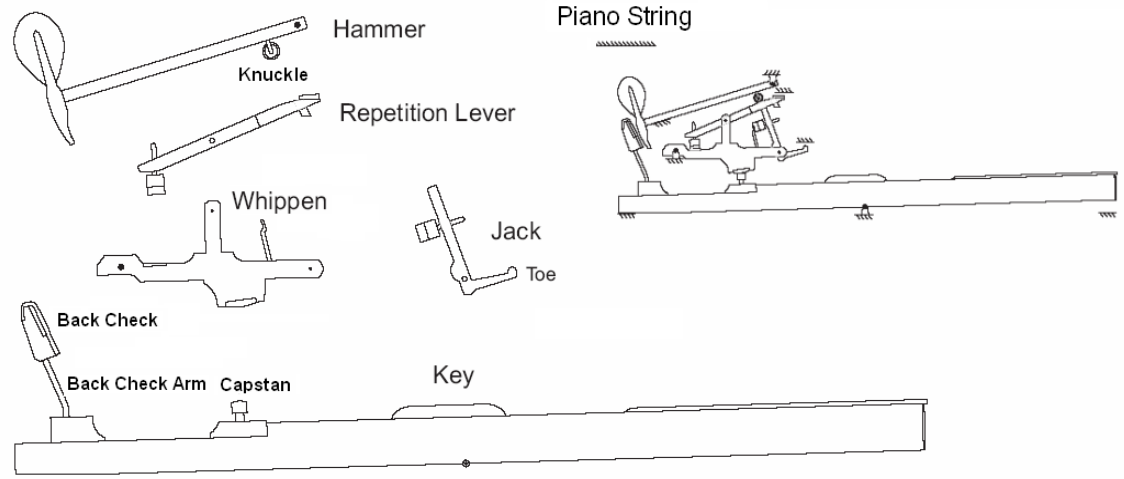

Figure 1.2: Components of the Boston GP-178 Grand Piano Action Mechanism

(a) (b)

Figure 1.3: (a) Connection of the Piano Key to the Balance Rail (b) Connection of the Key Front to the Front Rail

goes into a hole at the bottom of the key front.

Figure 1.4 shows that the whippen and the hammer are connected to the ground with pin joints, and the jack and the repetition lever are joined to the whippen with pin joints. The collection of the whippen, jack, and repetition lever is called the *whippen assembly*.

As the front of the key is pressed by the pianist, the key starts to rotate clockwise around

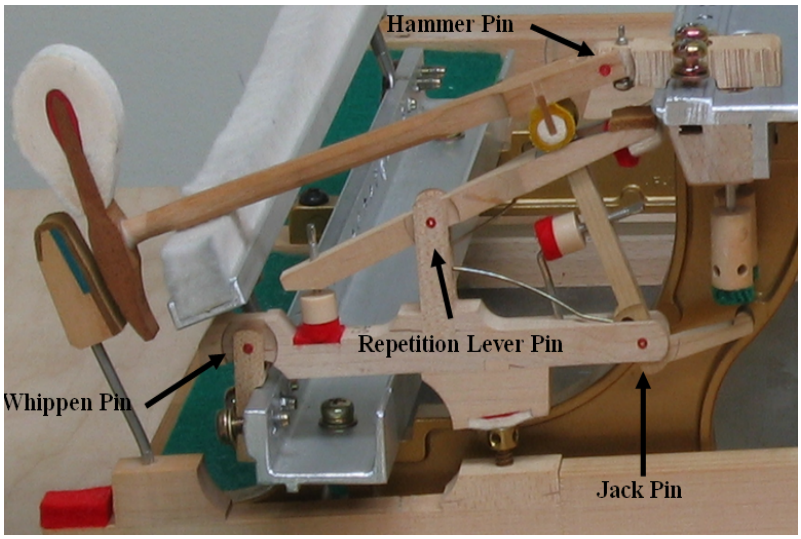

Figure 1.4: Location of the Pins in the Action Mechanism

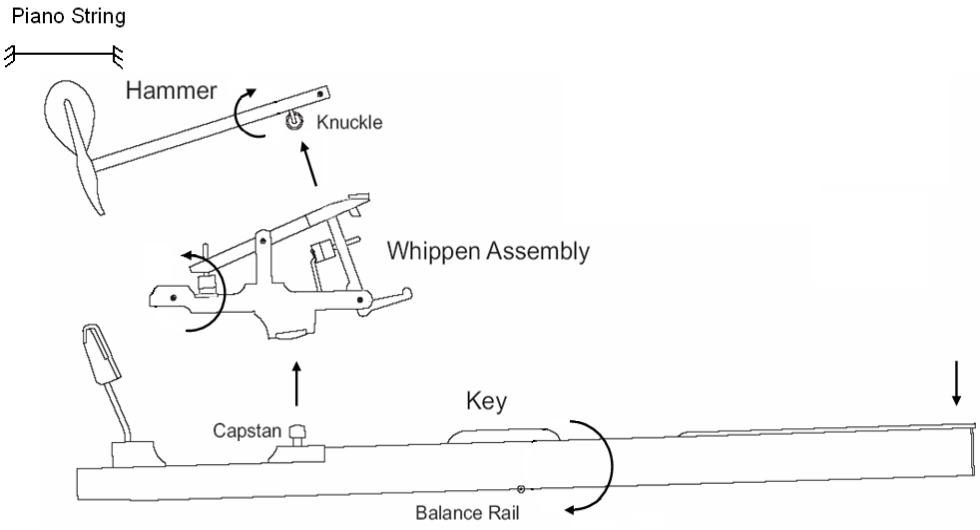

Figure 1.5: Rotation Sequence in a Piano Action Mechanism

its resting point on the balance rail. As a result, the capstan moves upward and presses on the bottom of the whippen assembly. Then, the whippen assembly rotates counter-clockwise and pushes up the knuckle of the hammer, causing it to rotate and strike the piano string (shown in Figure 1.5).

The jack and the repetition lever have specific functionalities. Once the hammer strikes the piano string, the hammer should not remain in contact with the string and it must bounce off, immediately. This requirement of the piano action is called *escapement* and the jack provides this. When the key is depressed, the jack transfers the force from the whippen to the hammer. When the hammer is only 1 mm from the string, the end of the horizontal arm of the jack (the toe) hits a fixed stop, causing the jack to rotate clockwise and detach from the knuckle. This allows the hammer to fly freely and fall back from the string, while the key is still fully depressed. Then, the hammer is caught at the *back check* (which has a high coefficient of friction) and is prevented from bouncing back and re-striking the hammer.

A piano action should also have a *repetition mechanism*, allowing repeated strikes on the key. Once the hammer has escaped, it is no longer moving with the key. Releasing the key must re-latch the hammer to allow successive strikes. This requirement is satisfied by the repetition lever. Once the note is complete, by partially releasing the key, the hammer is released from the back check and held up by the repetition lever so that, the hammer is 3 mm away from the string. At the same time, the jack moves away from the fixed stop and falls back under the knuckle.

1.3 Literature Review

1.3.1 Piano Action Modelling

Although a piano is an expensive musical instrument, there is not much research on the dynamic modelling of the piano action mechanism reported in the literature[2]. Dynamic phenomena, such as the contact and friction that exist at the different locations of the action mechanism, are so complex that modelling the action mechanism is a very difficult

[2]Major parts of the material in this section are taken from [2].

task. Of all the dynamic models available for the piano action mechanism in the literature, only the model by Hirschkorn et al. [1] is considered to be a solid mechanistic model for the contacts between the different bodies in the piano action mechanism (other dynamic models use kinematic constraints to represent the contact). For completeness, however, a concise description of all the work done is summarized as follows.

In 1921, Pfeiffer performed one of the first analyses of the piano action [15]. He conducted extensive analytical investigations of the various actions and components, and identified how changes to certain parameters affected both the kinematic and dynamic characteristics of the action. Since he used a very simple dynamic model based on conservation of energy, his sensitivity analysis was fairly rough. Also, he could not experimentally validate his model.

Matveev and Rimsky-Korsakov, in 1937 [16], initiated one of the earliest attempts to model the piano action. They simplified the action to a one-dimensional mechanism which had two masses connected by a spring. One mass represents the hammer, and the other represents the key and the whippen assembly. His model could fairly predict the general behaviour of the grand pianos.

In 1972, Oledzki reviewed this model again [17]. He observed a qualitative difference between the model results and the behaviour of an upright piano action. To improve the prediction of this model, he replaced the constant mass of the key with a variable mass, which changed with the position of the key.

In 1987, Topper and Wills [18] proposed a more advanced model, consisting of two rotating bodies interconnected by a spring. The two bodies represent the key and hammer, and the spring represents the compliance in the whippen. The parameters in Topper and Wills's model were determined through direct measurements of the action components; however, to obtain good agreement with the experimental data of a real action, model parameters eventually had to be re-calibrated. Once re-calibrated, the model could predict the down-stroke motion of the action, well.

In 1992, Gillespie [19] modelled the action using four bodies representing the key, whippen, jack, and hammer. The model used rigid bodies, connected by kinematic constraints. There was no friction, damping, or compliance in the bodies. Although, he did not consider all the features of a piano action in his model, by tuning the values of his model parameters

he was able to obtain a fairly good agreement between his model and experimental results.

In 1996, Gillespie in his Ph.D. thesis significantly expanded his previous model [20] and added several features. By adding a repetition lever to the original four bodies, he completed his model. To account for the compliance of some of the contacts and bodies, springs, damping, and friction were included in certain locations. He could obtain a strong similarity between the simulation results and experimental data for his model. However, similar to his previous model, the values of his model parameters were not determined by actual mechanical tests and to make the simulation results similar to the experimental data, the values of his model parameters were tuned by trial-and-error.

In 1995, Van den Berghe, De Moor, and Minten [21] created a model that used *macros* for each of the five bodies of the action and bond graphs to simulate the system. In this method, springs and/or dampers are placed between each massive body, and the Newton-Euler equations are applied for each center of mass, resulting in a model with many degrees of freedom. The completed piano model consisted of 37 second-order differential equations and 27 constraint equations. The parameters of the model were based on physical properties. His model was not computationally efficient and this was the main limitation of his model. He reports four hours simulation time on a 486DX33 PC for 1 second of real time. In a later attempt to improve the computational efficiency of the model, a simplified model was created, and *trained* to match the experimental results. However, that model could not predict the response of the piano action for the different ranges of the pianist's blows.

In 1999, Hayashi et al. [22] used a one-dimensional model for the piano action to help develop an automatic playing piano. Their model was very similar to the model proposed by Matveev and Rimsky-Korsakov [16], however, their proposed model included a third mass resting on top of the other masses, which represented the hammer. There were some constrains in their model that limited the motion of the masses to represent the maximum travel of the bodies. Their model could only predict the motion of the hammer prior to string contact and for this range of motion, there was a good agreement between their model and the experimental results. However, the subsequent motion of the action was not modelled in their work.

Lastly, in 2006, Hirschkorn et al. [1] developed a high-fidelity model of the action. This

model is mechanistic, i.e., the parameters of this model were directly measured from the mechanical properties of the action. The main five parts of the action mechanism were explicitly available in this model. They used a modified Hunt and Crossley [8] contact model and a simple friction model that took care of both static and kinetic friction forces. Their model predicted the dynamic response of the action for hard blows very well, and also gave reasonable results for soft blows. However, their model could not predict the vibrations of the hammer shank and the key lift-off from the ground, which have been confirmed through observations with a high-speed video camera, for *forte* blows. This is because in their model, the hammer shank was modelled with a rigid body (not a flexible beam). Also, the connection between the key and the ground was modelled with a revolute joint and this joint does not allow the key to lift off from the ground. The key lift-off happens when the front of the key reaches the ground in *forte* blows.

Based on this literature review, it was concluded that addressing the limitations of Hirschkorn's piano action model will lead to developing the most high-fidelity model of a typical grand piano action.

1.3.2 Flexible Beam Mechanics

Finite Element Method vs. Analytical Beam Models and Discretization Methods

The deformation of a flexible body in a multibody system is studied either on a segment-by-segment basis or over the entire range of the body. In general, the former approach gives rise to the Finite Element Analysis (FEA) approach, whereas the latter is about analyzing flexible beams by using analytical beam models[3].

The FEA approach can be implemented to analyze a flexible body with any shape; however, the analytical beam models can be only used for analyzing flexible beams. The variables in the FEA are actual displacements and rotations of the nodes, whereas the variables employed in the analytical beam models are generalized elastic coordinates. To refine the results in the FEA, smaller elements are used, and in the analytical beam models

[3]These models include Euler-Bernoulli, Rayleigh, and Timoshenko, and will be explained in the next section.

more shape functions are added to achieve the same refinement [5].

Although the FEA method directly results in Ordinary Differential Equations (ODEs) for a flexible body, the analytical beam models produce Partial Differential Equations (PDEs). With the Rayleigh-Ritz discretization method, these PDEs are converted to ODEs, which then can be solved by using an appropriate ODE solver.

Taylor polynomials are usually used in Rayleigh-Ritz discretization; however, the use of orthogonal polynomials, such as the Legendre or Chebyshev polynomials, further improve the behaviour of the generated dynamic equations, in terms of the numerical computation.

Analytical Beam Models

There are various models of the flexible beam in the literature. The Euler-Bernoulli model for a flexible beam, which is a simplification of the linear isotropic theory of elasticity, is the simplest one. By definition, when an Euler-Bernoulli beam undergoes deformation, the beam cross-sections remain planar and perpendicular to the reference (centroidal) axis. From this, the following assumptions about this beam model can be inferred [4]:

1. The beam's elastic configuration is completely determined by four variables, corresponding to the axial deformation, two lateral deflections, and a torsional angle.

2. The shear due to bending, and warping due to torsion are neglected.

3. The beam exhibits very little strain, but possibly large deflections.

If the rotational inertia of the cross-sections of the beam is also considered in the beam model, then the model is called a Rayleigh beam. The Rayleigh model of a flexible beam yields more accurate results than those of the Euler-Bernoulli model. The Timoshenko model of a flexible beam is even more accurate than the Rayleigh model, since it also incorporates the shear effects [13]. Once a model for the flexible beam is chosen, the Rayleigh-Ritz approach can be adopted to discretize the Partial Differential Equations (PDEs) of the beam.

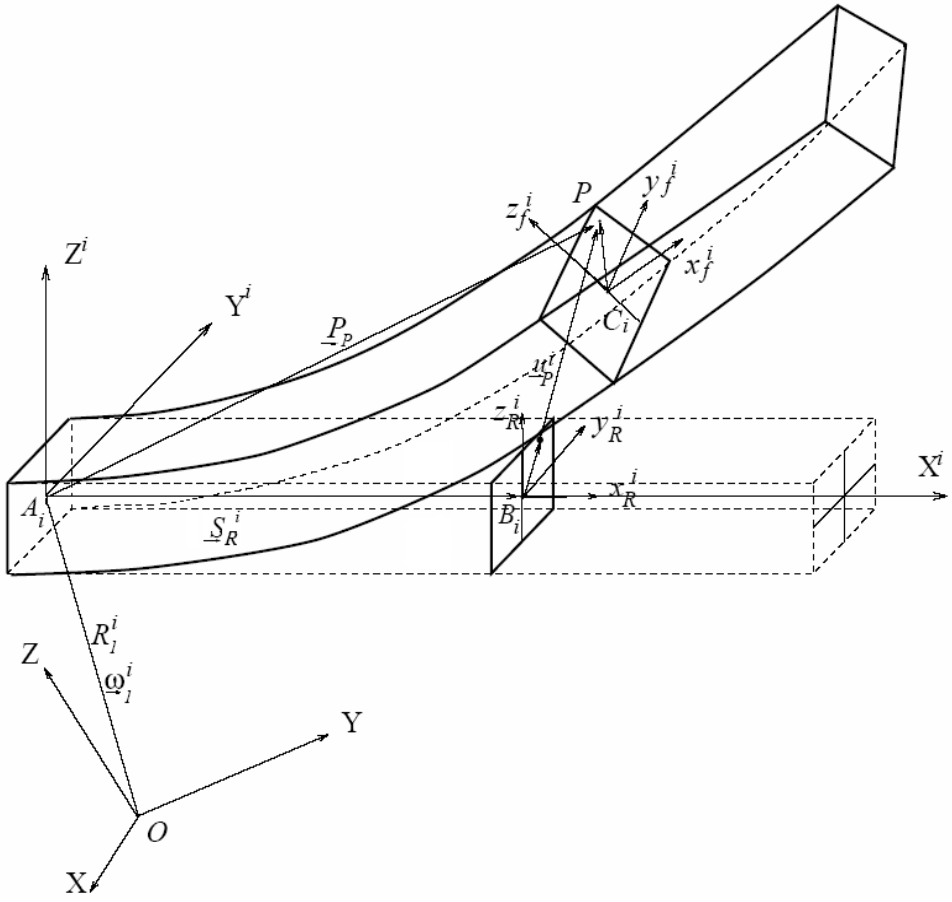

Figure 1.6: Flexible Beam and its Associated Reference Frames [4]

Shape Functions and Elastic Coordinates

Figure 1.6 illustrates a flexible beam, its body-fixed reference frame, and other associated reference frames. Frame $OXYZ$ is the inertial reference frame.

The reference frame $A_i X^i Y^i Z^i$ is the beam-fixed frame with its origin located at the centroid of the cross-section and its transverse axes aligned with the area principal axes at that point. The X^i axis is directed along the undeformed straight centroidal axis, and remains tangent to the centroidal line at A_i as the beam deforms. Frame $B_i x_R y_R z_R$ is the reference frame, defined for the cross-section that is distance S_R^i from the origin of

body reference frame $A_iX^iY^iZ^i$. This cross-sectional frame is a result of the translation of the body reference frame, along the undeformed centroidal axis. Due to the assumption that plane sections remain plane, this frame, albeit a body-fixed one, moves along the cross-section without deformation to $C_ix_f^iy_f^iz_f^i$, as the beam undergoes deformation, thus defining the position and orientation of the section at any instant of time [5].

The deformation of any generic particle on the centroidal axis of the beam located at the distance S_R^i from the origin of body reference frame $A_iX^iY^iZ^i$, can be specified by four deformation variables associated with the centroidal axis as beam deforms. The four chosen variables are $u(x,t)$ the pure axial deformation of the centroidal axis, $v(x,t)$ and $w(x,t)$, the transverse deformations in the direction of the Y^i and Z^i axes, respectively, and $\phi(x,t)$ the angle of twist of the beam section on which the particle resides with respect to the deformed centroidal axis.

Since the dynamic equations of the flexible beam, in terms of u, v, w, and ϕ, are long, they are not shown here. However, to discretize the dynamic equations to convert them from Partial Differential Equations (PDEs) to Ordinary Differential Equations (ODEs), Taylor polynomials can be used in the following Rayleigh-Ritz approach:

$$u(x,t) = \sum_{n=1}^{n_u} u_n(t)x^n \tag{1.1}$$

$$v(x,t) = \sum_{n=1}^{n_v} v_n(t)x^{n+1} \tag{1.2}$$

$$w(x,t) = \sum_{n=1}^{n_w} w_n(t)x^{n+1} \tag{1.3}$$

$$\phi(x,t) = \sum_{n=1}^{n_\phi} \phi_n(t)x^n \tag{1.4}$$

where x corresponds to the distance S_R^i shown in Figure 1.6 and $u_n(t)$, $v_n(t)$, $w_n(t)$, and $\phi_n(t)$ are called elastic coordinates. n_u, n_v, n_w, and n_ϕ are the number of elastic coordinates used for the four deformation variables. The greater the number of the elastic coordinates used in the formulation, the greater the number of vibration modes of the flexible beam can be captured.

In Figure 1.6, it is clear that there is no rigid body motion of the beam with respect

to the body-fixed frame. As it was mentioned earlier in this section as the beam moves, the three coordinate axes of the body frame are kept coincident with the three principal axes at the end of the beam. In other words, the following boundary conditions are always satisfied

$$u(0,t) = 0 \tag{1.5}$$

$$v(0,t) = 0, \;\; v'(0,t) = 0 \tag{1.6}$$

$$w(0,t) = 0, \;\; w'(0,t) = 0 \tag{1.7}$$

$$\phi(0,t) = 0 \tag{1.8}$$

where the *prime* represents the derivative with respect to x. In addition, Chebyshev and Legendre polynomials can be implemented as the shape function, and the details regarding their implementation are in [5].

The DynaFlexPro software[4] is used to generate the dynamic equations of the piano action mechanism in this work. The latest version of this software supports Rayleigh flexible beam model, and any of Taylor, Chebyshev, or Legendre polynomials can be used as shape function. The FEA approach is not incorporated in this software, yet. Since the piano action model is created in this software, the Rayleigh flexible beam model will be used to model the hammer shank.

1.3.3 Biomechanical Model of the Fingertip

Adding a biomechanical model of the pianist's hand, elbow, and arm to the piano action model can disclose interesting issues about the pianists' gesture, when they play the piano, that may eventually help the piano tutors to better teach piano lessons. However, before adding the model of the pianist's hand, arm, and elbow to the action model, one needs to precisely characterize the contact between the pianist's fingertip and the top of the key front. Once this contact location is characterized, then the input to the piano action model can be changed from the pianist's fingertip force to the displacement of the last bone of the fingertip. Therefore, a model for representing the stiffness and damping characteristics

[4]The DynaFlexPro software is explained in Section 3.1.

of the fingertip pulp is needed[5].

The mechanical properties of the fingertip pulp, in terms of its stiffness and damping, have been already investigated for a few different purposes. Serina et al. [23, 24] have investigated the role of the fingertip pulp in attenuating the dynamic forces transmitted to the wrist during activities such as typing. The purpose of their research was to examine the hypothesis that repeated loading of the fingertip contributes to tendon and nerve disorders of the wrist. Consequently, they adopted a structural model for the fingertip pulp, based on the theory of elastic membranes [24]. According to their model, in any indentation situation, the pressure on the fingertip is constant across the contact area [24]. With almost the same purpose, but different approaches, Pawluk [26, 27, 28] and Wu [29, 30] tried to find the mechanical response of the fingertip pulp to the dynamic loading. Wu used a two-dimensional non-linear FEA method to model the fingertip pulp; however, due to the high computational cost of the FEA methods, his work was disregarded. Pawluk has investigated the dynamic response of the fingertip pulp, based on the Fung's quasi-linear viscoelastic model of the tissue. Her model captured the principal features of the distributed pressure response of the fingertip [31].

Fingertip pulp has been also studied to examine the relationship between the stimulation of the mechanoreceptors (that are concentrated in the curved region of the fingertips), and the force applied to the fingertip [23, 24, 25]. Further research in this area might provide a further understanding about the force feedback which the pianists experiences from their fingertips while they plays the piano. This can help piano tutors to better realize the learning process of playing the piano.

As it was mentioned in Section 1.3.2, the DynaFlexPro software does not support the FEA approach yet, and therefore in the scope of this thesis, the final fingertip pulp model was needed to be a lumped model with mechanistic components. This also results in fast simulation times of the whole model (action model and the fingertip).

After all the fingertip pulp models in the literature were examined, it was only Pawluk's model that, according to the two criteria of the thesis, seemed to be an appropriate choice. However, based on the information she has provided in her papers [27, 28], her theoretical

[5]A good fingertip model is also necessary in the case the motor torque control should be replaced by the motor shaft position control. More details are provided in Section D.4.

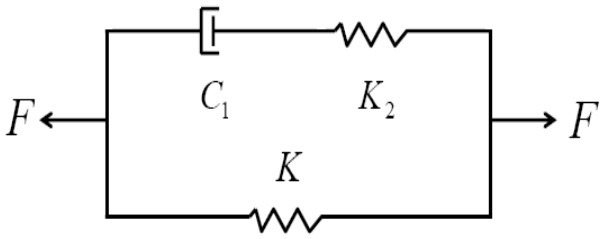

Figure 1.7: Proposed Non-Linear Model for the Fingertip Pulp

results could not be reproduced. Also, the parameters of her model were so sensitive to small changes that, her model was not used in this thesis.

Finally, after thoroughly examining all the models, a non-linear model for the fingertip pulp, shown in Figure 1.7, was proposed. This model has non-linear spring-damper components and closely reproduces Pawluk's experimental data. The details of this model are given in Section 3.8.

1.4 Contributions of the Thesis

The performance of a piano, to a great extent, is related to the design of its piano action. For piano makers, a high-fidelity design tool for designing piano action, based on the mechanical properties of the piano action components, is crucial. The main purpose of this thesis is to improve the fidelity of the state-of-the-art dynamic model of a piano action mechanism developed by Hirschkorn et al. [1] at the University of Waterloo. The flexibility of the hammer shank and the connection of the piano key to the ground were identified as the main areas for improvement. As it will be discussed in the following chapters, by re-modelling the hammer shank with a flexible beam, the fidelity of the piano action model is not improved but this discloses the facts that the flexibility of the hammer shank causes a scuffing motion for the hammer head and also changes its impact velocity. By re-modelling the revolute joint of the key with a revolute-prismatic joint however, the fidelity of the model significantly increases.

Adding biomechanical aspects to the piano modelling may eventually help the piano tutors to better teach piano lessons. To that end, in this thesis, the first step for adding

the biomechanical aspect to the available piano model, i.e. proposing a mechanistic model that represents the stiffness and damping characteristics of the fingertip pulp, is taken. By using experimental data, the values of the parameters of this model were obtained. This allows changing the input of the piano model from the pianist finger force to the displacement of the last bone of the fingertip.

Lastly, to tackle the problem associated with the previous torque control method of the motor[6] used in the experimental setup for validating the analytical results, a new method, on a real-time PC is developed. This new method results in a better performance for the torque control of the motor.

In summary, the main contributions of the thesis are as follow:

- Improving the fidelity of the dynamic model of a grand piano action developed by Hirschkorn et al. [1] by adding a flexible beam model for the hammer shank and modifying the connection point between the key and the ground.
- Adding biomechanical aspects to the piano model by replacing the pianist's finger force, as the piano action model input, by the displacement of the pianist's last finger bone.
- Implementing a new method for controlling the torque output of the motor.

[6]Explained in Section 2.5.

Chapter 2

Experimentation

The same action mechanism from the Boston GP-178 grand piano that was used by Hirschkorn [2] is also adopted for the experimental setup for this thesis.

This action mechanism in Figure 2.1 is[1], in fact, the keyboard of the GP-178 grand piano, stripped to a single key. In terms of space, this configuration provides access to the different locations of the action mechanism to install the encoders at specific locations.

The dynamics of a vibrating string is quite complex, and including it in the piano model is beyond the scope of this thesis. Modelling the contact between the hammer head and the rigid bar is not difficult and is similar to the modelling the other contacts that exist in the piano action[2]. Therefore, similar to Hirschkorn's work [2], a rigid bar is used in the experimental setup, instead of a real string.

In order to run the experiments with this mechanism, the following measurement instruments and motor are required:

- A load cell for measuring the force transferred from the motor arm to the key,
- Three encoders for measuring the rotation of the different parts of the action,
- A high-speed video camera for measuring the lift-off from the key,
- A strain gauge for measuring the flexibility of the hammer shank, and

[1]Figure 1.1 shows the same action mechanism in another view.

[2]Figure 3.5 shows the 14 contact locations in the piano action mechanism.

- A motor for actuating the key.

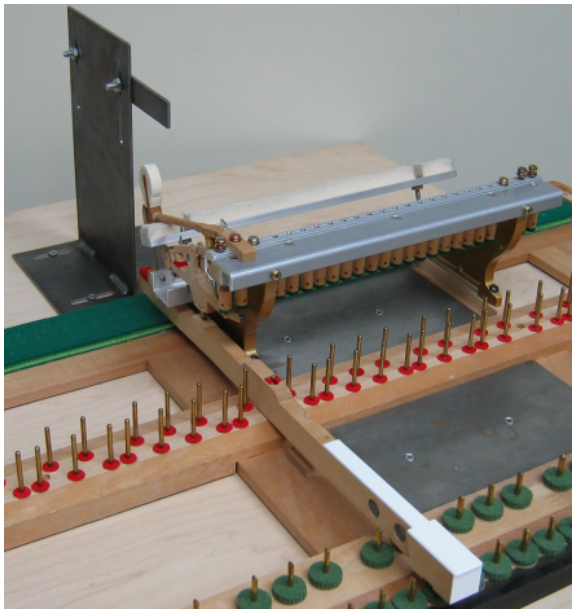

Figure 2.1: Modified Keyboard with the Key 52

Aside from the strain gauge and the real-time target PC, all the hardware is available from the previous work [2]. A short description of the equipment is provided in the following sections.

2.1 Actuation of the Key

For two reasons, providing an actuating element for the experimental setup is necessary. First, the consistency of the experimental setup, for a specific input force profile should be tested. Secondly, the pianist is not able to play the piano with any given force profile, and a precise electromechanical device is needed for this purpose. Therefore, a Kollmorgen MT308A1 DC brushless rotary motor was chosen [2]. To create a linear motion with this motor, a small resizable aluminium arm was attached to the output shaft [2]. The motor,

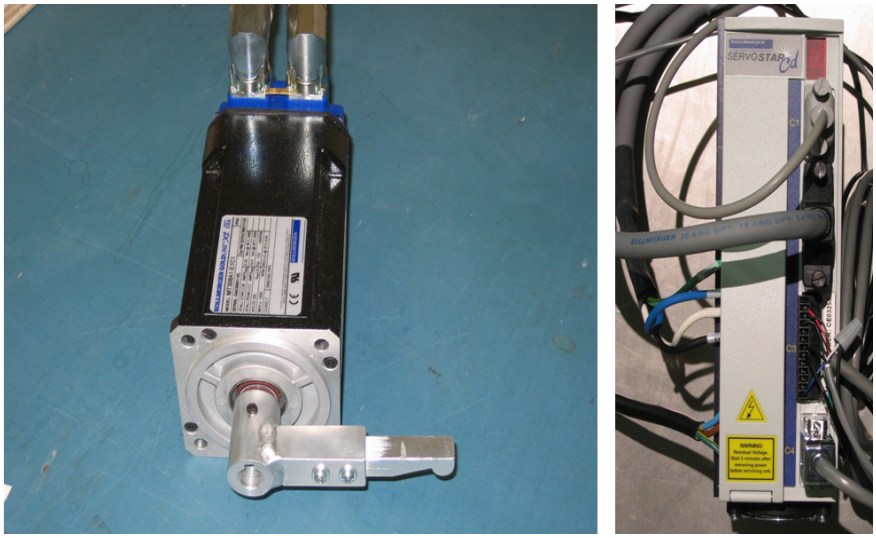

Figure 2.2: (a) Motor and Actuation Arm (b) Motor Drive

its arm, and the CE03250 amplifier used for running that are presented in Figure 2.2[3].

According to the distance over which the motor is required to provide a linear motion (10 mm)[4], the length of the motor arm was chosen as 100 mm [2]. With this arm length, the motor is capable of generating peak forces as high as 120 N. Since, in the literature, actual pianists' finger forces have been tested [2], and found not to exceed 50 N, the 120 N force from the motor suffices for this application. Although in the previous work [2] a National Instruments PCI-7342 Motion card was used for controlling the motor torque output, in this thesis, the motor is controlled by a National Instruments PCI-6229 DAQ card on a real-time target PC. More detail about this is provided in Section 2.5.

2.2 Force Measurement

To compensate for the imperfections that exist in the torque control of the motor, a torque (or force) sensor should be adopted for measuring the actual torque output of the motor

[3]Actual tests confirm that this motor and the CE03250 amplifier are capable of producing a desired force profile with a very high precision.

[4]Since θ=10/100 and $\sin(\theta) \approx \theta$, this distance is appropriate.

in each experiment. The torque of the motor is eventually transferred to the front of the key by the motor arm. Instead of measuring the motor torque by a torque sensor, it is more direct to measure the force on the top of the key front. Therefore, a 25 lb (111 N) rated subminiature load cell was used for directly measuring the force transferred from the motor arm to the piano key [2].

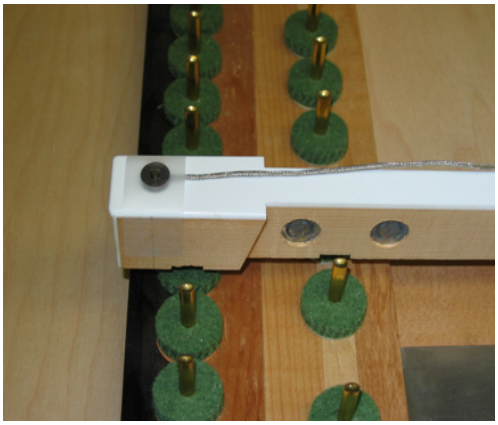

Figure 2.3: Load Cell Mounted on the Key

This load cell model is strain gauge based, and the National Instruments SCXI-1520 signal conditioning module was used for reading that. By using the PCI-6034E multifunction DAQ card, it was possible to read the load cell with a 2 kHz sampling rate [2]. It was the highest sampling rate that could be used without missing data in any time step.

Since the load cell was very light (1.1 g), its mass was not considered in the action model. Figure 2.3 depicts the load cell mounted on the top of the front of the key, by using an adhesive strip.

2.3 Position Measurement

For measuring the rotation of the different parts of the action mechanism, a modular encoder system, from the MicroE Systems Company, was used [2]. This system consists of optical encoders and scales which are not physically connected. As opposed to the other common encoder types, this type of encoder introduces no friction and adds very little

inertia to the system.

The scales are mounted on different parts of the mechanism. When these parts rotate, the scales rotate, as well. An optical sensor measures the amount of rotation by counting the number of small bars printed over the scales. The scales (linear and circular) and optical sensor are represented in Figure 2.4 (a). Figure 2.4 (b) signifies a circular scale mounted on the piano hammer which is read by an optical sensor.

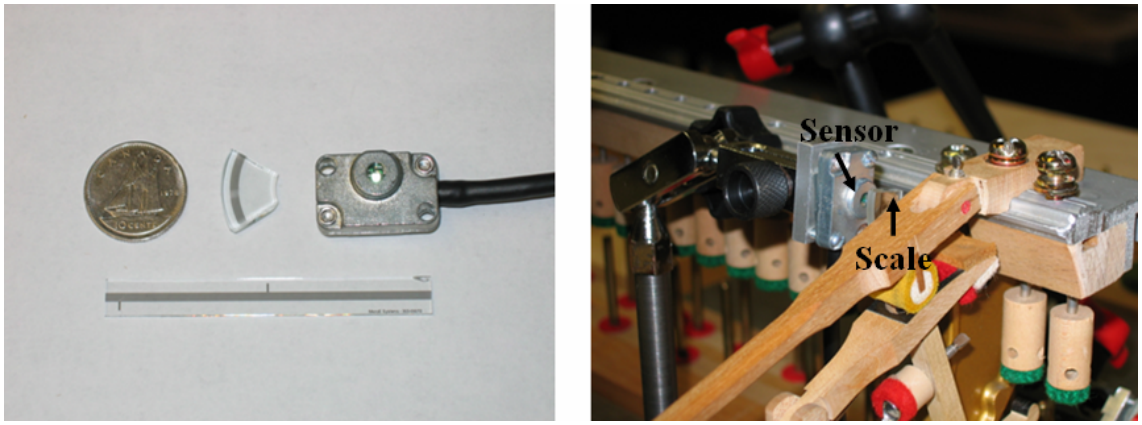

Figure 2.4: (a) Optical Encoder and Scales (b) Encoder and Scale Mounted on the Hammer

A small processor is attached to each optical encoder and it interpolates the readings and provides a quadrature encoder signal, meaning that the resolution is 4 times better than the actual graduations on the scales. In this work, two circular scales with 1.25 in and 2.25 in diameters, and one linear scale with 50 mm length were used. The resolution of the circular scales is 163,840 and 327,680 counts/revolution, respectively, and the resolution of the linear scale is 0.5 μm/count.

The quadrature signal is measured by the National Instruments PCI-6602 Counter/Timer board. By taking advantage of the high-speed capture and buffer capabilities of this Counter/Timer board, it is possible to read the optical sensors with a 2 kHz sampling rate.

The experimental setup with the motor, load cell, and attached encoders is illustrated in Figure 2.5.

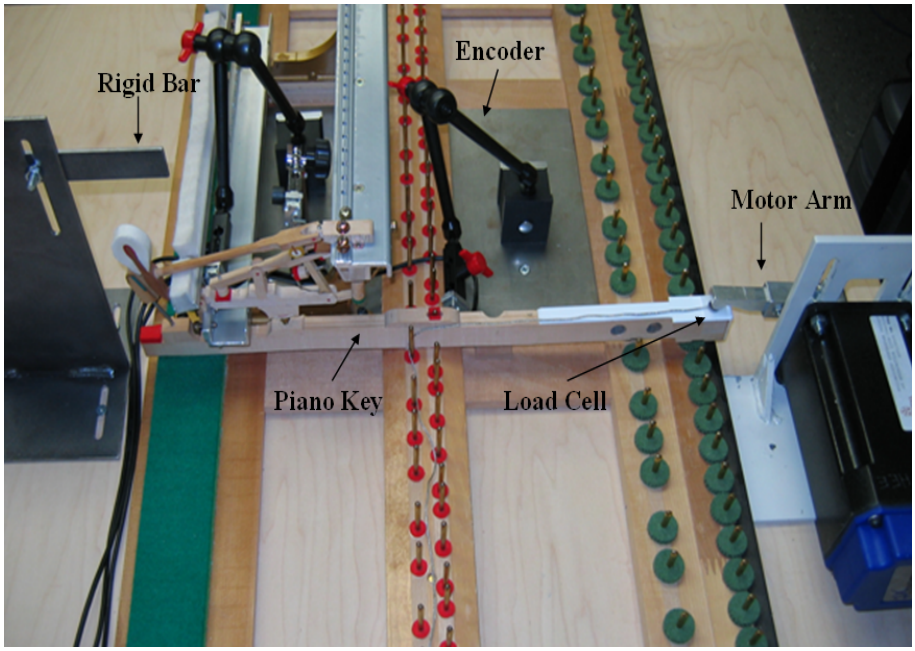

Figure 2.5: Experimental Setup

2.4 High-Speed Video Imaging

A high-speed video camera is necessary in order to attain some specific types of accurate measurements. For measuring the lift-off from the key, for instance, a high-speed video camera provides accurate measurements.

A Photron Fastcam-X 1280 was used for the video recording [2]. The software, included with the camera, allows tracking the planar coordinates at any desired point in the videos.

The camera is capable of capturing high speed videos at resolutions up to 1280 by 1024 pixels and speeds up to 16,000 frames per second, although the higher frame rates are possible with lower resolutions only. The resolution of 1280 by 1024 pixels and the speed of 2,000 frames per second were used for video recording in this work.

2.5 Real-Time Target PC

Hirschkorn used two different open-loop methods for controlling the motor torque output [32]:

1. By directly writing the motor torque demand signal at the analog port of the amplifier (motor drive), and

2. By using the National Instruments PCI-7342 motion card.

Due to the limited computational speed of the CPU of the available PCs, the first method could not be run faster than 100 Hz (10 ms refresh rate)[5]. This refresh rate was not fast enough for sending the torque demand signal to the motor, for some typical pianist finger force profiles. Figure 2.6 shows an example in which a pianist finger force profile cannot be accurately reproduced with a 10 ms refresh rate.

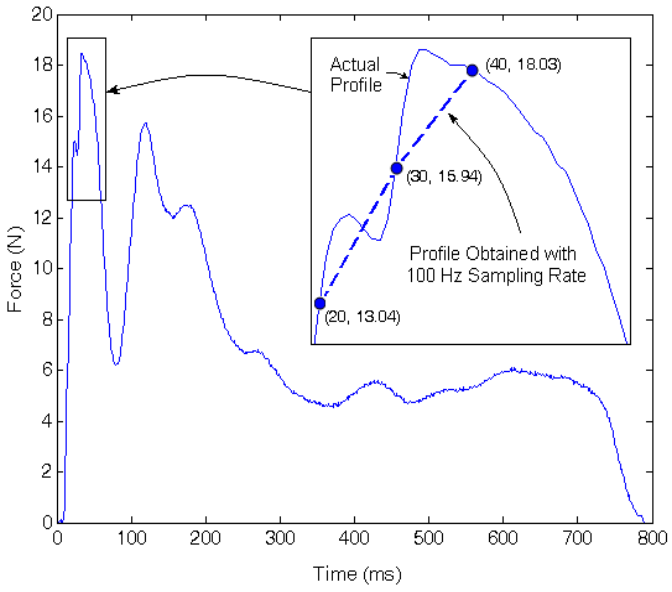

Figure 2.6: A Typical Finger Force Profile of a Pianist with 100 Hz Sampling Rate

[5]In this case, a PC with a 2.4 MHz CPU was used.

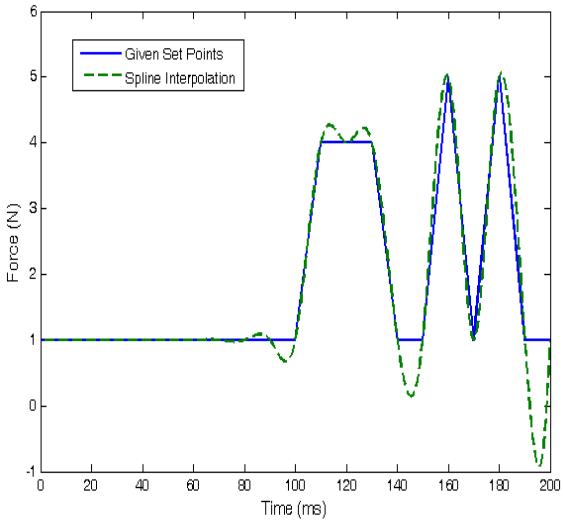

Figure 2.7: Spline Interpolation of the Specified Motor Output Profile

The second method can potentially be run with 8330 Hz (120 μ s) frequency; however, the software that National Instruments has included with the PCI-7342 motion card, allows set points only 10 ms away from each other. The points between 10 ms are automatically interpolated by using splines. As seen in Figure 2.7, this introduces a problem.

The solid line represents the specified motor output profile, and the broken line is the interpolated motor output profile that is sent to the motor drive. At times this low (10 ms between points), there is significant overshoot due to the cubic spline interpolation, and this is an artifact of the spline function.

By checking the performance of these two methods, it is concluded that a solution for improving the performance of the motor torque control is to increase the execution time (refresh rate) in the first method. One way is the employment of a real-time execution platform which can be a *PCI eXtensions for Instrumentation* (PXI) or a real-time PC. For this project, it is decided to provide a PC with a real-time operating system. A PC with a Pentium 4 CPU was purchased, and a real-time operating system from National Instruments was installed on it. The torque control programs are then run on this real-time PC which allows the deterministic and fast execution of programs. Since this real-time platform provides a faster execution time than a regular PC, it can be simultaneously used

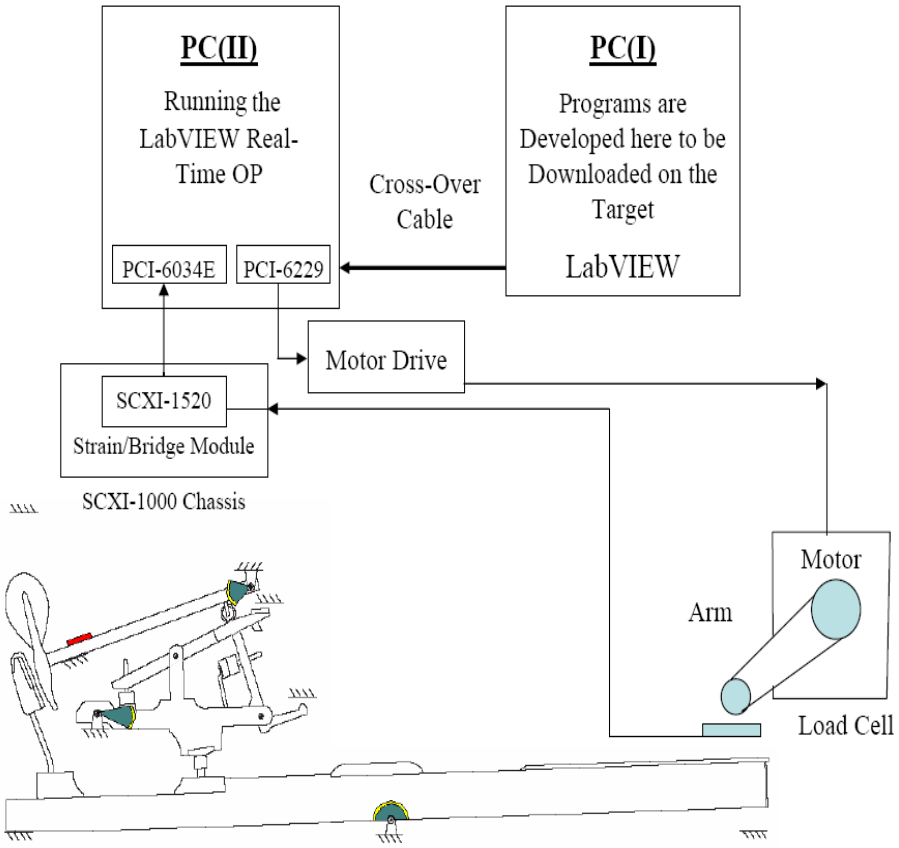

Figure 2.8: Idea of Using a PC as a Real-Time Platform

for reading the load cell, while the motor demand signal is sent to the amplifier from there. It turns out that the fastest frequency at which the real-time PC is able to read the load cell and send the torque demand signal to the amplifier simultaneously is 500 Hz (five times faster than in [2]).

Figure 2.8 shows how the real-time PC target (PC(II)) is implemented for real-time applications. The torque control programs are developed at the host machine (PC(I)). Then, programs are transferred to the real-time target machine by a cross-over cable, where they can be executed fast and deterministically.

2.6 Strain Measurement

A strain gauge is needed for measuring the strain on the hammer shank. The hammer shank is an octagonal wooden rod, and the width of each of its edges is 2.57 mm. According to this geometry, only a very narrow strain gauge can be mounted on one of the shank's edges. For this application, the strain gauge type EA-06-062DN-350 from Intertechnology Inc. is purchased. The nominal resistance of this strain gauge is 350 ohm and the width and length of this strain gauge are 1.95 mm and 5.51 mm, respectively, as shown in Figure 2.9.

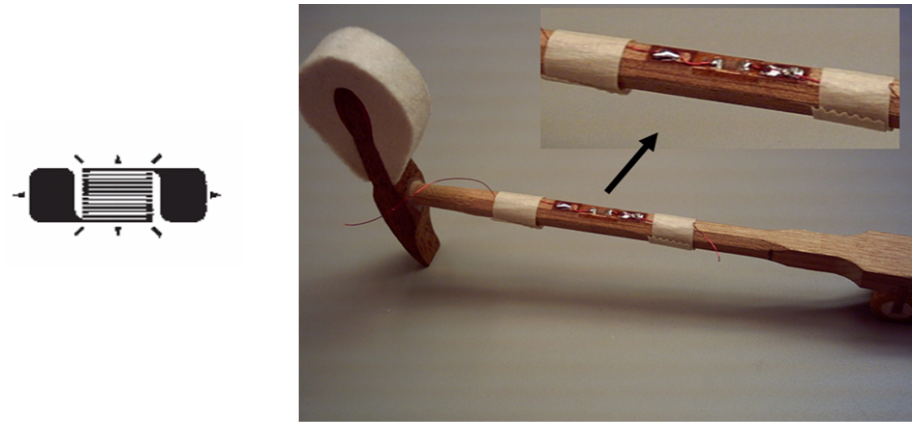

(a) (b)

Figure 2.9: (a) Strain Gauge (b) Strain Gauge Mounted on the Hammer Shank

As shown in Figure 2.10, this strain gauge was incorporated in a *Wheatstone bridge*. Three passive 350-ohm resistors were added to the bridge, to complete its electric circuit. The same devices that were used for reading the load cell, i.e., National Instruments SCXI-1520 signal conditioning module and PCI-6034E multifunction DAQ card, are used for reading this strain gauge.

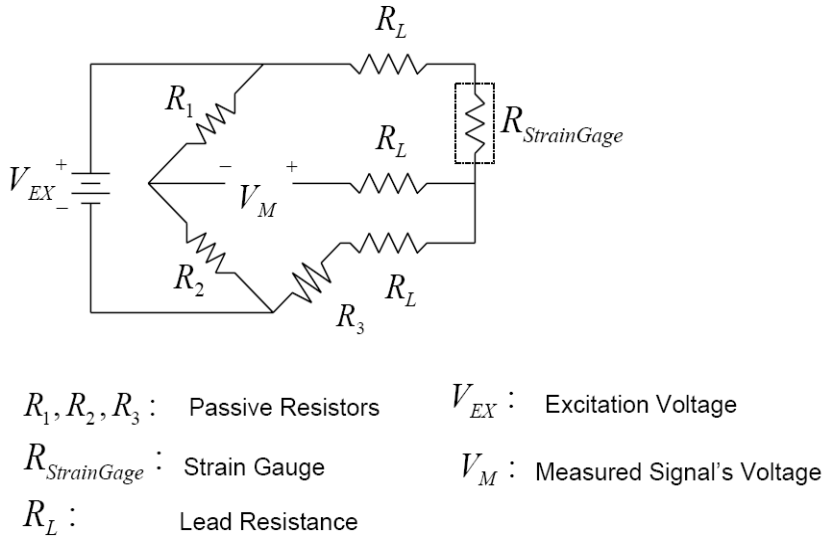

Figure 2.10: Strain Gauge Electric Circuit

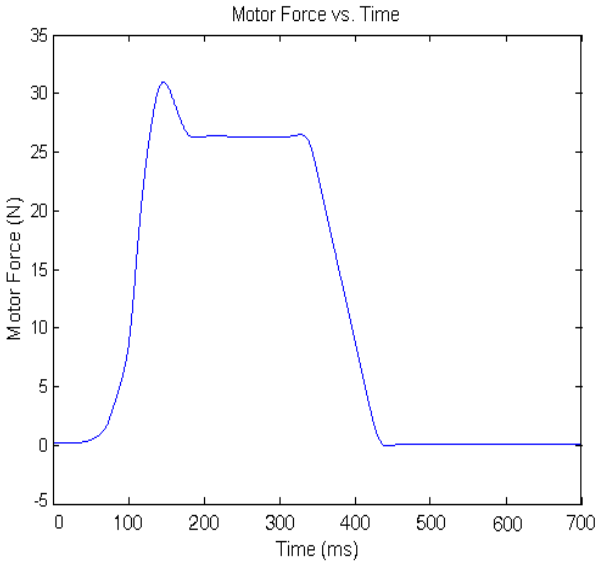

Figure 2.11: Typical Motor Force Profile

2.7 Strain Results

A reasonably hard blow from a pianist is called *forte*. The effect of the flexibility of the hammer shank on the dynamic response of the piano action is appropriately large for this

blow. Consequently, for the typical *forte* profile in Figure 2.11, the strain on the hammer shank was experimentally measured. The maximum of the motor force profile is 30 N.

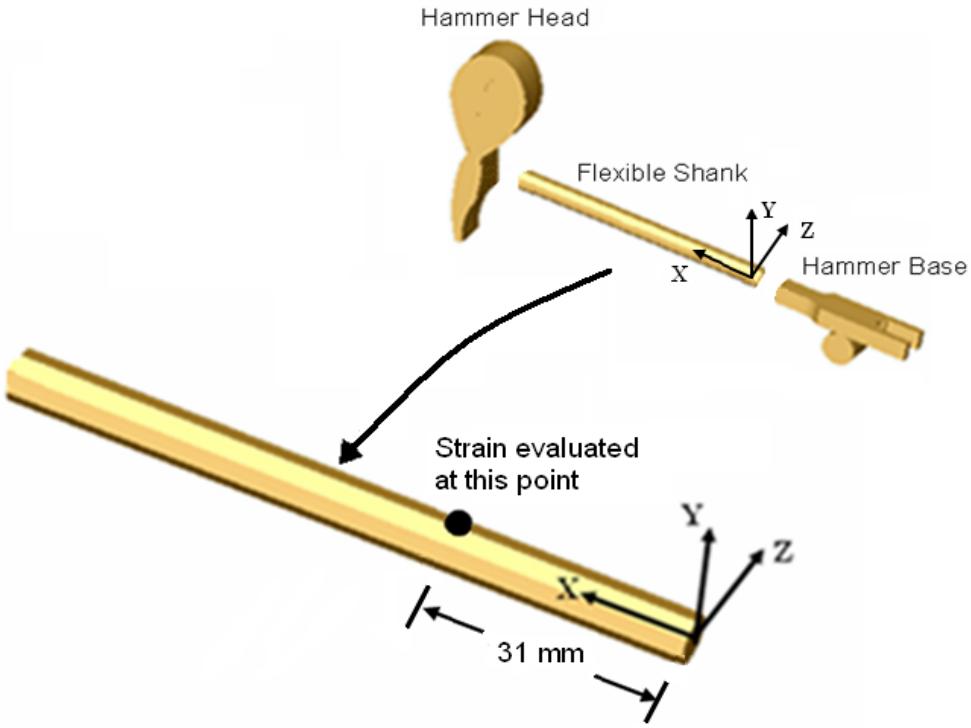

Figure 2.12: Hammer and its Flexible Shank

Figure 2.12 illustrates the hammer shank and the point at which the strain has been measured. It should be noted that the strain is measured at the top of the hammer shank, where the strain gauge is mounted.

The measured strain at the specified point of the hammer shank is depicted in Figure 2.13, for three trials. Three trials are performed for the strain measurement to verify that the experimental setup is capable of producing consistent and repeatable results. As it is seen, the strain profiles for the three trials are virtually identical. This shows that the experimental setup can produce very consistent strain profiles with the same force input to the motor.

The positive strain shows that the top part of the hammer shank is in tension and the negative strain shows that point is in compression. A comparison between the theoretical

and experimental results for the strain is conducted in Chapter 5.

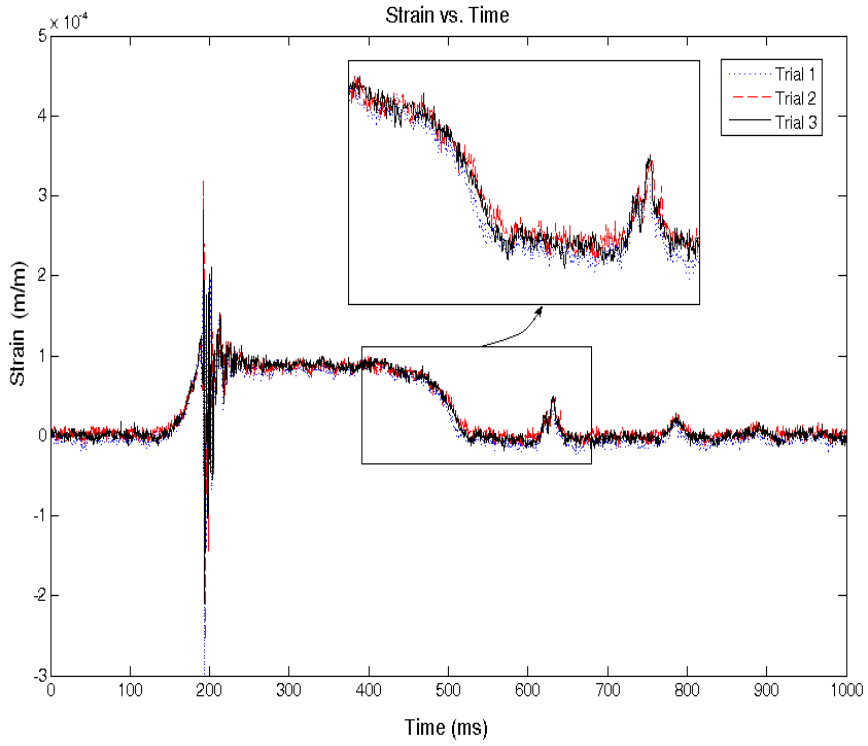

Figure 2.13: Measured Strain for Three Trials with a Forte Blow

2.8 Motor Torque Control

As it was mentioned in Section 2.5, to control the torque output of the motor, by using a real-time PC the motor torque demand signal is sent to the amplifier analog port. The maximum refresh rate at which the torque demand signals could be sent by this method, is 500 Hz[6]. In this method, since no feedback from the actual torque output of the motor is used to modify the motor torque demand signal, the control loop is open.

[6]This is the maximum refresh rate that the real-time operating system can provide. In faster refresh rates, some cycles may not have enough time to execute.

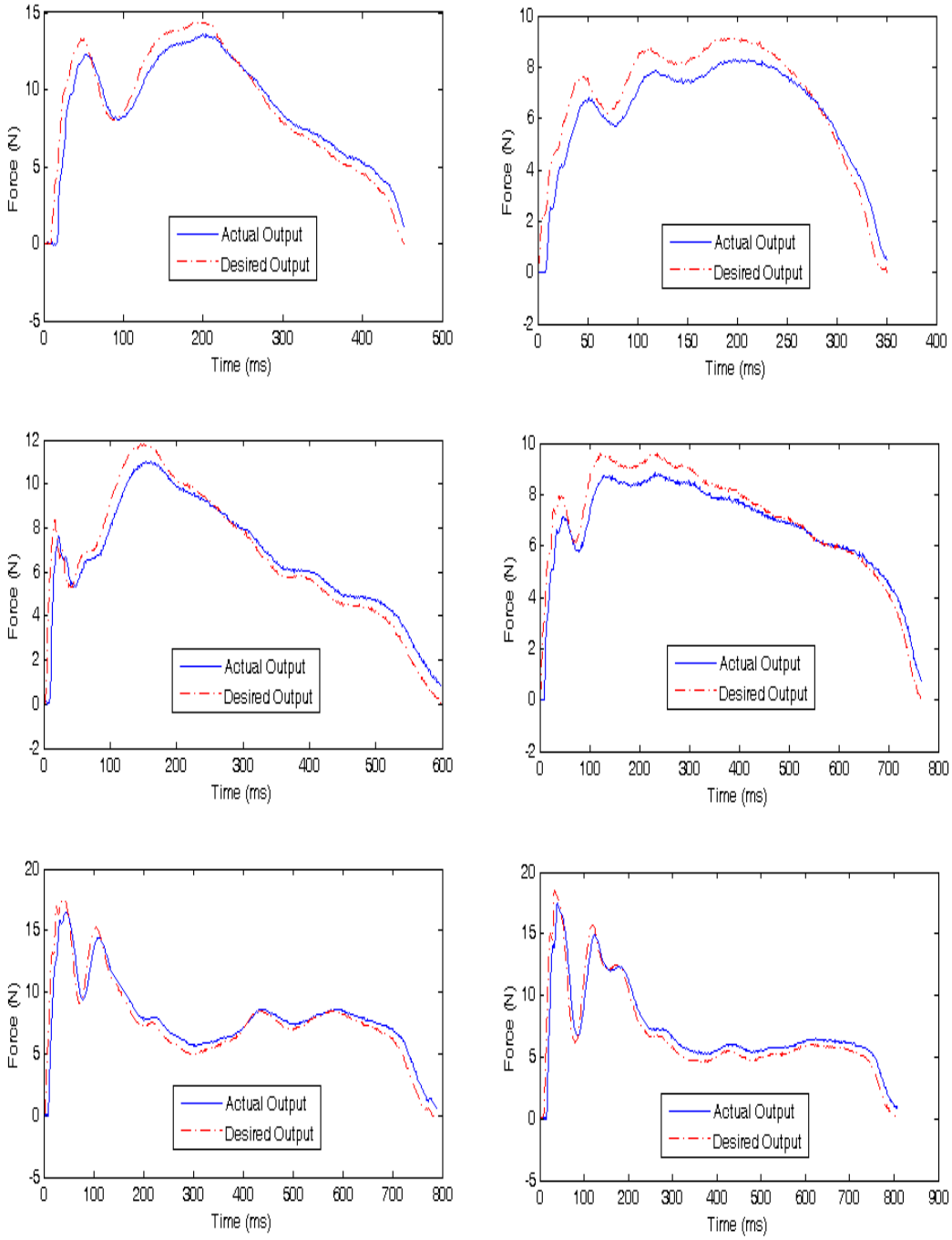

Figure 2.14: Desired and Actual Force Output Curves

The curves in Figure 2.14 show the performance of this method. These force profiles reflect the static force response of the motor, i.e., in the experiments run to obtain these force profiles, the motor arm pushes on a static surface. As it is seen, in the open-loop operation mode, the difference between the desired force profile that is loaded onto the amplifier, and the actual force output of the motor measured by the load cell is not significant[7].

However, there is a simple way by which the open-loop performance of the system can be slightly improved. By shifting the actual force output 8 ms back, a better match between the desired force output and the actual force output is obtained. At the maximum points of the force curve the match is not so good, but overall, the shifting back is a good solution to provide more accuracy, with maintaining the system working open-loop.

Figure 2.15 shows two typical force curves before and after 8 ms shifting back. This figure shows that by applying the shifting, the maximum difference between the desired and actual force curves goes down to 6.5 % (check the bottom plots in Figure 2.15). Based on this error, the performance of the open-loop operation is quite satisfactory.

To improve the performance of this new method even further, the neural network technique and a few linear control methods were tried; however, none of them increased the accuracy of the control on the motor torque output. These control methods are included in Appendix D.

By using the equipment described in this chapter, it turned out that the experimental setup is capable of producing consistent responses for a given pianist finger force profile. To validate the response of the piano action model developed in this thesis, a few experiments were conducted and the response of the action model was compared with the corresponding experimental data.

[7]For small rotation angles of the key, since the motor force and the motor arm are perpendicular to each other and the length of the motor arm is constant, as well, the equation $T = F.d$, where d is the motor arm, is valid. Therefore, in this case the words *torque control* and *force control* can be used, interchangeably.

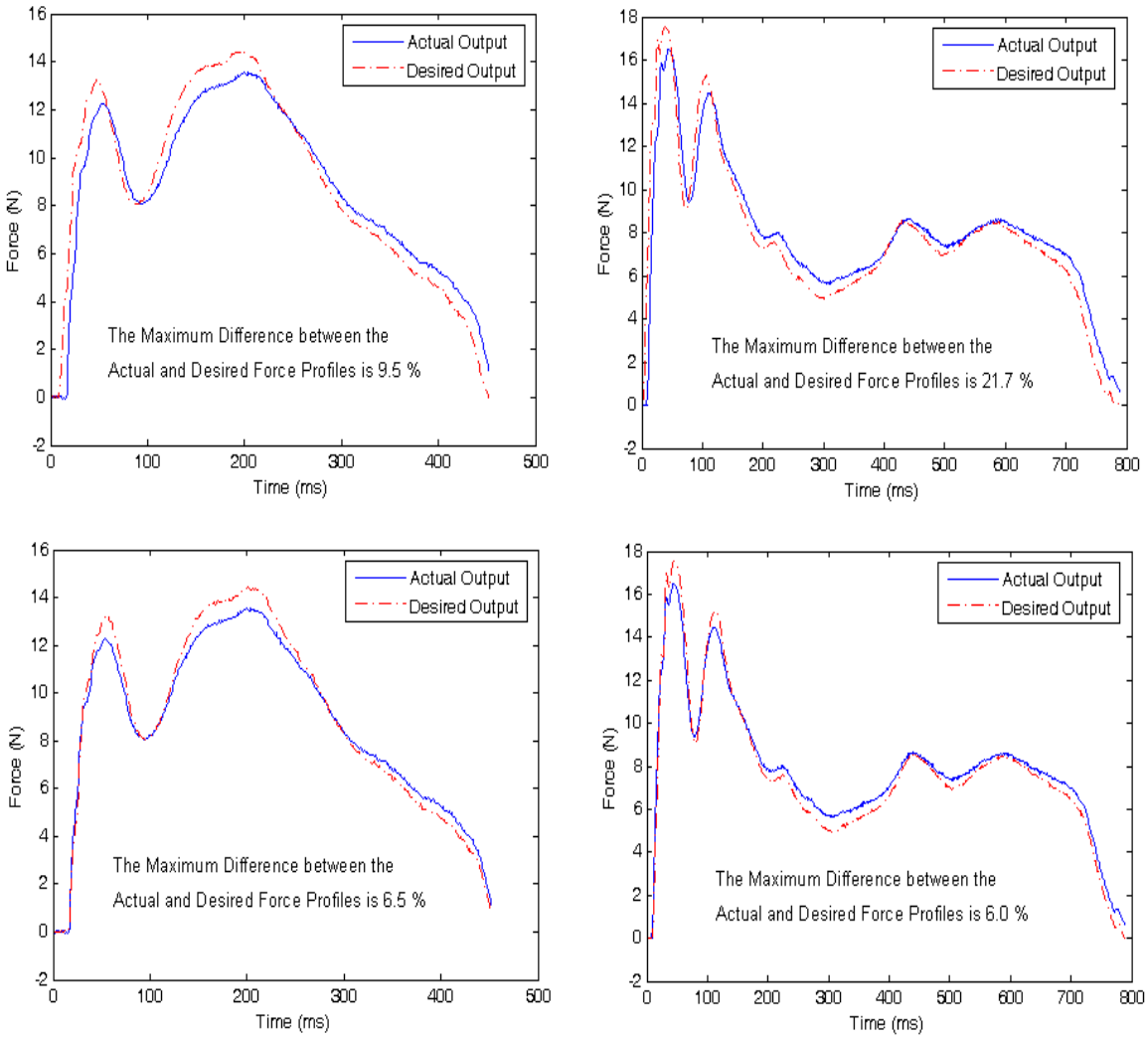

Figure 2.15: Two Typical Force Curves before (Top Profiles) and after (Bottom Profiles) 8 ms Shifting Back

Chapter 3

Dynamic Model of the Piano Action

The components, physical parameters, and geometric dimensions of the dynamic model of the piano action in this thesis are measured from key 52 of the Boston GP-178 grand piano. Although this is a specific piano action mechanism, this model can be modified to be used for other actions too.

Since all the components of the piano action move exclusively in a single plane, the model of the piano has been kept two-dimensional. Except for the model of the hammer shank and the connection of the piano key to the ground, the dynamic model created in this work is similar to that in [2].

The piano action mechanism used in this thesis is shown in Figure 1.1. Newton's second law can be used to precisely model certain dynamic aspects of this mechanism; however, for some dynamic phenomena such as friction and contact between surfaces made of felt (or leather), that exist in many locations of this mechanism, there is no accurate mechanistic model in the literature [33]. Although finding a high-fidelity model for the friction and contact for this specific mechanism is not the focus of this work, the model used for the contact and friction significantly affects the precision of the model results.

The felt bushing in Figure 3.1 is another element that is difficult to precisely model. The bushing creates friction in the joint and also allows some translational motion.

Figure 3.1: Felt Bushing on the Whippen

3.1 Action Mechanism

The DynaFlexPro software is used to generate the dynamic equations of the piano action mechanism. This software is a package for modelling and simulating the dynamics of mechanical multibody systems [10], developed at the University of Waterloo, and works based on Linear Graph Theory [36]. A graph is created by describing the interconnections (edges) between all of the physical locations (nodes) in a system. With a very methodical approach, a graph can be converted into a system of equations.

A partial graph of the system is presented in Figure 3.2[1]. The rigid bodies, which account for the masses, moments of inertia, and gravitational forces on the bodies, are represented by the dashed lines. Besides the key, whippen, jack, repetition lever, and hammer, a massless body has been also added to the mechanism. The key is attached to this massless body with a revolute joint, and this massless body is connected to the ground with a prismatic joint. Therefore, the massless body allows the key to lift off the balance rail without adding any inertia effects to the mechanism. In Section 5.2, the results of this model indicate that the massless body, along with the revolute and prismatic joints,

[1]The exact locations of the points on the different components are shown in Figure A.1 in Appendix A.

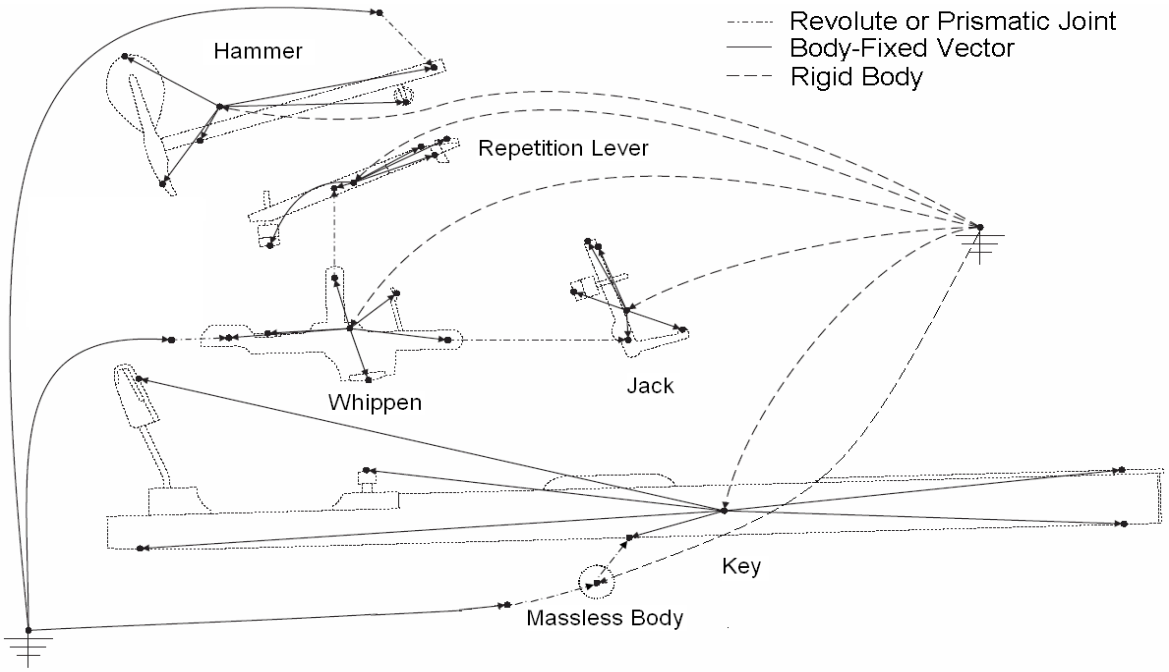

Figure 3.2: Simplified Graph of a Piano Action

improve the previous simple revolute joint model for the connection of the key to the ground [2].

The joints, which connect the bodies together, should also be included in the graph. Two revolute joints connect the whippen and hammer to the ground, and two revolute joints connect the jack and repetition lever to the whippen. The latter joints also include rotational springs. As it was mentioned earlier in this section, a revolute joint connects the key to the massless body, and a prismatic joint connects the massless body to the ground.

There are 14 edges for the contacts between the bodies, but it is too complicated to represent them in the graph, and they are, instead, discussed in Section 3.2. There is also one edge for representing the pianist finger force in the mechanism which is not shown in the graph.

The DynaFlexPro software takes the topology and parameters of a mechanical system, as the input, in the form of a text file, and then generates the dynamic equations of the system, symbolically.

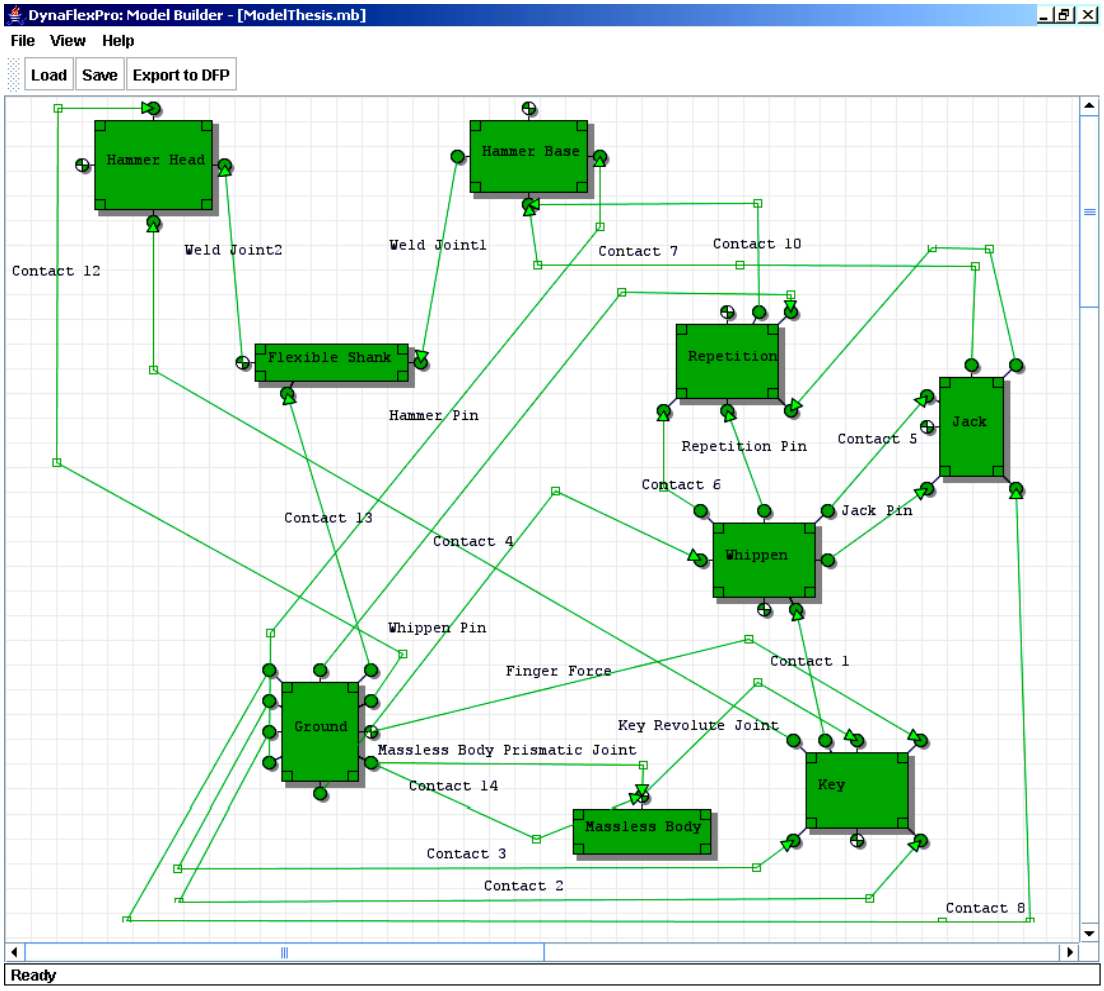

Figure 3.3: ModelBuilder Representation of the Piano Action Mechanism

ModelBuilder is a Graphical User Interface (GUI) that easily creates the input text file of a given mechanical system. Figure 3.3 illustrates the piano action mechanism in the ModelBuilder GUI. In this figure, the 9 boxes represent the 8 moving parts of the model and the ground. The lines between these boxes represent the joints, contact forces, or external forces that exist between the parts. The revolute joints connecting the jack and repetition to the whippen also include rotational springs. By clicking on each box or line, the properties of the corresponding part or constraint can be set or modified. The inputs

and modelling variables of the mechanical system are also set in ModelBuilder. Once the input text file is created, it is used by DynaFlexPro for creating the dynamic equations of the mechanical system.

The representative spanning tree for the graph of the piano has been selected so that the pianist finger force is the input to the mechanism and the nine system variables are: θ_k, θ_w, θ_h, θ_j, θ_r, Y_k, u_1, v_1, and v_2[2].

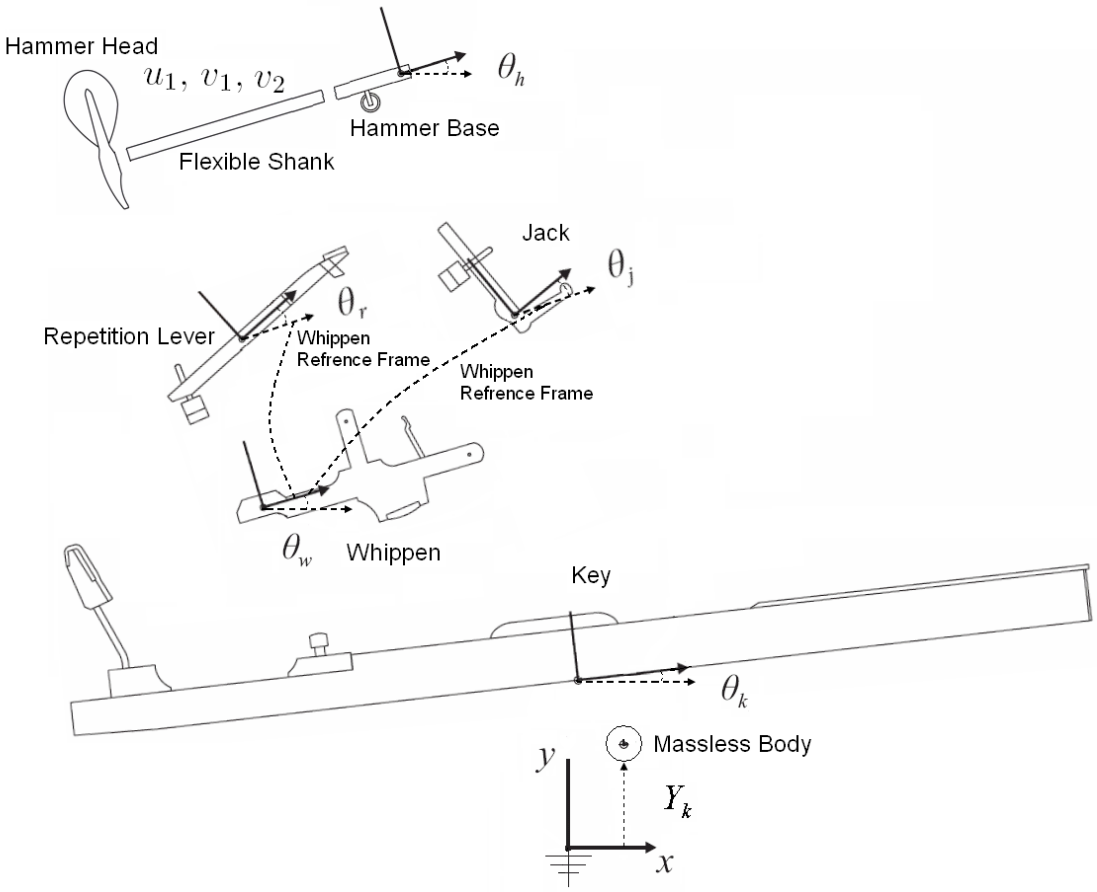

Figure 3.4: Variables of the Action Model

[2]The system variables of the piano action model proposed by Hirschkorn et al. [2] were: θ_k, θ_w, θ_h, θ_j, and θ_r.

According to Figure 3.4, θ_k, θ_w, and θ_h are the angles measured counterclockwise from the ground coordinate system to the local coordinate systems attached to the key, whippen, and hammer base, respectively. However, θ_j and θ_r are the angles measured counterclockwise from the local coordinate system of the whippen to the local coordinate systems attached to the jack and repetition lever. Y_k is the vertical displacement of the key along the prismatic joint, measured from the rest position of the key in the positive direction of the y axis of the ground coordinate system. u_1 is the longitudinal generalized elastic coordinate, and v_1 and v_2 are the two bending generalized elastic coordinates[3].

The set of eight Ordinary Differential Equations (ODEs) generated by DynaFlexPro has the following form

$$[M]\{\ddot{q}\} = \{F\} \tag{3.1}$$

where M is the mass matrix of the system, and F is a vector of quadratic velocity terms (e.g., centripetal acceleration), gravitational, and contact forces[4].

3.2 Contact Mechanics

There are 14 contact locations in this mechanism, presented in Figure 3.5[5]. The materials at the contacting surfaces are felt and leather. Hirschkorn et al. [2] proposed a modified Hunt and Crossley model [8] to represent the mechanical behaviour of these materials in contact. The contact force includes both normal and friction forces, with the following expression for the normal component of the contact force:

$$f_n = f_{fit}(x)(1 + D\dot{x}) \tag{3.2}$$

where x is the penetration depth, $\dot{x}$ is the relative normal speed, and D is the damping factor. The function f_{fit} is the nonlinear spring force, calculated from a third-order polynomial fit curve of the form,

$$f_{fit}(x) = ax^3 + bx^2 + cx \tag{3.3}$$

[3]In Section 3.5, it is explained why only three generalized elastic coordinates are used for the flexible beam.

[4]The expanded form of these equations is too large to show; however, it can be provided upon request.

[5]The content of this section is derived from the Hirschkorn's thesis [2].

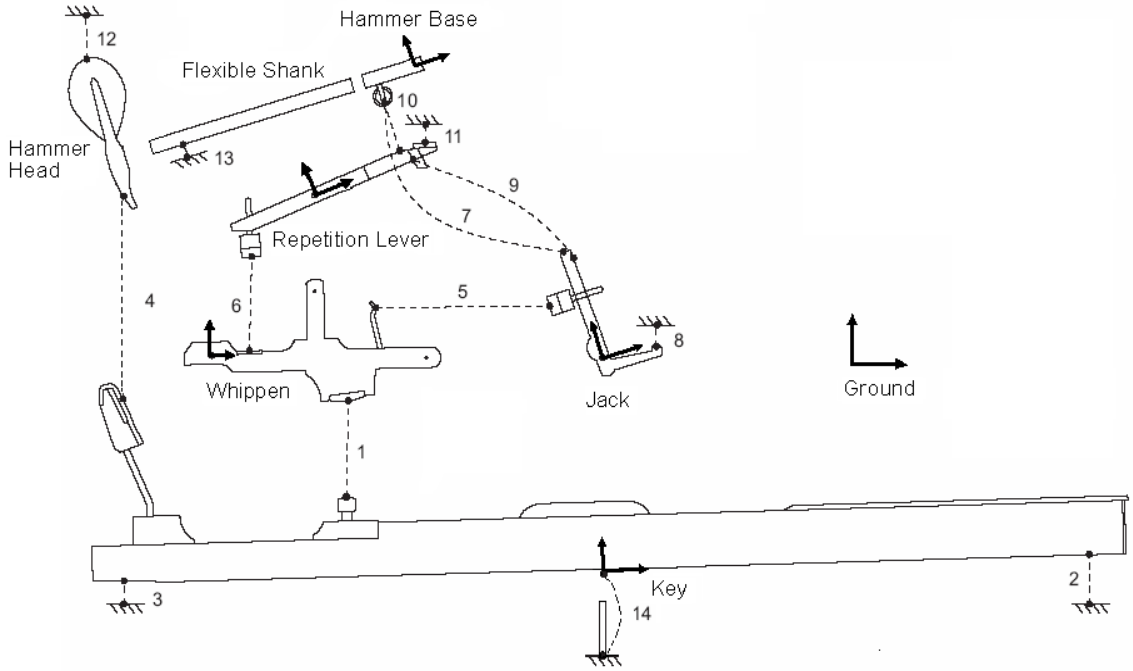

Figure 3.5: Contact Locations in the Piano Action Mechanism

The same contact model is adopted in this work. Hirschkorn determined the parameters (a, b, c, and D) of the model by performing a loading experiment for each contact location in the mechanism [2]. The typical results for the normal force during loading and unloading, and the resulting fit curve are shown in Figure 3.6.

The weakness of this model is that the hysteretic damping behaviour is speed-dependent, and it is known from previous research (Stamm [33]) that the behaviour of the real felt is not. The effect of this discrepancy, however, can be minimized by choosing a damping term (D) that produces the best reaction forces at speeds similar to those seen in the piano action for a given finger force profile.

3.3 Contact Detection

In order to determine whether the bodies are in contact, regardless of the form of the contact model, contact detection is necessary. Contact detection depends on the geometries of the

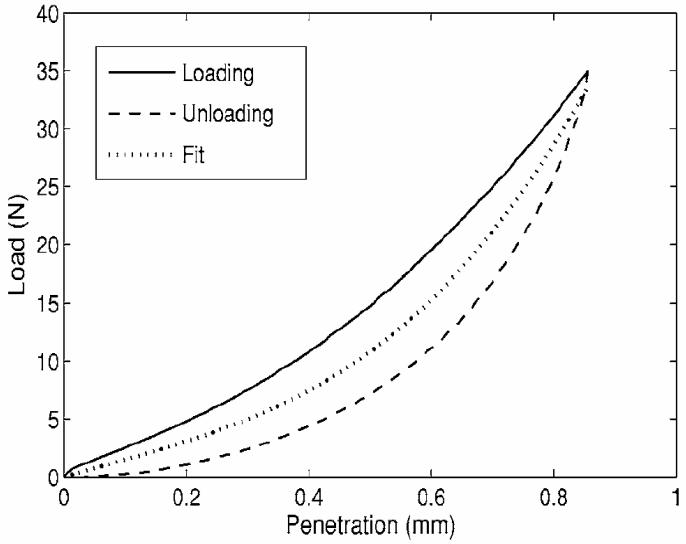

Figure 3.6: Contact Force during Loading and Unloading [2]

contact surfaces and the positions of the bodies, i.e., different geometries require different calculations.

For the contact surfaces in the piano mechanism, three different geometries were considered: circle, line, and a hybrid surface that consists of an arc with two lines extending tangentially from each end. It turned out that these three shapes can reasonably represent all the contact surfaces found in the action.

All 14 contacts and their types are listed in Table 3.1. The form of the calculation used to determine the contact force is not affected by the geometry chosen for each contact. The geometry of the contact only determines whether the bodies are in contact, and the penetration depth. Therefore, certain contact types can be used in situations where they might not closely resemble the physical shape of the bodies. For instance, the felt under the front of the key is actually a flat, horizontal disk, but treating it as a circular contact with a large radius can still produce the correct penetration depth.

Contact	Description	Type
1	Key - Whippen at Capstan	Circle - Circle
2	Key - Ground at Key Front	Line - Circle
3	Key - Ground at Key Back	Line - Circle
4	Key - Hammer at Back Check	Line - Circle
5	Whippen - Jack	Line - Circle
6	Whippen - Repetition	Line - Circle
7	Jack - Hammer at Knuckle	Hybrid - Circle
8	Jack - Ground at Button	Circle - Line
9	Jack - Repetition	Line - Circle
10	Repetition - Hammer at Knuckle	Hybrid - Circle
11	Repetition - Ground at Stop	Line - Circle
12	Hammer - Ground at String	Circle - Line
13	Hammer - Ground at Rest	Circle - Line
14	Massless Body - Ground at Key Pin	Circle - Line

Table 3.1: Contact Types in Piano Action

3.4 Tangential Friction Model

The same simple friction model, based on the Coulomb friction law that was used in [2], was chosen to model the tangential friction force in this work.

The Coulomb friction law states that if two bodies are in contact with no relative motion, a friction force f_t exists that resists any motion, as long as the force does not exceed $\mu_s f_n$, and is calculated by

$$f_t \leq \mu_s f_n \tag{3.4}$$

where μ_s is the static coefficient of friction, and f_n is the normal force at the contact, as determined from Equation (3.2).

If there is motion between the bodies, the resisting friction force is determined from

$$f_t = \mu_k f_n \tag{3.5}$$

where μ_k is the kinetic coefficient of friction.

One common method of modelling the Coulomb friction is to create a piecewise curve, based on the tangential speed of the bodies, as seen in Figure 3.7, which approximates the behaviour of friction.

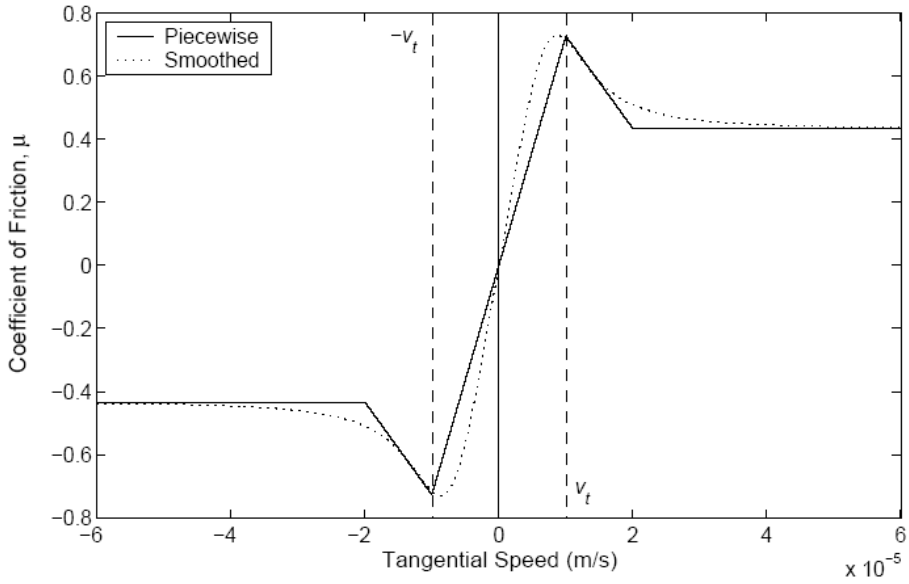

Figure 3.7: Piecewise and Smoothed Friction Curves [2]

The coefficient of friction linearly increases, until it reaches the maximum static friction coefficient value, when the tangential speed reaches the threshold velocity. This simulates the fact that when there is no (or very little) relative velocity between the surfaces, the friction force opposes the motion up to the static coefficient of friction. Once the relative tangential speed exceeds the threshold velocity, the friction coefficient is reduced to the kinetic coefficient of friction.

Since piecewise curves can cause difficulty in numerical simulations, a smoothed friction curve was chosen instead. Based on the relation (slightly modified from Cull and Tucker [34])

$$\mu = A\left(\tanh(s_t/v_t) + \frac{B_1 s_t/v_t}{1 + B_2(s_t/v_t)^4}\right) \tag{3.6}$$

where μ is the coefficient of friction, A, B_1, and B_2 are constants that are determined from

the static and kinetic coefficients of friction, s_t is the relative tangential speed of the two contacting surfaces, and v_t is the threshold velocity. A sample of this curve is given in Figure 3.7. The tangential friction force is then calculated from

$$f_t = \mu f_n \tag{3.7}$$

in which f_n is computed from Equation (3.2). When the relative tangential speed becomes large, the coefficient of friction approaches A. This means that the constant, A, is chosen to be the kinetic coefficient of friction. B_1 and B_2 are manually adjusted so that the maximum peak of the curve matches the static coefficient of friction.

This smoothed Coulomb friction model was used for the four contacts that undergo significant tangential motion: 1, 4, 7, and 10 in Table 3.1. The tangential friction was ignored for the other contacts, since the system constraints allow very little tangential movement.

A similar model was used for rotational friction in the five pin joints. The same type of curve was used to relate the torque on the joint to the rotational speed of the body. The only difference is that the torque is not dependent on any normal force. The friction in the joints is primarily determined by the tightness of the felt bushings (i.e., a large pin in a small hole), which is constant once the action is assembled. This modified form is

$$T = E\left(\tanh(\omega/\omega_t) + \frac{F_1\omega/\omega_t}{1 + F_2(\omega/\omega_t)^4}\right) \tag{3.8}$$

where T is the resulting torque, E, F_1, and F_2 are constants determined from the measured torque in the joint, ω is the rotational speed, and ω_t is the threshold rotational speed.

3.5 Dynamics of the Rayleigh Beam

The Rayleigh beam model [37], combined with a complete second-order deformation field and Rayleigh-Ritz discretization scheme [4], has been incorporated into DynaFlexPro. In this software, Taylor, Legendre, and Chebyshev polynomials can be used as the shape function. The Rayleigh beam model can be used to model any flexible beam as long as shear effects are negligible.

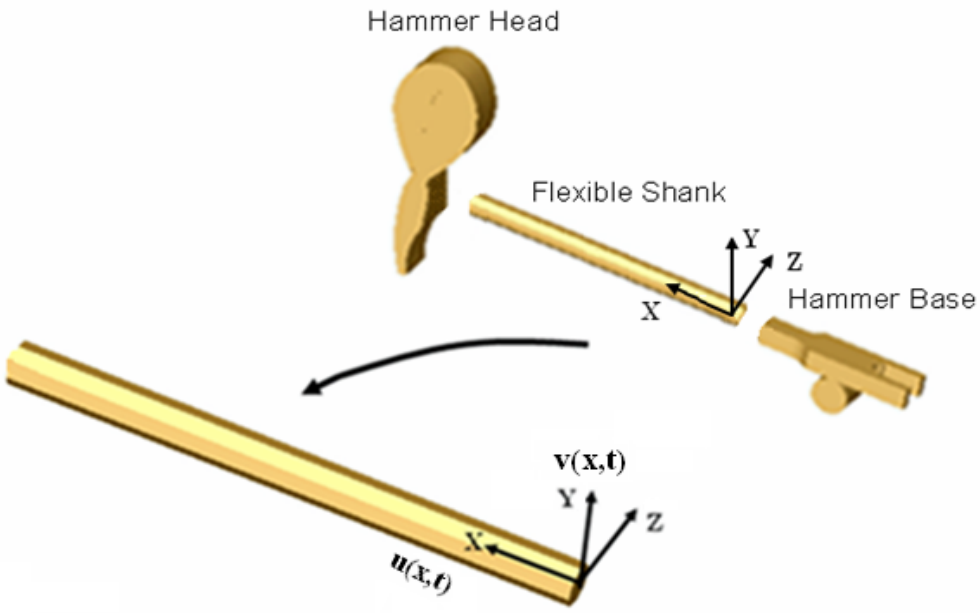

Figure 3.8: Hammer Shank

The hammer shank for which a flexible beam model was considered is shown in Figure 3.8. Since the motion of the hammer shank is planar, only two deformation variables, i.e., $u(x,t)$, the pure axial deformation of the centroidal axis along the X axis, and $v(x,t)$, the transverse deformation of the beam about the Z axis, are needed to describe the deformation of the beam.

The Taylor polynomial was used as the shape function and by doing a convergence study it turned out that one longitudinal generalized elastic coordinate and two bending generalized elastic coordinates are enough for capturing all of the relevant vibration modes of the hammer shank for the *forte* force profile in Figure 2.11. This choice of shape function is represented by *u1200* which simply means that the number of generalized elastic coordinates in the axial and transverse directions is one and two, respectively. Also, there is no deflection in the other transverse direction and the torsion of the beam is zero.

The results of the convergence study are shown in Figure 3.9. On the first column of this figure, the first, second, and third plots show the deflections of the end point of the hammer shank for the *u1100*, *u1200*, and *u2300* choices of shape function. The first

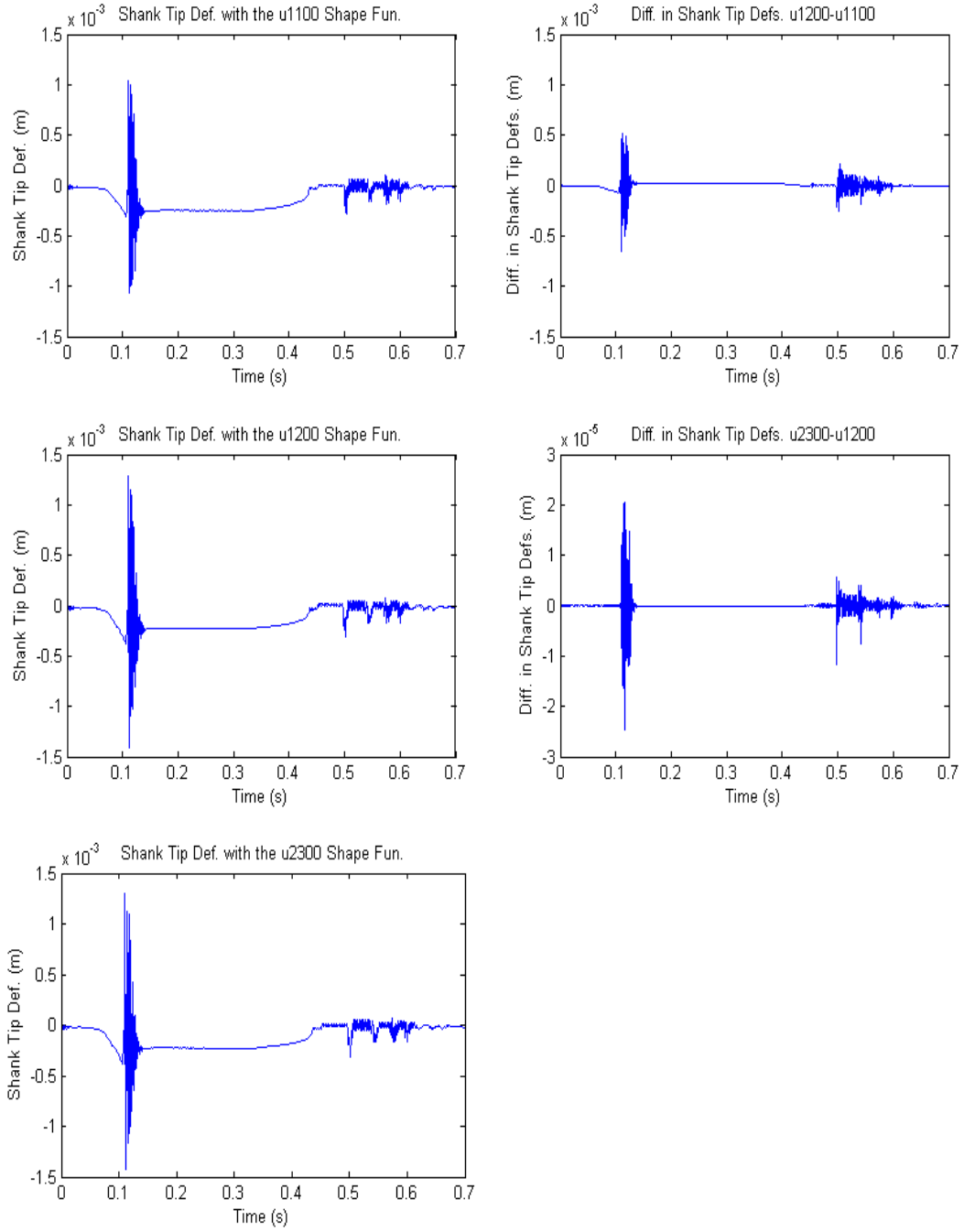

Figure 3.9: Computation of the Hammer Shank Deflection with Different Shape Function Choices

plot on the second column of this figure shows the difference between the hammer shank deflections obtained from the *u1100* and *u1200* choices of shape function. The second plot on the same column shows the difference between the hammer shank deflections obtained by the *u1200* and *u2300* choices of shape function. From these two plots, it can be seen that the difference between the hammer shank deflection obtained from *u1200* and *u2300* choices of shape function is quite negligible (as opposed to that of *u1100* and *u1200* choices of shape function), and therefore is was concluded that the *u1200* choice of shape function provides accurate results.

3.6 Regulation of the Piano Action Model

As the result of expansion and contraction of wood and compression and wear of felt, piano action components tend to change over time. To compensate for these changes, the relative orientation of action components is designed to be adjustable. For example, to adjust the height of the capstan, it can be screwed in or out. Also, to adjust the dip of the key, washers can be placed under the key front, and the back check metallic arm can be bent to change its position. Doing these adjustments is called the *regulation* process, and it should be performed regularly to maintain the proper feel and response of the piano. This process is outlined in *Steinway and Sons* manual [7].

The regulation adjustments are extremely fine and it is impossible in practice to transfer all of the measurements from a properly regulated action to a model and expect the model to be precisely regulated like the real action. For this reason, once the geometry parameters of the components are determined, for fine-tuning the regulation procedure is performed on the model, as well.

With references to the locations labeled in Figure 3.10, the regulation procedure is outlined as follows:

1. By placing small paper washers under the felt at the front of the key, the key dip is adjusted. The key front should travel 10.0 mm, at rest until it hits the felt under the key front.

2. The hammer height at rest should be 48.0 mm. This is adjusted by screwing the

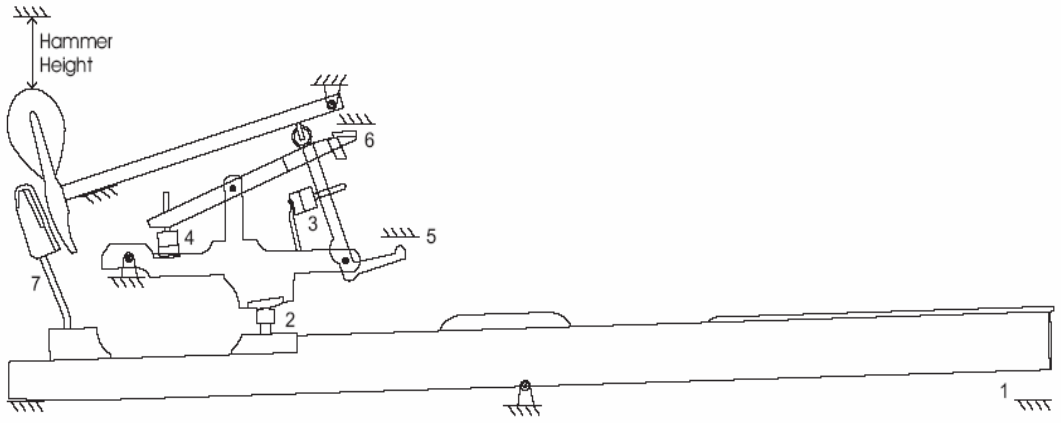

Figure 3.10: Key Points for the Regulation of the Piano Action

capstan in or out.

3. By screwing the rest pad in or out the rest position of the jack is adjusted. The right side of the jack should be aligned with the right edge of the knuckle post.

4. The rest position of the repetition lever is adjusted by the screw on the felt pad. The repetition lever should be at the same height as the jack under the knuckle.

5. The button above the toe of the jack is adjusted so that when the hammer height is 1.0 mm below the string, the jack rotates out from under the knuckle.

6. The screw above the repetition lever should be adjusted so that once the jack releases from the hammer, and it rests on the repetition, the hammer height is 3.0 mm.

7. The back check location is adjusted by bending the metal wire connecting it to the key. Under a medium blow, the hammer should be caught by the back check when the hammer height is 15.0 mm.

3.7 Initial Conditions and Numerical Solution

To solve the ODEs of the piano action mechanism, initial conditions for the nine modelling variables are required. To find the initial conditions for the modelling variables, first the

regulation requirements outlined in Section 3.6 should be met by the model. Once these requirements are satisfied, the components of the piano model are raised and allowed to settle under gravity with a zero force input on the key front. Then, the final values of the nine modelling variables at static equilibrium are picked as the initial conditions (Table 3.2).

$\theta_h(0)$	0.293 (rad)
$\theta_j(0)$	0.337 (rad)
$\theta_k(0)$	0.032 (rad)
$\theta_r(0)$	0.377 (rad)
$\theta_w(0)$	0.025 (rad)
$uf_1(0)$	0.000 (m/m)
$vf_1(0)$	0.000 (mm^{-1})
$vf_2(0)$	0.000 (mm^{-2})
$Y_k(0)$	0.490×10^{-4} (m)

Table 3.2: Sample Initial Values of the Piano Modelling Variables

The Maple lsode[backfull] stiff ODE solver, with absolute and relative tolerances of 10^{-6} and 10^{-13}, respectively, was used to solve the piano action ODEs [11]. It was found that the solvers dedicated to stiff systems were much more efficient for this system. The contacts in the system are very stiff with forces that change drastically with small variations in the position of the contacting surfaces. The Rayleigh beam model introduces a strong structural spring into the equations of the piano action model, and therefore is another contributing factor in the stiffness of the system ODEs.

A convergence study indicated that these error tolerances were sufficient to avoid inaccuracies in the results. The maximum relative difference between the results for the hammer shank deflection, from the relative tolerance of 10^{-13} to the relative tolerance of 10^{-14} with the same absolute tolerance of 10^{-6}, was only 0.004 percent. This value was 0.002 percent, where the relative tolerance was kept constant at 10^{-13}, and the absolute tolerance was changed from 10^{-6} to 10^{-7}.

Running a complete simulation, for the system with the force profile in Figure 2.11 as

the input to the piano action, requires about 75 minutes on a 2.4 GHz PC computer. This is true for the case when the hammer shank and the connection of the key to the ground have been modelled with a flexible beam and a prismatic-revolute joint, respectively. However, the Maple environment is not the most efficient platform for running simulations in terms of time, and the simulation time can be significantly reduced by implementing the model and solvers in a dedicated, compiled language such as C.

The model solution is compared to the experimental results in Chapter 5.

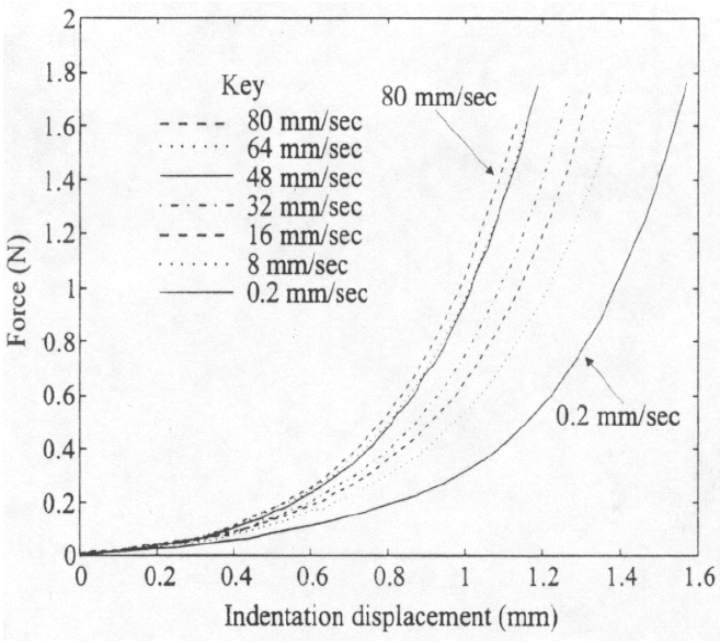

Figure 3.11: Force Response of a Fingertip as a Function of the Indentation for the Constant Velocities of Indentation (Loading Curve Only) [28]

3.8 Biomechanical Model of the Fingertip

As it is mentioned in Section 1.3.3, to represent the characteristics of the fingertip pulp, the non-linear spring-damper model in Figure 1.7 was proposed. This model closely reproduces

Pawluk's experimental data [28] shown in Figure 3.11[6]. The following discussion explains why this model has been proposed.

The existence of a static stiffness in the fingerpad, observed in the curve corresponding to 0.2 mm/s velocity of indentation, in the experimental data of Pawluk in Figure 3.11, suggests that even the simplest model, describing the fingerpad force response to an arbitrary indentation, must contain a spring. Furthermore, the stiffness of this spring must be an exponential function of the displacement to describe the quasi-static force response correctly (in Figure 3.11, the force profile corresponding to the 0.2 mm/s velocity of indentation has an exponential form). Since the force response also changes with the velocity, a damper must be included in the model. To achieve a static response, the damper must be parallel with the spring. To maintain the exponential force response for all the constant-velocity trajectories, the damping constant must also be an exponential function of the displacement. However, a model, including a spring and a damper in parallel, is incomplete since it predicts that by increasing the velocity, the force response increases without any limitation. Therefore, to limit the maximum of the force response as a function of velocity, it is necessary to add a spring in series with the damper. To make the instantaneous stiffness an exponential function of the position, the spring constant of this series spring needs to be an exponential function of the position, too. As a result, the simplest and most primitive model, which can conceptually describe the fingerpad force response to the indentation profiles with constant velocity, is a Kelvin model [31] whose components are exponentially dependent on the displacement, as depicted in Figure 3.12 with the following governing equations.

$$K = f_1(X) = a_1 e^{b_1 X}$$
$$K_2 = f_2(X_2) = a_2 e^{b_2 X_2}$$
$$C_1 = f_3(X_1) = a_3 e^{b_3 X_1}$$

For this proposed model, by using the governing equations for the coefficients of the damper and springs, the external force and indentation are related to each other. These equations

[6]For the *piano* and *forte* blows the contact force range of 0-5 and 0-30 Newtons and velocity range of 0-250 and 0-675 mm/s are common, respectively [2]. Therefore, Pawluk's experimental data is not very appropriate for the fingertip model for the piano application.

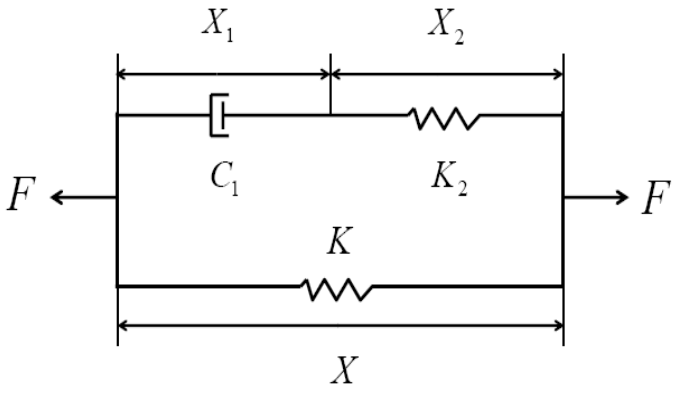

Figure 3.12: Kelvin Model

exponentially relate the coefficients of the springs and damper to the displacement and velocity, respectively, in the simplest possible form. The model parameters a_1, a_2, a_3, b_1, b_2, and b_3 are determined from the experimental data.

In Figure 3.12, F is the tensile force, and X is the total indentation which is equal to (X_1+X_2). The relationship between F and X is established as follows:

From geometry,

$$X_1 = X - X_2 \tag{3.9}$$

From equilibrium,

$$C_1 \frac{d(X - X_2)}{dt} = K_2 X_2 \tag{3.10}$$

$$F = KX + K_2 X_2 = KX + C_1 \frac{dX_1}{dt} \tag{3.11}$$

From (3.10) and (4.11), respectively, it can be concluded that

$$\begin{aligned} \frac{dX_2}{dt} &= \frac{dX}{dt} - \frac{dX_1}{dt} \\ &= \frac{dX}{dt} - \frac{(a_2 e^{(b_2 X_2)} X_2)}{(a_3 e^{(b_3 (X - X_2))})} \end{aligned} \tag{3.12}$$

$$F = a_1 e^{(b_1 X)} X + a_2 e^{(b_2 X_2)} X_2 \tag{3.13}$$

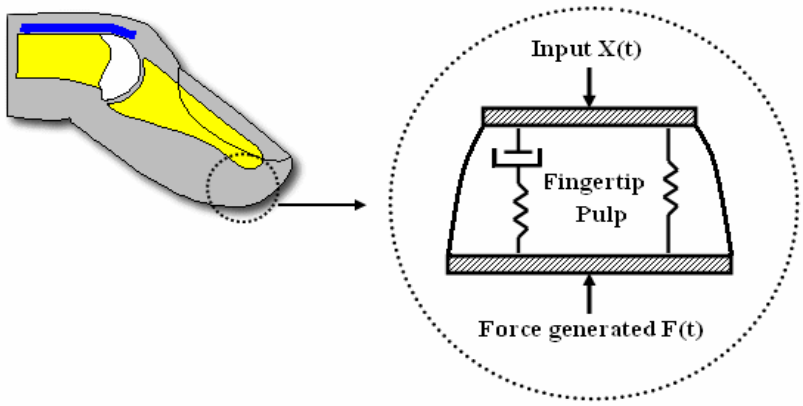

Figure 3.13: Correspondence between the Proposed Model and the Actual Fingertip Pulp

Equations (3.12) and (3.13) are the governing equations of this model, relating F and X to each other. The differential equation (3.12) is solved for X_2 for a given X and, by substituting X_2 in Equation (3.13), F is calculated.

Figure 3.13 exhibits the correspondence between the proposed model and the actual fingertip pulp. This model only represents the mechanical properties of the fingertip under pressure, when this mechanical model is under tension. The mechanical properties of the fingertip during the unloading phase cannot be simulated with this model.

The parameters of the model (a_1, a_2, a_3, b_1, b_2, and b_3) should be determined so that the model best predicts the experimental data. The experimental data from Pawluk, illustrated in Figure 3.11, was used to determine the parameters of the model.

An iterative method, shown in Figure 3.15, is implemented to determine the model parameters. By considering two extreme cases, the initial values for the six model parameters were estimated. By running the iterative algorithm, the values of the model parameters converged and at that point, the iterative algorithm was stopped and the final values were picked.

The two extreme cases, based on which the initial values of the six model parameters were selected, were as follows. By assuming that the indentation profile has a constant speed, then at a very high speed of indentation, the damper force is high and X_1 is negligible, and it can be assumed that $X_2 \approx X$. On the other hand, at a very low speed of indentation, X_2 is negligible and it follows that $X_1 \approx X$. In the former case, from Equation (3.11) it is concluded ($X_2 \approx X$)

$$F \approx KX + K_2X = a_1e^{(b_1X)}X + a_2e^{(b_2X)}X \tag{3.14}$$

In the latter case, from Equation (3.11) it is concluded ($X_1 \approx X$)

$$F \approx KX + C_1\frac{dX}{dt} = a_1e^{(b_1X)}X + a_3e^{(b_3(X))}\frac{d(X)}{dt} \tag{3.15}$$

Equations (3.14) and (3.15) are functions of indentation (X) only, and are valid for a very high-speed and a very low-speed indentation, respectively. The experimental data from Figure 3.11 is used[7] to determine $a1$, $a2$, $a3$, $b1$, $b2$, and $b3$. First, (3.15) should be fit to the lowest speed force profile (0.2 mm/s) in Figure 3.11. By using the *lsqcurvefit*[8] function in *MATLAB*, this can be done. a_1, a_3, b_1, and b_3 are obtained as follows:

$$a_1 = 0.0000 \text{ N/mm}, \quad a_3 = 0.0979 \text{ N} \cdot \text{s/mm}, \quad b_1 = 12.5966 \text{ mm}^{-1}, \text{and} \quad b_3 = 2.7481 \text{ mm}^{-1}$$

Equation (3.14) should be fit to the highest speed force profile (80 mm/s) in Figure 3.11. By knowing a_1 and b_1 from the previous step, a_2 and b_2 are found by using the *lsqcurvefit* function in *MATLAB*. The results are

$$a_2 = 0.1046 \text{ N/mm} \text{ and } b_2 = 2.3269 \text{ mm}^{-1}$$

These initial values are verified to see how realistic they are. By substituting these values in equations (3.12) and (3.13), these equations are numerically solved to see whether the force profiles, obtained from them for the high speed and low speed of indentations, (80mm/s and 0.2 mm/s), matched the corresponding force profiles of Figure 3.11. Figure

[7] The *Autocad* software was used to extract the data from the curves in Figure 3.11.

[8] *lsqcurvefit* solves non-linear curve-fitting problems. It fits the given input and output data to a user-defined non-linear function.

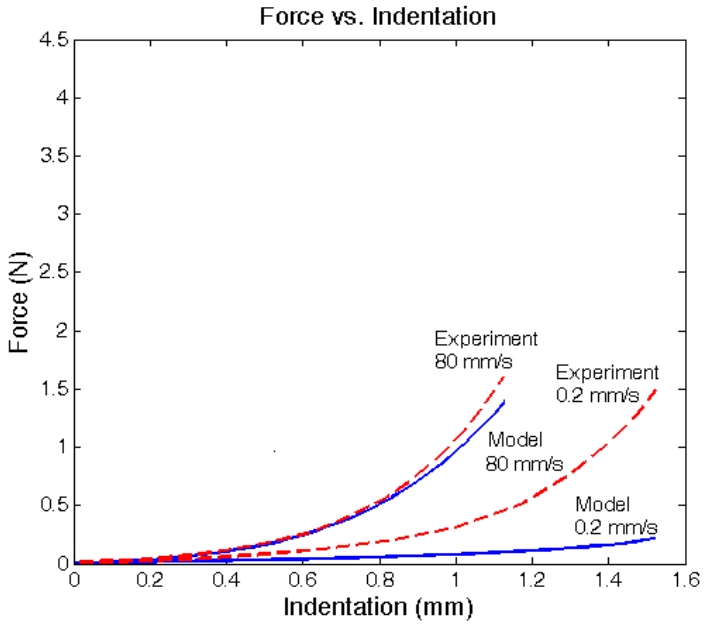

Figure 3.14: Force Response of the Model to Two Different Ramp Trajectory Inputs Compared with the Same Experimental Results

3.14 shows the results of the comparison. It can be seen that there is a close match between the model and experimental results for the indentation velocity of 80 mm/s. For the indentation velocity of 0.2 mm/s, however, the discrepancy is high. Based on this observation, the obtained initial values, seem to be good enough as the starting point of the iterative algorithm for finding a_1, a_2, a_3, b_1, b_2, and b_3.

To obtain the final values of the model parameters, the estimated initial values for the six model parameters were used in the iterative algorithm, shown in Figure 3.15. All of the experimental curves in Figure 3.11 were used in the iteration process and the following values for the six parameters of the model were obtained[9]:

$$a_1 = 0.0178 \text{ N/mm}, \quad a_2 = 0.0518 \text{ N/mm}, \quad a_3 = 0.0889 \text{ N} \cdot \text{s/mm}, \quad b_1 = 2.6177 \text{ mm}^{-1},$$

$$b_2 = 2.6788 \text{ mm}^{-1}, \text{and} \quad b_3 = 0.6919 \text{ mm}^{-1}$$

[9]With these final values of the six parameters, Figure 3.14 has been plotted again in Figure 4.15, in Section 4.3.

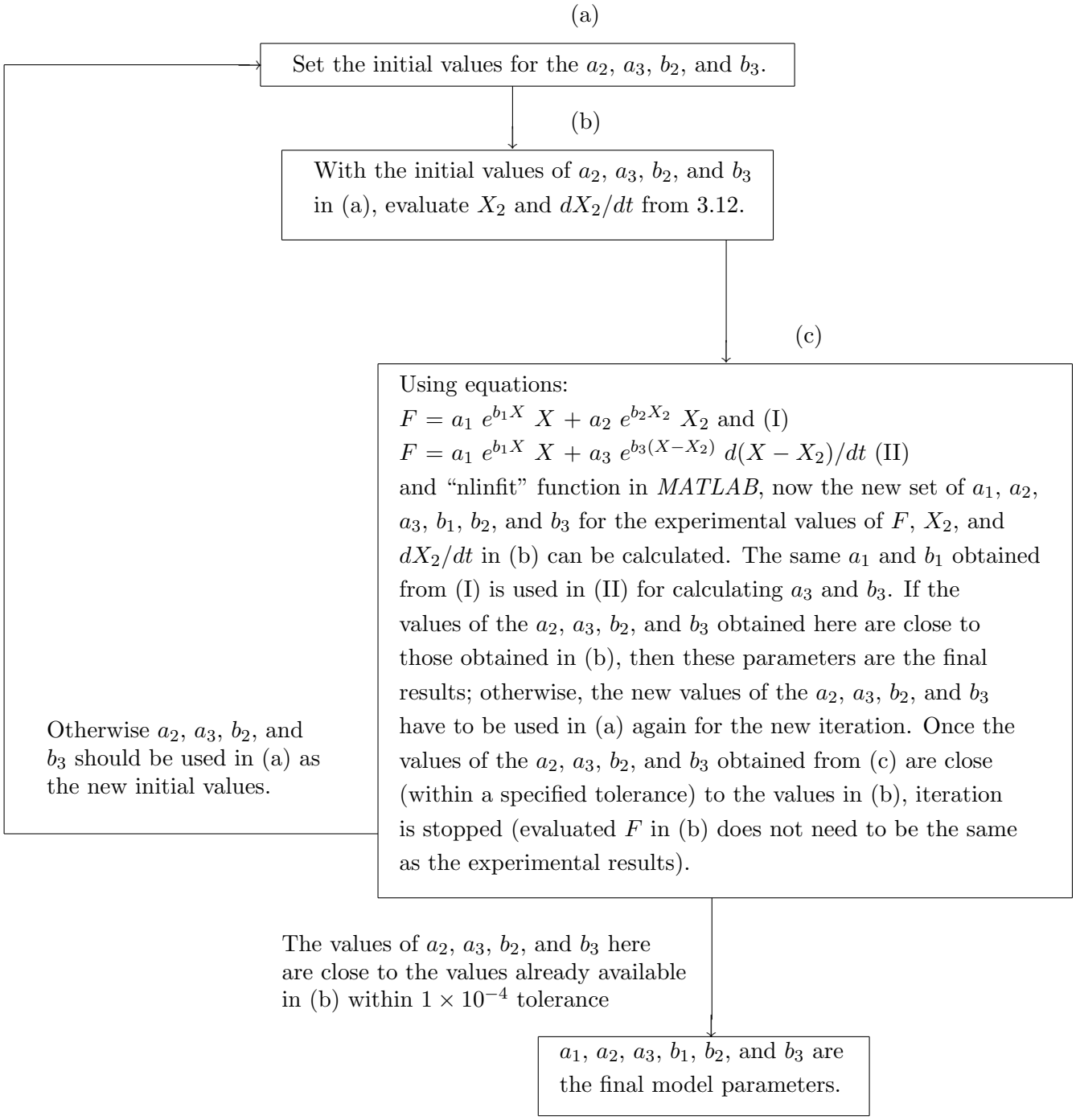

Figure 3.15: Iterative Algorithm for Finding the Parameters of the Model

Chapter 4

Simulation Results

This chapter outlines the simulation results for the piano action models with hammer shank represented by a Rayleigh beam, and the connection of the key to the ground is modelled with a revolute-prismatic joint. Also, the precision of the non-linear model, proposed for the fingertip pulp in predicting the experimental data for the force range of 0-2 N, is discussed.

4.1 Flexibility of the Hammer Shank

4.1.1 Computed Results for the Hammer Shank Deflection

To check the effect of the flexibility of the hammer shank on the response of the action, the hammer shank was modelled with the Rayleigh beam. The model of the connection of the piano key to the ground kept a revolute joint and the models of the rest of the piano action components are similar to that of [2].

Figure 4.1 exhibits the general bending shape of the hammer shank, according to the simulation results for the input force profile given in Figure 2.11. The horizontal axis on this figure is the X axis of the local reference frame on the hammer shank, illustrated in Figure 2.12, and the vertical axis shows the corresponding deflection of points along the shank at different instants in time. This figure confirms that the maximum deflection occurs at the end point of the hammer shank (first mode of vibration). Therefore, in this

thesis, the deflection of the hammer shank was studied at its end point.

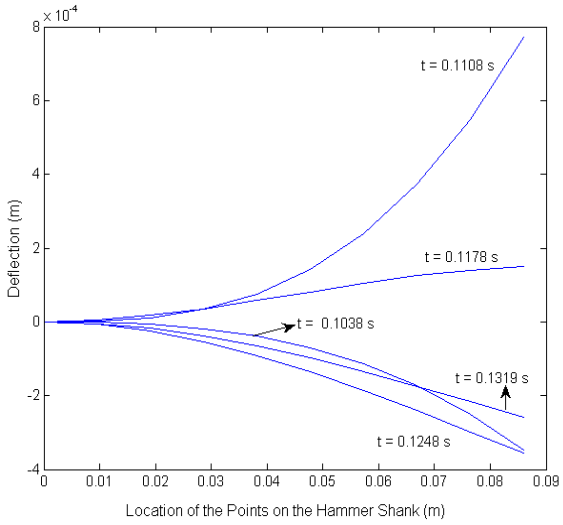

Figure 4.1: General Bending Shape of the Hammer Shank According to the Simulation Results

Figure 4.2 shows the computed lateral (Y) deflection of the end point of the hammer shank, relative to its local reference frame. The percent deflection has been calculated by dividing the deflection by the length of the beam, which is 0.086 m. According to this figure, since the maximum deflection of the shank is less than 2%, the assumption of small beam deflection, which is one of the requirements of the Rayleigh beam theory, is satisfied.

Figure 4.2 demonstrates that, as the hammer starts to accelerate, the backward deformation at the tip of the hammer shank increases. When the hammer head strikes the rigid piano string at the instant marked A (see the top left plot in Figure 4.2), the vibrations significantly spike[1]. At the B moment, 1 ms after the A moment, the contact with the rigid string ceases and the hammer head returns from the top. Measurements show that for a *forte* blow in a real piano, hammer-string impact contact times of 3-4 ms are typical. Therefore, model predicts the duration of the hammer-string contact (1 ms) fairly close to the experimental data.

[1]The maximum tip deflection during impact is about 1.5 mm.

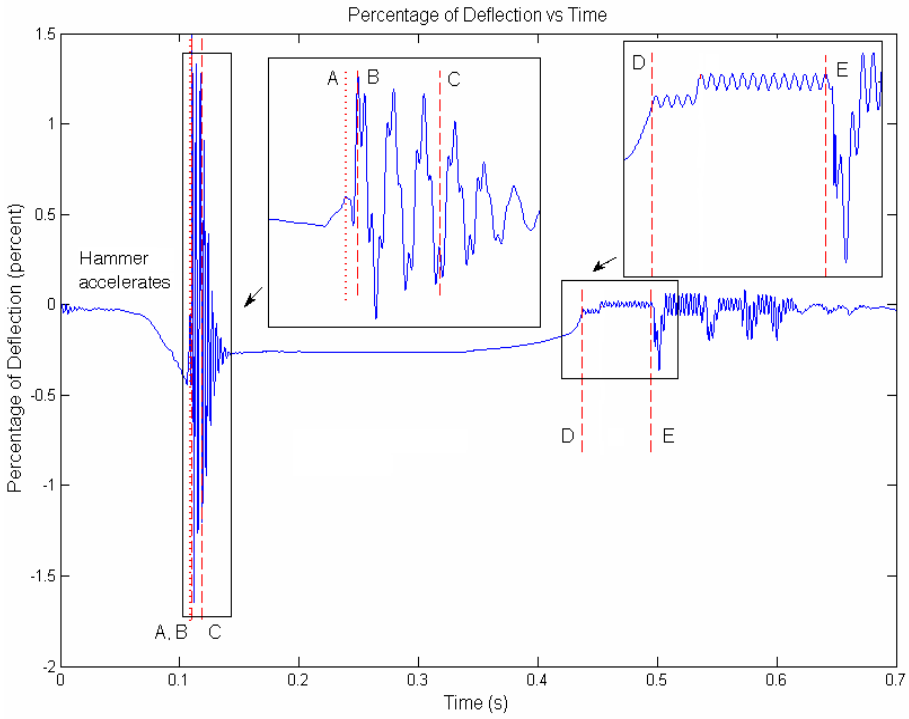

Figure 4.2: Relative Deflection of the Tip of the Hammer Shank

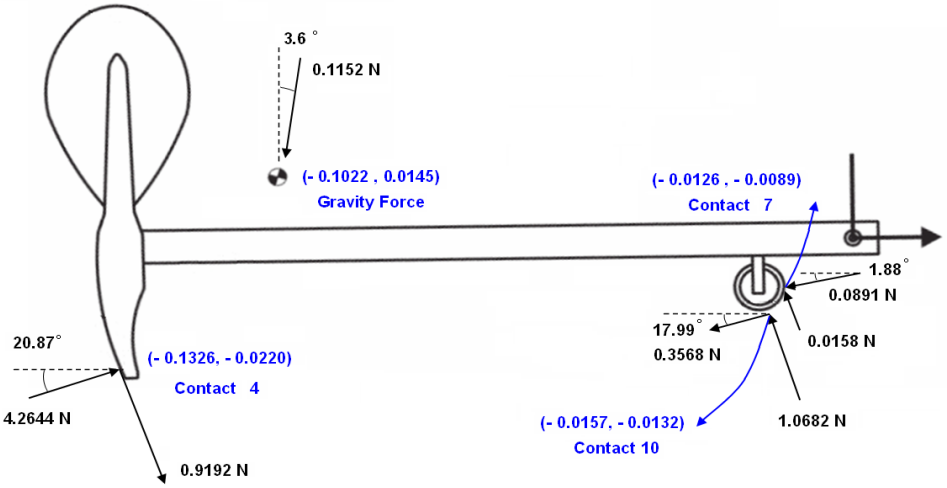

Figure 4.3: Free Body Diagram of the Hammer when it is caught at the Back Check

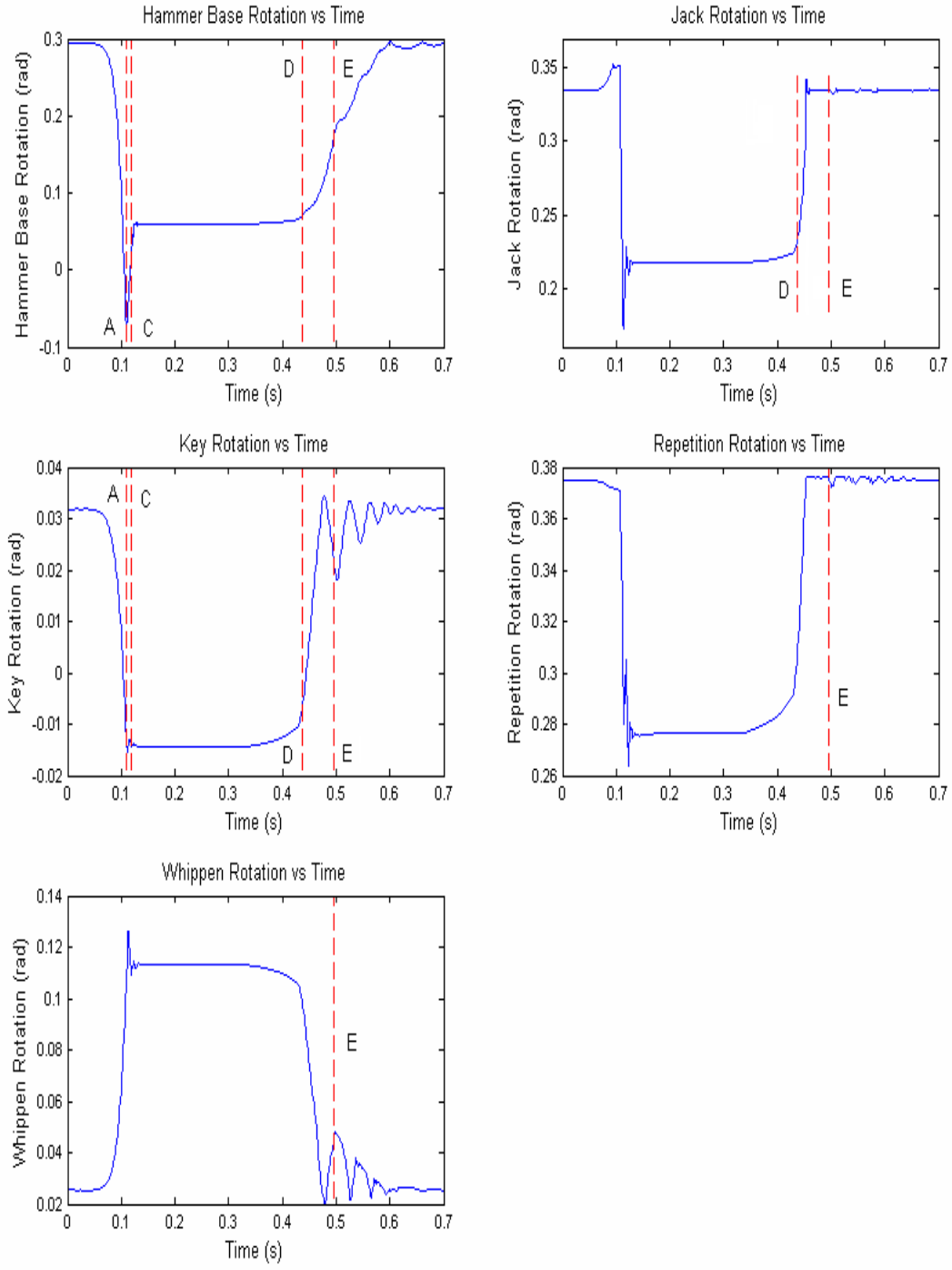

Figure 4.4: Rotation of the Main Parts of the Piano Action

At the C moment, 9 ms later, the hammer head starts its contact with the back check (see Figure 1.2 for the location of the back check). Due to the damping in this contact location, the vibrations are damped out quite quickly.

Figure 4.3 shows the free body diagram of the hammer when it is caught at the back check. On this diagram, the normal force on the back check represents the resultant force coming from the contact 4 (Figure 3.5) and back check arm (Figure 1.2). The tangential force at the back check represents the friction force. The resultant moment of the normal and tangential forces at the back check location of the hammer head, about the hammer pivot is counterclockwise[2]. This confirms the backward deflection of the hammer shank when it is caught at the back check.

Slightly before the D moment, the key begins to fall back; however, the hammer head is still in contact with the back check (the key and hammer rotation diagrams in Figure 4.4 reflect this) and simultaneously rotates with that. At the D moment, the key completely releases the hammer head at the back check.

At the E moment, the repetition lever and the jack do not have significant relative motion with respect to the whippen and therefore, the rotation of the whippen assembly can be described by the rotation of the whippen itself. As can be seen in Figure 4.4, at this moment the back of the key is bouncing on the ground and through the capstan (see Figure 1.2 for the location of the capstan) it causes the whippen to bounce on top of it.

Since, at this moment, the hammer base rests on the whippen through the knuckle, this bouncing motion of the key transfers to the hammer, accounting for the form of the hammer shank vibrations after the E moment.

The lowest vibration frequency of the hammer shank between the A and C moments and after the E moment is 303 Hz[3].

[2]The counterclockwise resultant moment of the friction and normal forces at the back check, on the piano hammer, about the hammer pivot is: 4.2644 (cos(20.87) 0.0220 - sin(20.87) 0.1326) + 0.9192 (cos(20.87) 0.1326 + sin(20.87) 0.0220) = 0.0073.

[3]By increasing the hammer shank modulus of elasticity by 10%, 20%, 30%, and 50%, the natural frequency of vibration increases to 313, 326, 344, and 370 Hz, respectively. By increasing the hammer shank density by 10%, 20%, 30%, and 50%, the natural frequency of vibration changes to 303, 303, 278, and 278 Hz, respectively.

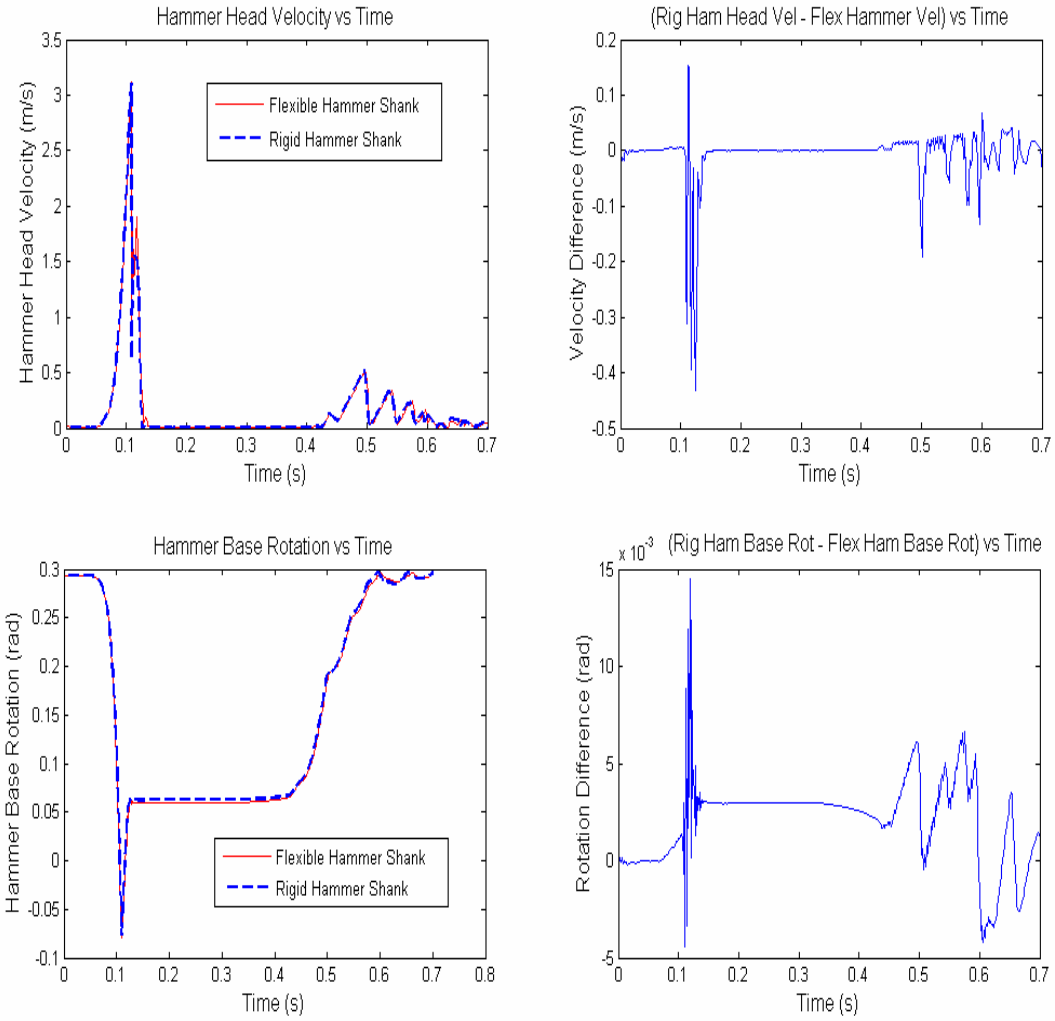

Figure 4.5: Impact Velocity and the Rotation of the Hammer for a Rigid and Flexible Shank

4.1.2 Effect of the Shank Flexibility on the Head Velocity

Since the impact velocity of the hammer head determines the string vibrations, the effect of the hammer shank flexibility on this velocity was explored. Figure 4.5 represents the hammer head impact velocity and the rotation of the hammer base for two cases: when

the hammer shank is modelled as a rigid body and when the hammer shank is modelled as a flexible body. The left hand figure shows the two curves in one diagram and the right hand figure shows the difference between them. It is calculated from these figures that the difference between the impact velocities in the two different cases reaches the maximum of 27% (using $(V_{FlexShank} - V_{RigShank})/V_{FlexShank}$) during the contact period. This difference in velocity, during the impact, might have a notable effect on the piano string vibrations. However, this result is highly dependent on the accuracy of the hammer-string contact model. Given that the current hammer-string contact model is very simple and is adjusted for the contact between the rigid bar (not an actual string) and the hammer head, more research is needed before the significance of the results can be interpreted.

4.1.3 Shank Flexibility Causes Head Scuffing Motion

The flexibility also changes the position and footprint of the contact region between the hammer head and the piano string, during the contact time. Figure 4.6 shows the piano hammer and the piano string, before the contact. If the hammer shank is modelled as a rigid body, during the contact, point A on the hammer head does not move in the x direction in the hammer base local reference frame. If the hammer shank is modelled as a flexible body, however, point A on the hammer head will have some motion along the x axis during the contact time, known as *scuffing*, in the hammer base local reference frame. This alters the footprint of the contact between the hammer head and the piano string during the contact, and this, in turn, affects the tone generated on the string.

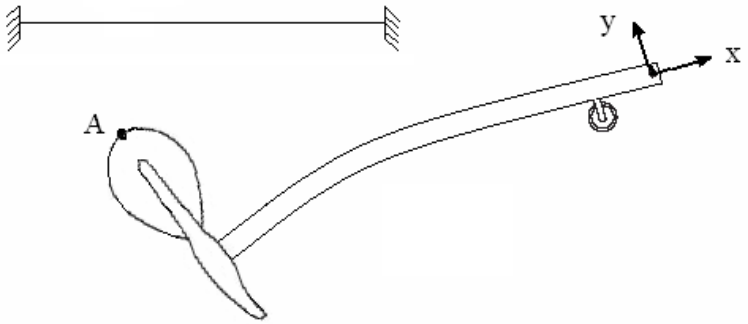

Figure 4.6: *Scuffing* Motion of the Hammer Head

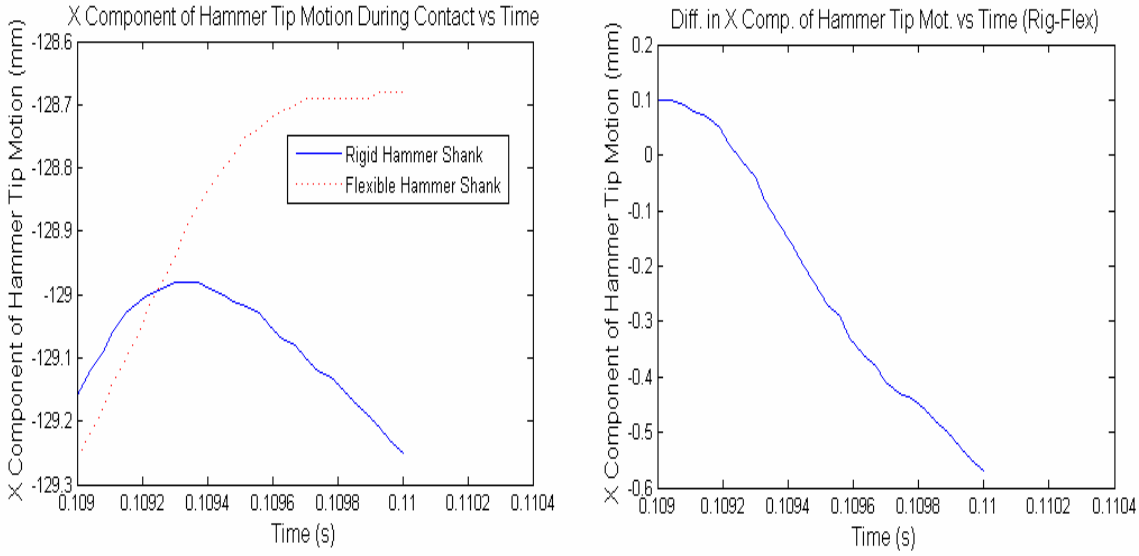

Figure 4.7: X Component of the Displacement of the Hammer Head Tip

The effect of the hammer shank flexibility on the X position of the contact point between the hammer head and the piano string, expressed in the global reference frame, is shown in Figure 4.7. Clearly, there is a significant shift in the X position of the contact point due to the shank flexibility (around 0.7 mm of extra *scuffing*), which can result in a noticeable change in the sound of the piano string.

4.1.4 Effect of the Shank Flexibility on the Rotation of the Components of the Piano Action Mechanism

When the rotation curves of a given component of the piano action mechanism with the hammer shank is modelled as a rigid body and as a flexible beam, are plotted, the difference between the curves is not distinguishable. This means that the flexibility of the hammer shank has almost no effect on the rotation of the components of the piano action mechanism.

The small percentage of difference between the rotations of the different components of the piano action is shown in Figure 4.8. Table 4.1 shows the values of the parameters

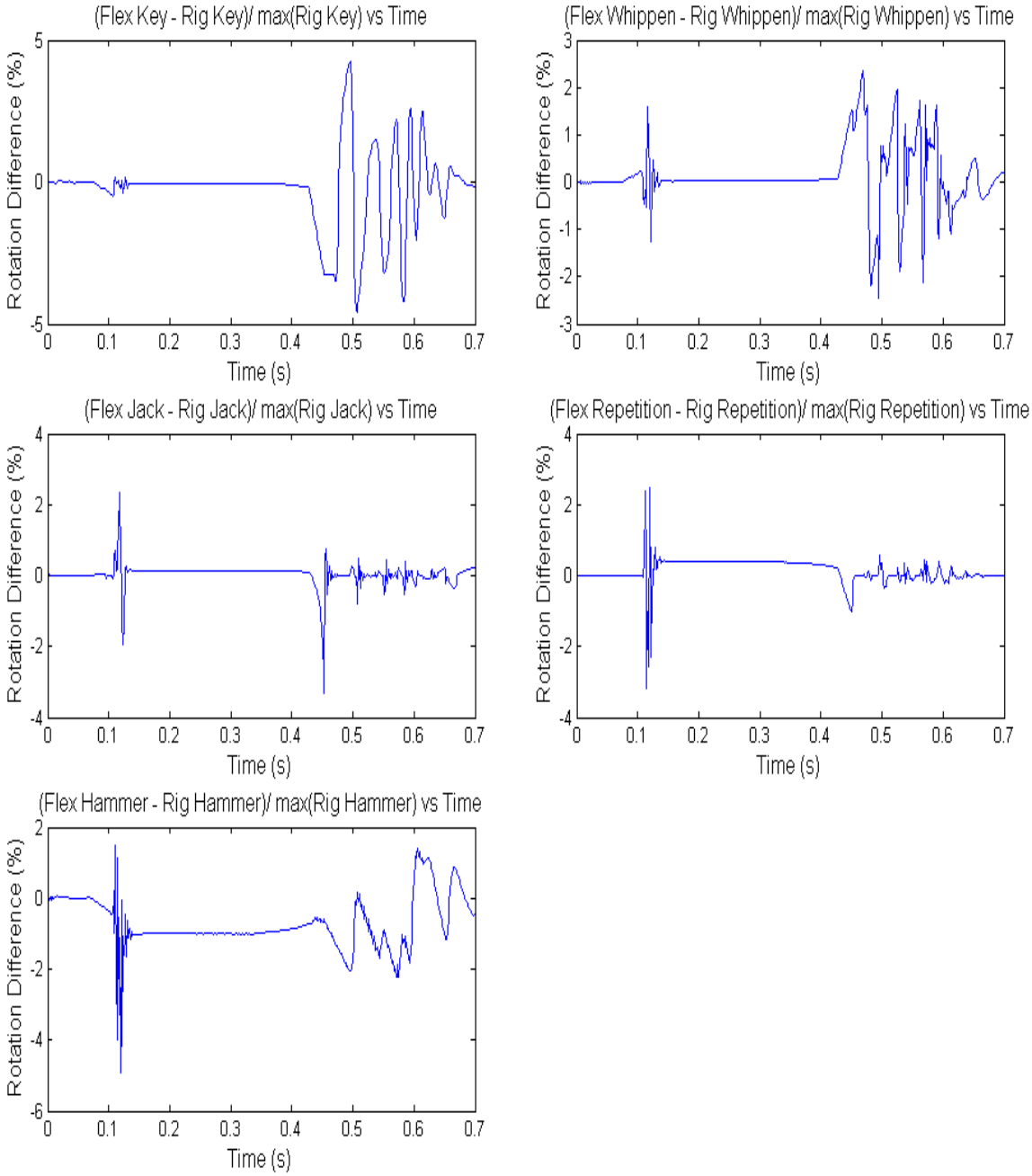

Figure 4.8: Difference between the Rotation of the Piano Components for the Rigid and Flexible Hammer Shank Cases

that have been used in calculating the percentage difference in this figure.

Max (Rig Key)	0.0345 (rad)
Max (Rig Whippen)	0.1270 (rad)
Max (Rig Jack)	0.3529 (rad)
Max (Rig Repetition)	0.3770 (rad)
Max (Rig Hammer)	0.2965 (rad)

Table 4.1: Values used in Figure 4.8

4.1.5 Comparison between Experimental and Computed Strains

To validate the computed results obtained for the flexibility of the hammer shank, a strain gauge was mounted on top of the hammer shank, as shown in Figure 2.9. With this strain gauge, for the finger force profile shown in Figure 2.11 (the same force profile that was used in the model), the strain on the top of the hammer shank was measured. The solid curve in Figure 4.9 indicates the measured strain.

Figure 4.2 represents the deflection of the hammer shank tip. To obtain comparable data with the strain gauge reading, however, it was needed to extract the strain on top of the hammer shank from the model at the location shown in Figure 2.12. The formula for measuring the axial strain by using the elastic variables of the Rayleigh beam is as follows [4]:

$$\epsilon_{xx} = H_{11} + yH_{12} + zH_{13} + H_{14} \tag{4.1}$$

in which

$$H_{11} = u' + \frac{u'^2}{2} \tag{4.2}$$

$$H_{12} = -v'' + u''v' - w''\phi \tag{4.3}$$

$$H_{13} = -w'' + u''w' + v''\phi \tag{4.4}$$

$$H_{14} = \frac{1}{2}(a_1y^2 + a_2z^2 + a_3yz) \tag{4.5}$$

$$w \equiv 0 \tag{4.6}$$

$$\phi \equiv 0 \tag{4.7}$$

$$a_1 = v''^2 + \phi'^2 \tag{4.8}$$

$$a_2 = w''^2 + \phi'^2 \tag{4.9}$$

$$a_3 = 2v''w'' \tag{4.10}$$

where the *prime* represents the derivative with respect to x. The axial and bending deflections, u and v, are obtained from equations (1.1) and (1.2) by setting $n_u = 1$ and $n_v = 2$, respectively, giving:

$$u(t,x) = xu_1(t) \tag{4.11}$$

$$v(t,x) = x^2 v_1(t) + x^3 v_2(t) \tag{4.12}$$

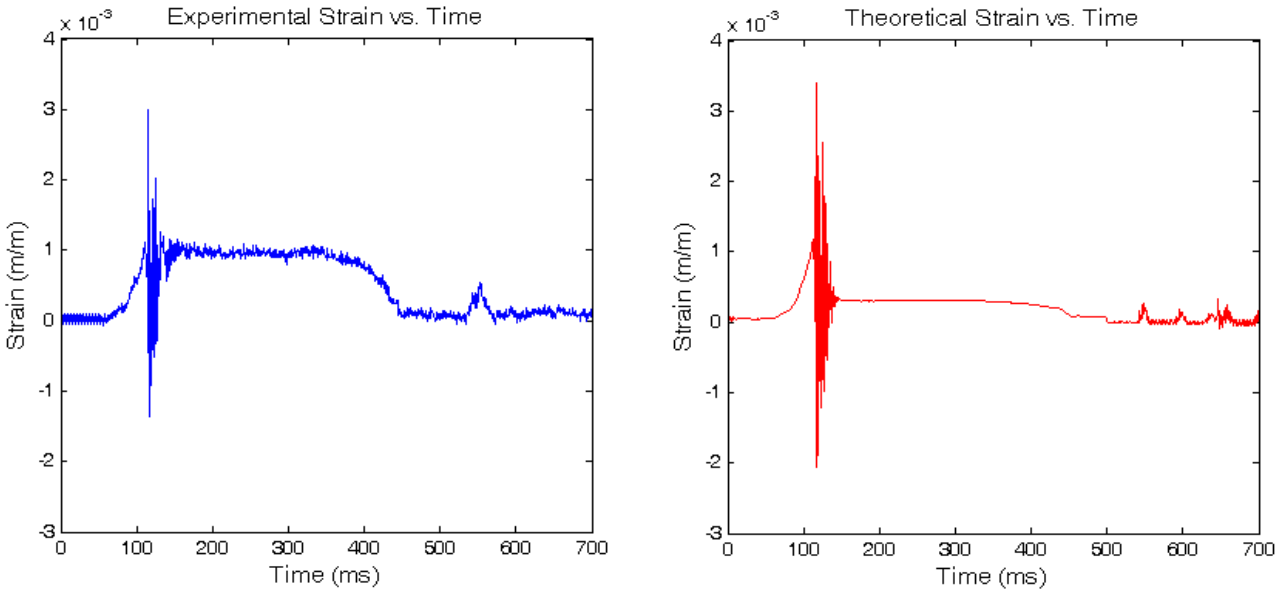

Figure 4.9: Experimental vs. Theoretical Strain Measurement

By substituting these values in the ϵ_{xx} formula, the axial strain on top of the hammer shank can be evaluated. Also, according to the reference frame in Figure 2.12, the

coordinates of the strain gauge are as follows:

$$X = 0.031\,\text{m},\ \ Y = 0.0031\,\text{m},\ \ \text{and}\ \ Z = 0\,\text{m}$$

In Figure 4.9, the right-hand side plot shows the computed strain and the left-hand side plot shows the measured strain for the piano action model. As it can be seen in this figure, the pattern of the theoretical and experimental results is the same. Also, except for the static deflection of the hammer shank when it is caught at the back check, the theoretical and experimental results are in good agreement.

The flexible beam model in DynaFlexPro software has been validated by the discrete flexible link model in the *Adams* software[4]. Therefore, the discrepancy between the curves when the hammer head is caught at the back check is unlikely due to the flexible beam model in DynaFlexPro. The strain gauge measurement is unlikely erroneous either, since the strain gauge measurement instrument has been carefully calibrated by mechanical experiments.

According to Figure 4.3, the contact and friction forces at the back check location of the hammer head have the dominant effect on the static deflection of the hammer shank. Therefore, the inaccuracy of the contact or friction model at the back check is the likely source of discrepancy between the curves.

4.2 Key Lift-off

In *forte* blows, the connection of the key to the ground allows a significant lift-off for the key at that location, when the front of the key reaches the ground. Key also lifts off when the pianist removes his finger from the key front and the back of the key falls down on the ground. Since a simple revolute joint does not allow the key to have a vertical motion at its connection point to the ground, it seemed necessary to redesign the joint model for this location. To check the effect of the key lift-off on the response of the action, a new model was considered for the connection of the key and ground.

[4] *Adams* is a software for analyzing the kinematics and dynamics of mechanical systems. *Adams* is a product of MSC Software Corporation.

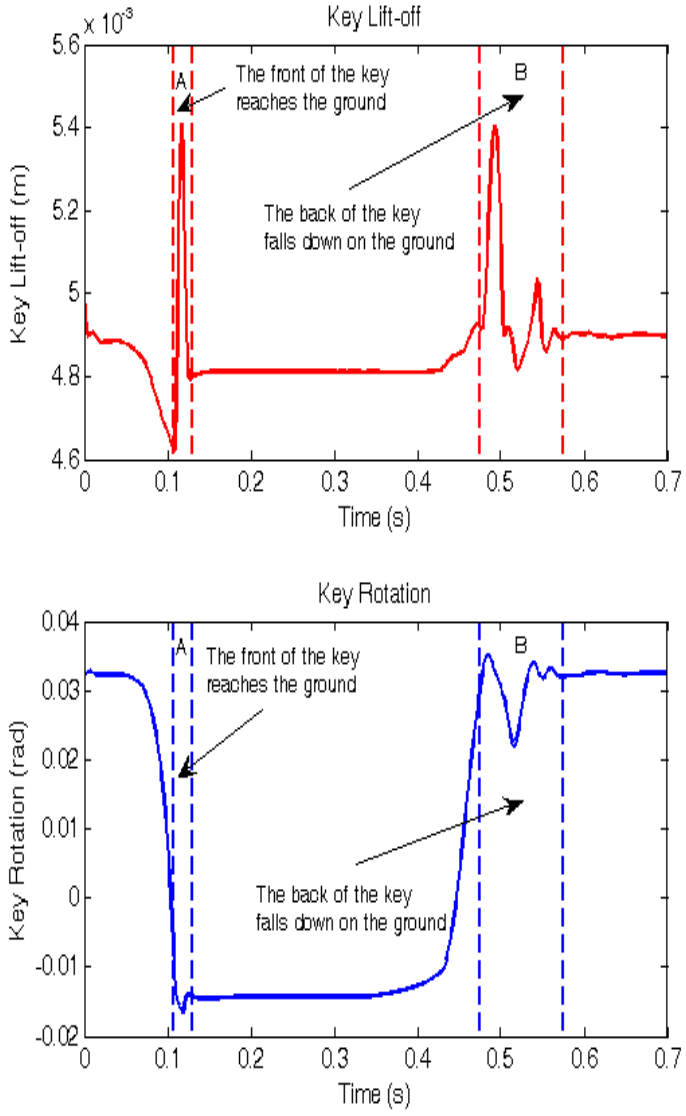

Figure 4.10: The Computed Key Lift-off and the Rotation of the Key

A massless body was added to the mechanism, and a revolute joint was placed between this body and the key. The massless body then was connected to the ground with a prismatic joint and a contact force. To model the friction between the key and vertical peg (Figure 1.3 (a)), the damping parameter of the contact force was used.

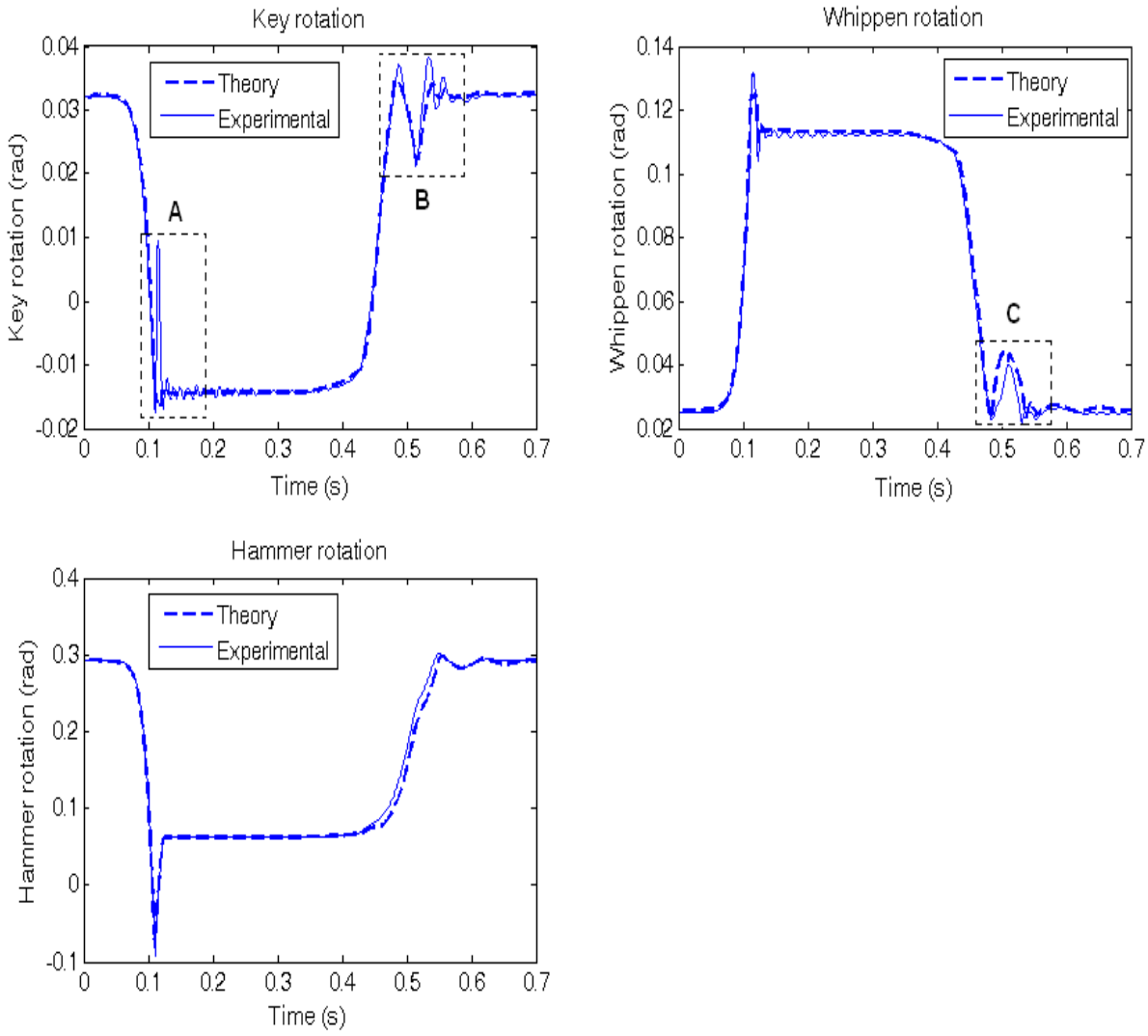

Figure 4.11: Experimental vs. Theoretical Results for the Prismatic-Revolute Joint Model for the Connection of the Piano Key to the Ground

To exclusively examine the effect of this new model for the connection of the key to the ground, the hammer shank was kept as a rigid body in the piano action model.

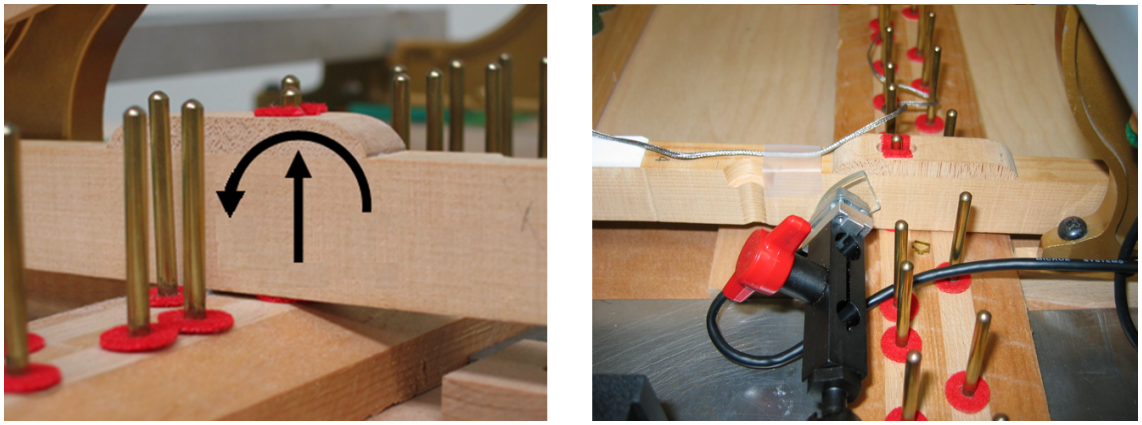

Figure 4.12: (a) Key Lift-off (b) The Scale Attached to the Key and the Corresponding Encoder

Since the contact surfaces in contact 12 (contact between the hammer head and the piano string in Figure 3.5) and in contact between the massless body and the ground are very similar, the three parameters for the stiffness of the contact for the contact between the massless body and the ground were opted to be the same as those for the contact 12 (Table 3.1). The location of the contact point on the ground was selected so that the piano key was at the same height at the rest position as it was when a revolute joint was used for modelling the connection of the key to ground. The damping parameter of the contact was tuned so that when the key falls back on the balance rail the bouncing motion of the key is damped out quick enough. After tuning these parameters, it turned out that to satisfy the static position of the hammer shank, according to the *regulation process* (outlined in Section 3.6), it is also necessary to adjust the location of the contact point on the hammer for the contact between the hammer and back check.

Figure 4.10 displays the computed key lift-off and the rotation of the key. It is evident that when the front of the key reaches the ground (part A in diagrams) and back of the key falls down on the ground (part B in diagrams), the key lifts off the balance rail.

Figure 4.11 displays the model results versus experimental results for the finger force profile in Figure 2.11. It should be noted that the discrepancies between the model and experimental results specified in boxes A and B for the rotation of the key in Figure 4.11

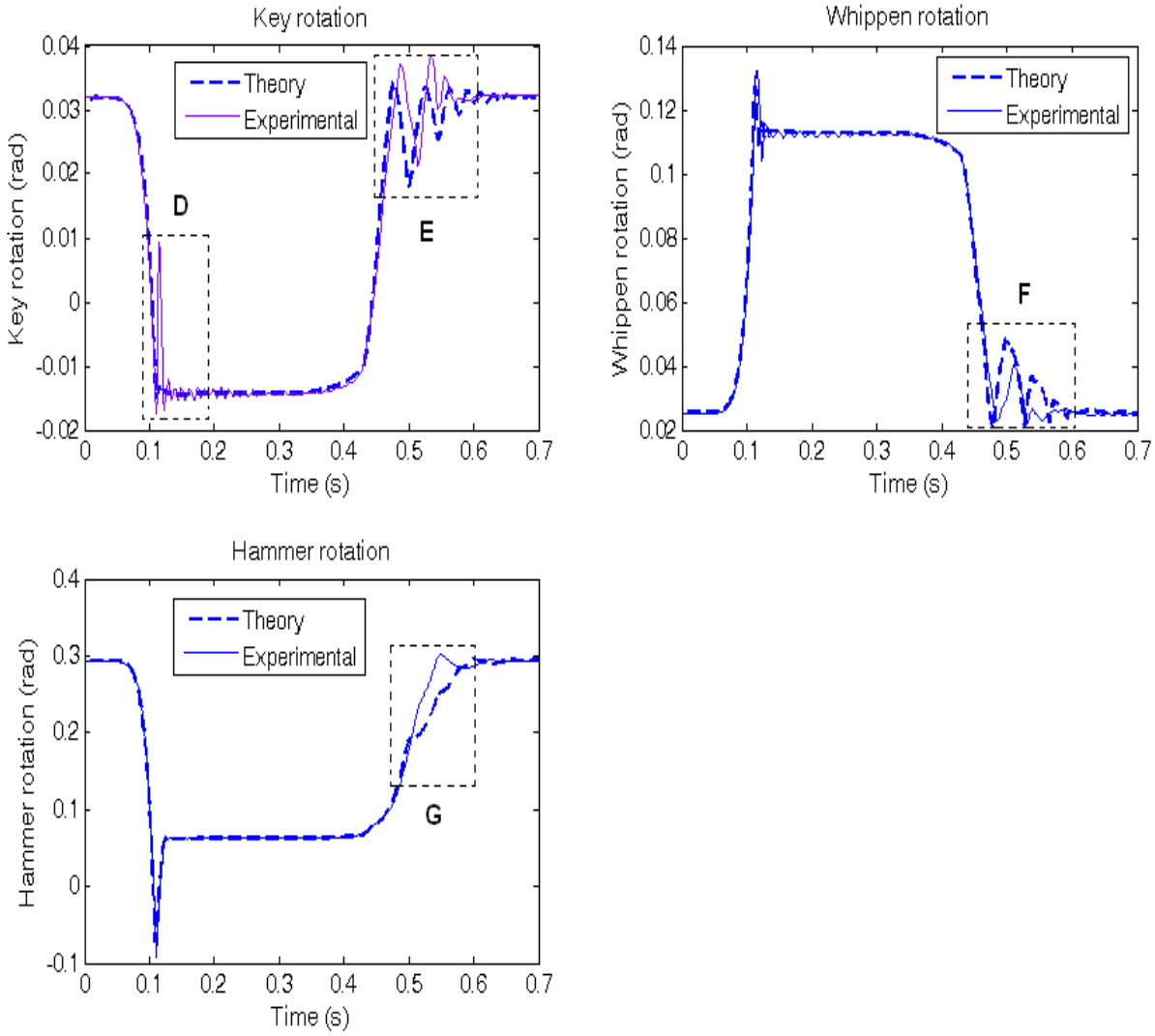

Figure 4.13: Experimental vs. Theoretical Results for the Revolute Joint Model for the Connection of the Piano Key to the Ground [1]

are due to the erroneous reading of the encoder that measures the rotation of the key. At these moments, the key is bouncing on the balance rail (Figure 4.12 (a)), and therefore the centre of the circular scale attached to the key changes (Figure 4.12 (b)). This causes the encoder not to measure the correct rotation of the key, while it is bouncing on the balance

rail[5]. The discrepancy between the model and experimental results specified in box C is merely due to the model inaccuracy.

By comparing Figure 4.11 with Figure 4.13 that shows the model results for the *forte* blow[6], in case the key is connected to the ground with a revolute joint (i.e., previous model in [1]), it is evident that the new proposed model noticeably increases the fidelity of the model, especially when the key falls back on the ground.

4.3 Fingertip

By using the final values of the parameters from Section 3.8, Pawluk's experimental data were reproduced with the proposed non-linear model and the results are shown in Figure 4.14. In this figure, the non-linear model predicts the experimental data very well. It should be mentioned that there are also other methods (for instance, a Neural Network) that can be used to find a function that maps experimental data. However, the elegance of this non-linear model is that it is very simple and has mechanistic components that directly represent the stiffness and damping of the fingertip pulp.

The proposed non-linear model successfully predicts the general behaviour of the fingertip pulp explained in [28]. It confirms that for an indentation profile with a constant velocity, when the velocity dips below a certain limit, the fingertip force stops decreasing and remains constant. Also, when the velocity goes beyond a certain limit, the fingertip no longer increases and remains constant. These threshold velocities (after which the fingertip force does not change) are illustrated in Figure 4.15. They are approximately 0.2 mm/s corresponding to 1.9 N (maximum force), and 80 mm/s corresponding to 5.3 N (maximum force), both for a 1.6 mm indentation. At these threshold velocities, there is a good match between the model results and experimental data, too.

[5]More details are available in [2].

[6]The discrepancies between the model and experimental results specified in boxes D and E for the rotation of the key in Figure 4.13 are due to the erroneous reading of the encoder that measures the rotation of the key. The discrepancies between the model and experimental results specified in boxes F and G are merely due to the previous model inaccuracy.

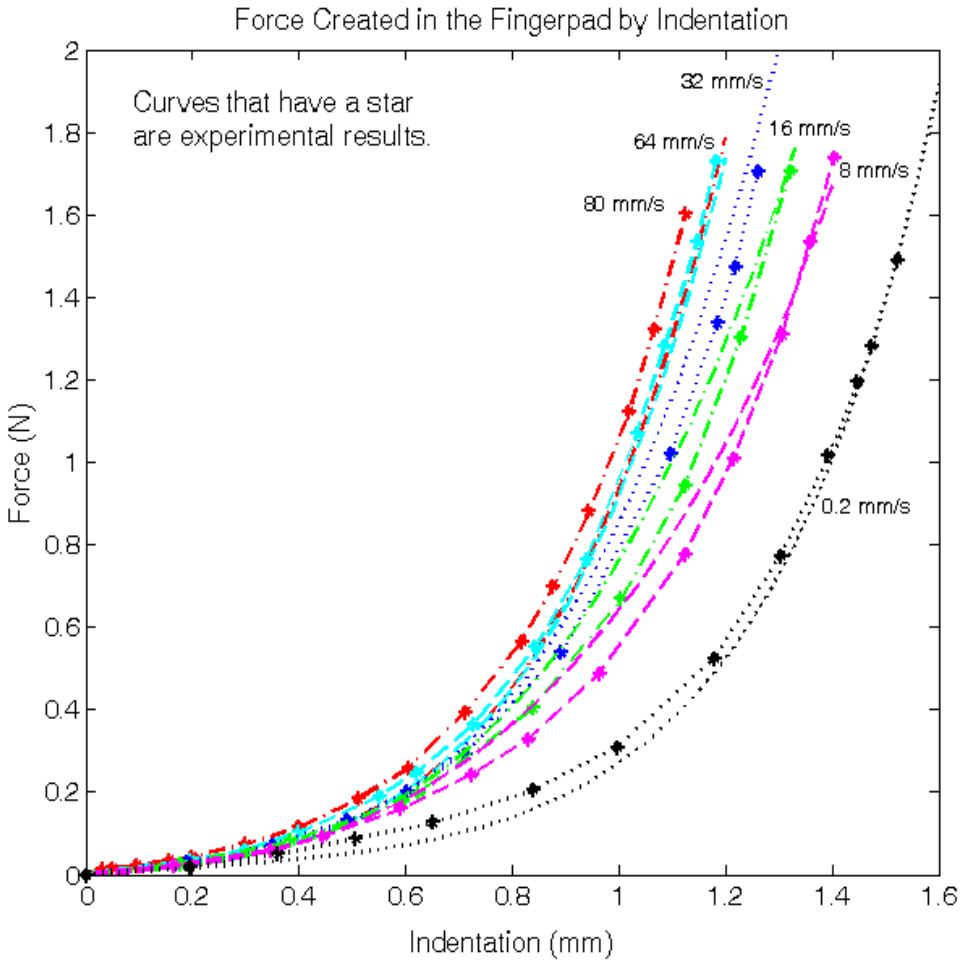

Figure 4.14: Proposed Model Results versus the Pawluk Experimental Results. The 12 Curves are Matched Two-by-Two, and each Pair is for a Certain Constant Velocity of Indentation

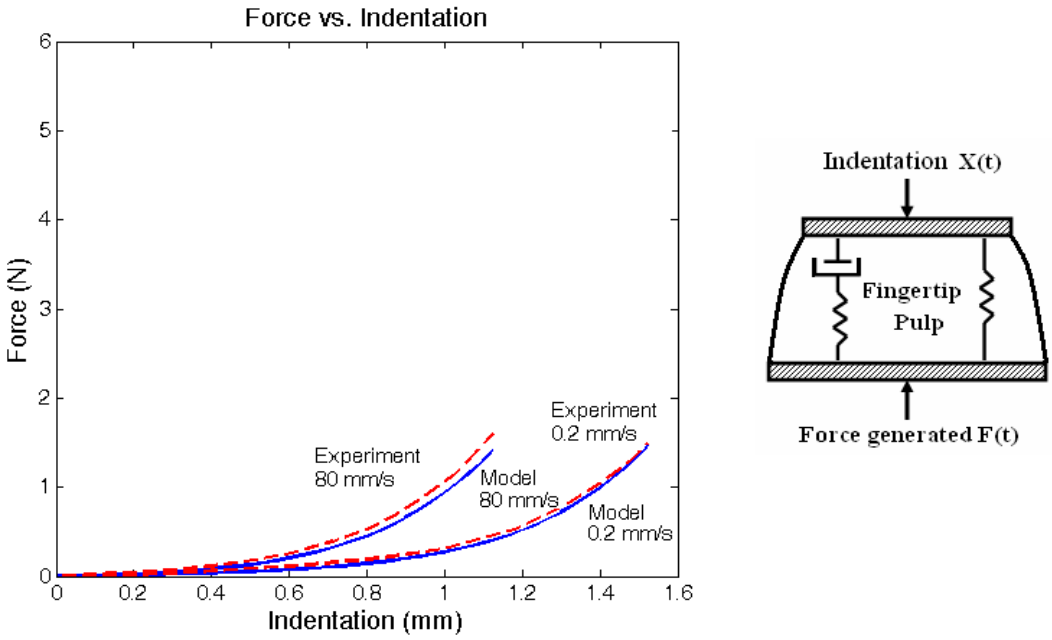

Figure 4.15: Model Force Response to two Extreme Cases: High-Velocity, and Low-Velocity Indentation Profiles, Compared with Experimental Data

Chapter 5

Conclusions and Future Research

5.1 Conclusions

The principal goal of this research was to increase the fidelity of an existing dynamic model of the piano action, developed at the University of Waterloo. Toward that end, the hammer shank, which had already been modelled with a rigid body in the previous model [2], was replaced with a flexible beam. The effect of the hammer shank flexibility in increasing the fidelity of the model, compared with experimental results for the rotation of the five piano parts, was investigated. It turned out that even in *forte* blow, the flexibility of the hammer shank did not significantly affect the rotation of the other parts of the piano mechanism, compared with the case that the hammer shank had been modelled as a rigid part. However, the flexibility of the hammer shank changed the impact velocity of the hammer head, and also caused a greater scuffing motion for the hammer head during the contact with the string.

To validate the theoretical results of the flexibility of the hammer shank, a strain gauge was mounted on top of the hammer shank. The pattern of the theoretical and experimental results was the same and, except for the static deflection of the hammer shank when it was caught at the back check, the theoretical and experimental results were in good agreement. It was concluded that the inaccuracy of the contact or friction model at the back check was the likely source of discrepancy between the results.

In the previous work [2], the connection of the key to the ground had been modelled

with a revolute joint. A new model, including a revolute joint, a prismatic joint, and a contact force at the bottom of the key, was proposed for this location. This new model allowed the key to lift off the balance rail, very similar to what happened experimentally. The damping and stiffness parameters of the contact force were tuned so that a better agreement between the theoretical and experimental results for the rotation of the action mechanism parts was obtained. It turned out that the new model for the connection of the key to the ground significantly increased the fidelity of the model for the *forte* blows.

By using a real-time PC, a new method for controlling the output torque of the motor was implemented, and a slightly better open-loop performance than the previous work [32] was obtained. With this method, the actual torque output of the motor was quite close to the desired torque output of the motor and there was only 8 ms lag between them.

5.2 Future Research

Although the contact model used in the action mechanism model predicts the contact forces for the forte blows, very well, it does not predict the contact forces for the piano blows with the same accuracy [1]. Contrary, in this contact model, the contact force depends upon the speed of the contacting bodies, even though the contact experiments demonstrate that the contact force for felt is not dependent on the contact speed [33]. This limitation of the original piano action model developed by Hirschkorn et al. [1] has not yet been addressed. In the future, other felt contact models can be investigated, along with other methods of modelling hysteretic behaviour, such as the Preisach Model [35].

The actual contact between the piano string and the hammer head is much more compliant than the current model (contact between the hammer head and the rigid bar). Therefore, adding a more realistic model of the piano string to the current piano action model is another interesting issue that can be done in the future. Depending upon the complexity of the model that is going to be considered for the piano string, the computational cost of the model increases; however, it might disclose some other interesting factors about the dynamic characteristics of the model. The duration of the contact between the hammer head and the piano string, the penetration of the hammer head in the piano string, the sound generated, and scuffing motion of the hammer head while it is in contact with

the piano string, are a few examples.

The available biomechanical model of the fingertip predicts the mechanical characteristics of the fingertip in the low contact force range of 0-2 Newtons and velocity range of 0.2-80 mm/s. To incorporate this model into the present piano model, however, the parameters of this model need to be tuned, according to the experimental data obtained from a pianist fingertip, in an appropriate contact force and velocity range. For the *piano* and *forte* blows the contact force range of 0-5 and 0-30 Newtons and velocity range of 0-250 and 0-675 mm/s are common, respectively. Furthermore, since this model only predicts the contact force in the fingertip in the loading phase, another model should be developed to predict the contact force in the unloading phase.

Finally, to address the discrepancy between the theoretical and experimental strains on top of the hammer shank, the accuracy of the contact and friction models at the back check location of the hammer shank can be investigated.

References

[1] M. Hirschkorn, J. McPhee, and S. Birkett, "Dynamic Modelling and Experimental Testing of a Piano Action Mechanism ", *ASME Journal for Computational and Nonlinear Dynamics*, vol.1, pp. 47-55, 2006.

[2] M. Hirschkorn, "Dynamic Model of a Piano Action Mechanism ", *Master's Thesis, University of Waterloo*, 2004.

[3] A. Askenfelt and E. Jansson, "From Touch to String Vibrations. II: The Motion of the Key and Hammer ", *Journal of Acoustical Society of America*, vol.90, pp. 2383-2393, 1991.

[4] P. Shi, J. McPhee, and G. Heppler, "A Deformation Field for Euler-Bernoulli Beams with Application to Flexible Multibody Dynamics ", *Multibody System Dynamics*, vol.5, pp. 79-104, 2001.

[5] P. Shi, J. McPhee, and G. Heppler, "Polynomial Shape Functions and Numerical Methods for Flexible Multibody Dynamics ", *Mechanics of Structures and Machines*, vol.29, no.1, pp. 43-64, 2000.

[6] A. Izadbakhsh, J. McPhee, and S. Birkett, "Dynamic Modelling of a Piano Action Mechanism with a Flexible Hammer Shank ", *Canadian Society of Mechanical Engineers (CSME) Forum*, 2006.

[7] Steinway and Sons, *Steinway and Sons Technical Reference Guide*, 1992.

[8] K. Hunt and F. Crossley, "Coefficient of Restitution Interpreted as Damping in Vibroimpact ", *ASME Journal of Applied Mechanics*, vol.42, pp. 440-445, 1975.

[9] Wood Handbook -Wood as an Engineering Material, *U.S. Department of Agriculture*, Online version available at: http://www.fpl.fs.fed.us/documnts/fplgtr/fplgtr113/.

[10] DynaFlexPro User's Manual, *MotionPro Inc.*, Waterloo, Ontario, Canada, 2006.

[11] Maple 10 User Manual, *Maplesoft*, Waterloo, Ontario, Canada, 2005.

[12] P. Shi, "Flexible Multibody Dynamics: A New Approach Using Virtual Work and Graph Theory ", *Ph.D. Thesis, University of Waterloo*, 1998.

[13] S. Bilbao, "Wave and Scattering Methods for the Numerical Integration of Partial Differential Equations ", *Ph.D. Thesis, Stanford University*, 2001.

[14] R. E. Valembois, P. Fisette, and J. C. Samin, "Comparison of Various Techniques for Modelling Flexible Beams in Multibody Dynamics ", *Nonlinear Dynamics*, vol. 12, no. 4, pp. 367-397, 1997.

[15] W. Pfeiffer, "The Piano Key and Whippen ", *Verlag Das Musikinstrument*, 1967.

[16] P. A. Matveev and A. M. Rymskij-Korsakov, *Sbornik*, 1937.

[17] A. Oledzki, "Dynamics of piano mechanisms ", *Mechanism and Machine Theory*, vol. 7, pp. 373-385, 1972.

[18] T. N. Topper and B. L. Wills, "The computer simulation of piano mechanisms ", *International Journal of Modelling and Simulation*, vol. 7, pp.135-139, 1987.

[19] B. Gillespie, "Dynamic modeling of the grand piano action ", *In proceedings of the International Computer Music Conference*, pp. 77-80, 1992.

[20] B. Gillespie, "Haptic Display of Systems with Changing Kinematic Constraints: The Virtual Piano Action ", *Ph.D. Thesis, Stanford University*, 1996.

[21] G. Van den Berghe, B. De Moor, and W. Minten, "Modeling a grand piano key action", *Computer Music Journal*, vol. 19, pp. 15-22, 1995.

[22] E. Hayashi, M. Yamane, and H. Mori, "Behavior of Piano-Action in a Grand Piano. I. Analysis of the Motion of the Hammer Prior to String Contact ", *Journal of the Acoustical Society of America*, vol. 105, n. 6, pp. 3534-3544, 1999.

[23] E. Serina, C. Mote, and D. Rempel, "Force Response of the Fingertip Pulp to Repeated Compression: Effects of Loading Rate, Loading Angle, Anthropometry ", *Journal of Biomechanics*, vol. 30, pp. 1035-1040, 1997.

[24] E. Serina, E. Mockensturm, C. Mote, and D. Rempel, "A Structural Model of the Forced Compression of the Fingertip Pulp ", *Journal of Biomechanics*, vol. 31, pp. 639-646, 1998.

[25] D. Jindrich, Y. Zhou, T. Becker, and J. Dennerlein, "Non-Linear Viscoelastic Models Predict Fingertip Pulp Force-Displacement Characteristics during Voluntary Tapping", *Journal of Biomechanics*, vol. 36, pp. 497-503, 2003.

[26] D. Pawluk, "A Viscoelastic Model of the Human Fingerpad and a Holistic Model of Human Touch ", *Ph.D. Thesis, Harvard University*, 1997.

[27] D. Pawluk and R. Howe, "Dynamic Contact of the Human Fingerpad against a Flat Surface ", *Journal of Biomechanical Engineering*, vol. 121, pp. 605-611, 1999.

[28] D. Pawluk and R. Howe, "Dynamic Lumped Element Response of the Human Fingerpad ", *Journal of Biomechanical Engineering*, Transactions of the ASME, Vol. 121, pp. 178-183, 1999.

[29] J. Wu, R. Dong, W. Smutz, and A. Schopper, "Modeling of Time-Dependent Force Response of Fingertip to Dynamic Loading ", *Journal of Biomechanics*, vol. 36, pp. 383-392, 2003.

[30] J. Wu, R. Dong, S. Rakheja, and A. Schopper, "Simulation of Mechanical Responses of Fingertip to Dynamic Loading ", *Medical Engineering Physics*, vol. 24, pp. 253-264, 2002.

[31] Y. Fung, "Biomechanics: Mechanical Properties of Living Tissue ", *Springer-Verlag*, New York, 1981.

[32] M. Hirschkorn, "Equipment Documentation ", *Technical Report*, University of Waterloo, 2004.

[33] W. Stamm, "Compressional behaviour of felts ", *Master's Thesis, University of Karlsruhe*, 2004.

[34] S. Cull and R. Tucker, "On the modelling of coulomb friction ", *Journal of Physics A: Mathematical and General*, vol. 32, pp. 21032113, 1999.

[35] M. Frankowicz and M. Chrenowski, "Application of Preisach model to adsorption-desorption hysteresis ", *Physica B: Condensed Matter*, vol. 372, issues 1-2, pp. 219-221, 2006.

[36] J. Gross and J. Yellen, "Graph Theory and its Applications ", *CRC Press*, New York, 1999.

[37] S. Han and H. Benaroya, "Nonlinear and Stochastic Dynamics of Compliant Offshore Structures ", *Springer*, Boston, 2002.

Appendix A

Model Parameters

All of the parameters that have been used in the action model are listed in the following sections. Figure A.1 shows all of the key points of the action components that in order to model the piano action, must be considered. It shows all joints, centres of mass, contact points, and coordinate systems for the piano action components as well as the ground[1].

A.1 Mass Properties

Table A.1 lists the masses, mass moments of inertia, and locations of the centres of mass (as defined in Figure A.1) for the components of the piano action.

The mass of each body was measured by using a lab scale. To locate the centres of the mass, the bodies were suspended by a thread from two different points. Then a vertical line was drawn under the fulcrum, and the location of the intersection was measured for each body. The measured intersections were reported as the centres of the mass.

To determine the mass moments of inertia, the bodies were suspended from a string and swung like a pendulum. The mass moments of inertia about the pivot point I_p, were then determined from the following expression for the period of a pendulum:

[1]The major portion of the material presented in the Appendix A is directly taken from [2] with minor changes. In Figure A.1 the massless body, and in Table A.11 the contact 14 have been added, respectively. In Table A.1, the hammer base, hammer shank, and hammer head are added and the previous hammer (total body) is removed. Tables A.4, A.8, A.9, A.10, and Section A.4 are new.

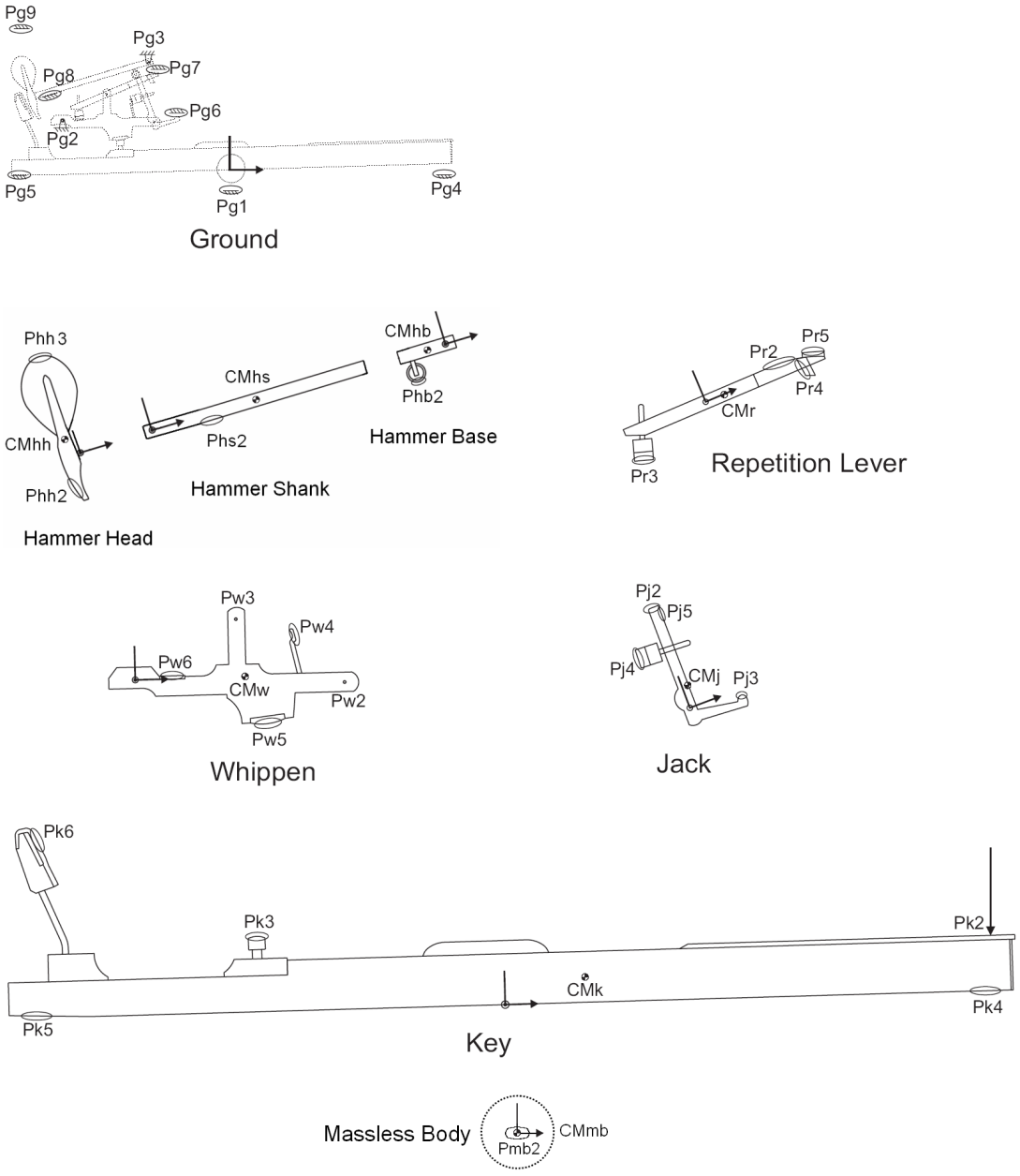

Figure A.1: Defined Points on the Action Components

Component	Mass (kg)	Mass Moment of Inertia (kg·m^2)	Centre of Mass (m) x	y
Key	0.12008	2.75E-03	0.0514	0.0158
Whippen	0.01196	1.69E-05	0.0502	-0.0018
Jack	0.00265	7.78E-07	0.0008	0.0195
Repetition	0.00371	4.10E-06	0.0021	-0.0012
Hammer Base	0.00226	0.251e-6	-0.0180	-0.0033
Hammer Shank	0.00156	9.615e-7	0.0430	0
Hammer Head	0.00792	2.253e-6	-0.0045	0.0223

Table A.1: Inertia Properties of the Action Components

$$I_p = mgl\left(\frac{T}{2\pi}\right)^2 \tag{A.1}$$

where m is the mass of the body, g is the gravitational constant, l is the distance from the pivot point to the centre of the mass of the body, and T is the period of oscillation. The moments of inertia about the centre of mass, I_{cm}, were then calculated by the parallel axis theorem:

$$I_{cm} = I_p - ml^2 \tag{A.2}$$

The three parts of the hammer, as depicted in Figure A.1, were not separable. Hence, determining the mass, mass moments of inertia, and locations of the centres of mass for them, accomplished a bit differently. Once the mass, mass moment of inertia, and centre of the mass of the hammer were determined experimentally by knowing the density of the wood and the geometry of the hammer, the SolidWorks software was used for determining the mass, mass moment of inertia, and centre of mass of the hammer base, hammer shank, and hammer head.

A.2 Geometric Properties

With a flatbed scanner all the bodies were scanned, and the images were scaled to match the known dimensions. Then, the images were imported into *AutoCAD* where the bodies were

traced and the dimensions measured. The ground dimensions were determined the same way, though the initial image was obtained using a digital camera, since the experimental apparatus could not be placed on a flatbed scanner.

Tables A.2, A.3, A.4, A.5, A.6, A.7, A.8, A.9, and A.10 list the coordinates of the key points and describe the contact surfaces for the fixed locations and all of the components of the action. All the coordinates are expressed in the frame shown on each body in Figure A.1.

All of the contact surfaces in the model are one of three possible two-dimensional geometries:

Circle A simple circular surface defined by the centre of the circle and radius.

Line A line defined by a point on the line and a unit normal vector.

Hybrid A shape consisting of an arc segment and two lines extending infinitely from the tangents of the arc. This is described by the centre and radius of the arc, and the starting and ending angles of the arc, as measured counter-clockwise from the positive x-axis.

		Position (m)		Unit Vector		Radius
Point	Description	x	y	x	y	(m)
Pg1	Pin Location	0.0000	-0.0048			
Pg2	Pin Location	-0.1810	0.0528			
Pg3	Pin Location	-0.0883	0.1166			
Pg4	Circle Contact	0.2172	-0.0074			0.0050
Pg5	Circle Contact	-0.2037	-0.0112			0.0050
Pg6	Line Contact	-0.0580	0.0663	0.000	-1.000	
Pg7	Circle Contact	-0.0843	0.1149			0.0033
Pg8	Circle Contact	-0.1921	0.0766			0.0050
Pg9	Line Contact	-0.2196	0.1716	0.000	-1.000	

Table A.2: Geometric Properties of the Ground

Point	Description	Position (m) x	y	Unit Vector x	y	Radius (m)
Pk2	Pin Location	0.2278	0.0261			
Pk3	Circle Contact	-0.1176	0.0263			0.0097
Pk4	Line Contact	0.2175	0.0000	0.000	-1.000	
Pk5	Line Contact	-0.2208	0.0010	-0.041	-0.999	
Pk6	Line Contact	-0.2187	0.0817	0.904	0.427	

Table A.3: Geometric Properties of the Key

Point	Description	Position (m) x	y	Radius (m)
Pmb2	Circle Contact and Pin Location	0.000	0.000	0.005

Table A.4: Geometric Properties of the Massless Body

Point	Description	Position (m) x	y	Unit Vector x	y	Radius (m)
Pw2	Pin Location	0.0989	-0.0035			
Pw3	Pin Location	0.0483	0.0275			
Pw4	Line Contact	0.0759	0.0189	0.969	0.247	
Pw5	Circle Contact	0.0595	0.0030			0.0253
Pw6	Line Contact	0.0170	0.0015	0.000	1.000	

Table A.5: Geometric Properties of the Whippen

Point	Description	Position (m) x	y	Unit Vector x	y	Radius (m)	Arc (rad)
Pj2	Hybrid Contact	-0.0010	0.0495			0.0010	1.571 - 3.142
Pj3	Circle Contact	0.0247	-0.0050			0.0021	
Pj4	Circle Contact	-0.0093	0.0300			0.0050	
Pj5	Line Contact	0.0031	0.0477	1.000	0.000		

Table A.6: Geometric Properties of the Jack

Point	Description	Position (m) x	Position (m) y	Unit Vector x	Unit Vector y	Radius (m)	Arc (rad)
Pr2	Hybrid Contact	0.0363	-0.0521			0.0552	1.300 - 1.571
Pr3	Circle Contact	-0.0351	-0.0089			0.0050	
Pr4	Circle Contact	0.0527	-0.0009			0.0050	
Pr5	Line Contact	0.0561	0.0017	0.317	0.948		

Table A.7: Geometric Properties of the Repetition Lever

Point	Description	Position (m) x	Position (m) y	Radius (m)
Phb2	Circle Contact	-0.0170	-0.0091	0.0044

Table A.8: Geometric Properties of the Hammer Base

Point	Description	Position (m) x	Position (m) y	Unit Vector x	Unit Vector y
Phs2	Line Contact	0.0180	-0.0031	0.000	-1.000

Table A.9: Geometric Properties of the Hammer Shank

Point	Description	Position (m) x	Position (m) y	Radius (m)
Phh2	Circle Contact	0.0467	-0.0025	0.0549
Phh3	Circle Contact	-0.0041	0.0356	0.0102

Table A.10: Geometric Properties of the Hammer Head

A.3 Contact Properties

The contact parameters for all 14 contact locations are listed in Table A.11.

Contact #	Points		Curve Parameters			Damping Factor	Friction Parameters		
			a	b	c		A	B_1	B_2
1	Pk3	Pw5	1.26E+10	3.26E+07	7.92E+03	1.877	0.167	0	1
2	Pk4	Pg4	4.41E+10	-1.02E+07	1.57E+04	1.219	0	0	0
3	Pk5	Pg5	2.42E+10	-1.11E+07	6.54E+03	2.502	0	0	0
4	Pk6	Phh2	5.86E+11	-3.70E+07	3.11E+04	2.446	0.434	1.78	1
5	Pw4	Pj4	5.28E+09	-7.54E+05	4.42E+03	5.781	0	0	0
6	Pw6	Pr3	2.53E+10	-9.89E+06	7.07E+03	7.732	0	0	0
7	Pj2	Phb2	3.92E+11	1.10E+07	3.23E+04	4.694	0.177	1.85	1
8	Pj3	Pg6	7.46E+10	-2.29E+07	1.32E+04	1.527	0	0	0
9	Pj5	Pr4	6.02E+10	-1.68E+07	6.96E+03	0.779	0	0	0
10	Pr2	Phb2	1.09E+12	-7.51E+07	2.23E+04	2.935	0.332	0.73	1
11	Pr5	Pg7	8.82E+11	-7.59E+07	1.67E+04	4.985	0	0	0
12	Phh3	Pg9	1.81E+10	8.19E+07	1.16E+04	0.800	0	0	0
13	Phs2	Pg8	8.58E+08	-1.11E+06	2.39E+03	8.964	0	0	0
14	Pg1	Pmb2	1.81E+10	8.19E+07	1.16E+04	100	0	0	0

Table A.11: Contact Properties

The *Curve Parameters* define the three polynomial terms of the fit curve of Equation (3.3). This curve and the *Damping Factor* are used in Equation (3.2).

The three *Friction Parameters*, which are derived from the static and kinetic coefficients of friction, are used in Equation (3.6). The coefficients of friction for each pair of contacting bodies were measured by holding the first body fixed, pushing the second body into the first with a known force, and then measuring the force required to initiate the bodies sliding, and keep them sliding.

A.4 Hammer Shank Properties

Table A.12 lists the parameters of the hammer shank that are used in its Rayleigh beam model.

Parameter	Value	Unit
E (Modulus of Elasticity)	10.18×10^{9}	Pa
ρ (Density)	560	kg/m^3
L (Length)	0.086	m
A (Area)	32.38×10^{-6}	m^2
J_{zz} (Second Moment of Area)	83.44×10^{-12}	m^4

Table A.12: Properties of the Hammer Shank

A.5 Other Properties

In addition to the mass, geometric, and contact properties already listed, the model incorporates rotational springs and friction in the revolute joints of the action bodies.

The spring force in the jack was measured to be approximately constant at 0.0042 N·m. The spring force in the repetition lever follows the standard linear spring model with values shown in Equation (A.3)

$$T = -0.073(\theta_r - 0.832) \tag{A.3}$$

where T is the torque acting on the revolute joint (in N·m), and θ_r is the angle between the repetition lever and the whippen (in radians).

The friction parameters for the revolute joints of the five bodies, as defined in Equation (3.8), are listed in Table A.13.

The rotational friction parameter E is derived directly from the kinetic frictional torque in the joint. This torque was determined by measuring the force required to rotate the joint at a known distance from the centre of the joint. Static friction, as described by F_1 and F_2, was not included in these joints.

Component	E	F_1	F_2
Key	0.0122	0	0
Whippen	0.000397	0	0
Jack	0.000397	0	0
Repetition	0.00247	0	0
Hammer	0.00101	0	0

Table A.13: Rotational Friction Parameters

Appendix B

Experimental Equipment

The following tables list the software and equipment used in the experimental piano action.

Vendor	Package	Version
Kollmorgen	ServoStar MotionLink	4.4.6
National Instruments	LabVIEW Express	7.1
Photron	Motion Tools	1.0.5

Table B.1: Software

Vendor	Part	Description
Kollmorgen	MT308A1	DC Brushless Servo Motor
Kollmorgen	CE03250	DC Brushless Servo Drive, 3 Amp
National Instruments	PCI-6229	Multifunction PCI IO Board

Table B.2: Actuation Equipment

Vendor	Part	Description
Sensotec	Model 13, 25 lb	Subminiature Strain Load Cell, 25 pound
INTERTECHNOLOGY	Type EA-06-062DN-350	Strain Gauge, 350 ohm Bridge
National Instruments	PCI-6034E	Multifunction PCI IO Board
National Instruments	SCXI-1520	SCXI Strain/Bridge Module

Table B.3: Force and Strain Measurement Equipment

Vendor	Part	Description
MicroE Systems	M1510S-40	Digital Encoder Sensor
MicroE Systems	R3213	Encoder Rotary Scale, 1.25 inch
MicroE Systems	R5725	Encoder Rotary Scale, 2.25 inch
National Instruments	PCI-6602	Counter/Time PCI Board

Table B.4: Position Measurement Equipment

Vendor	Part	Description
Photron	FASTCAM-X 1280 PCI	High Speed Video System, 1,280 x 1,024 pixel

Table B.5: High-Speed Video Equipment

Appendix C

Experimental Setup Wiring

For reading the strain gauge, the configuration shown in Figure C.1[1] was used.

The PC (II) in this figure runs on a real-time operating system and is dedicated for controlling the motor. The PCI-6229 Multifunction IO board, which is compatible with the NI real-time operating system, was used to send the motor demand signal. The fastest update rate at which the motor torque demand signal can be sent to the amplifier with this PC is 500 Hz. The programs run on this real-time platform are first developed on the PC (I), and then are passed to the real-time PC (II) through a cross-over cable for deterministic execution.

To send the motor torque demand signal from the PC (II) at a high speed, the PC (II) is not used for reading the load cell or strain gauge, too. The PC (III) is individually used for reading the load cell or strain gauge. On this PC, using the high-speed buffer feature of the PCI-6602 and PCI-6034E cards, it is possible to read the load cell (or strain gauge) with 2 kHz update rate. This high update rate allows capturing more data in a given span of time. This is an important issue in the case of strain gauge, since when the hammer strikes the piano string, high-frequency vibrations are created in the hammer shank and to capture them a high update rate is needed.

Since there is only one signal conditioning unit available in the experimental setup, it is not possible to capture the data from the load cell and strain gauge, simultaneously (two

[1]In this figure, a circular scale has been used to measure the rotation of the key. The vertical motion of the key is measured by a high-speed video camera, separately.

separate signal conditioning units are needed for that purpose). To work around this, first the signal conditioning unit is used to read the load cell and with a given input force profile to the motor, the response of the motor is measured by the load cell. To make sure the motor torque output is consistent, this process is repeated a few times; then, in the next step, the signal conditioning unit is used for reading the strain gauge. The motor is run with the same given force profile, and this time the strain gauge is read. Finally, once the experiment is completed, the duration and maximum point of the strain and motor output torque curves are used to synchronize the strain curve with the motor output force curve.

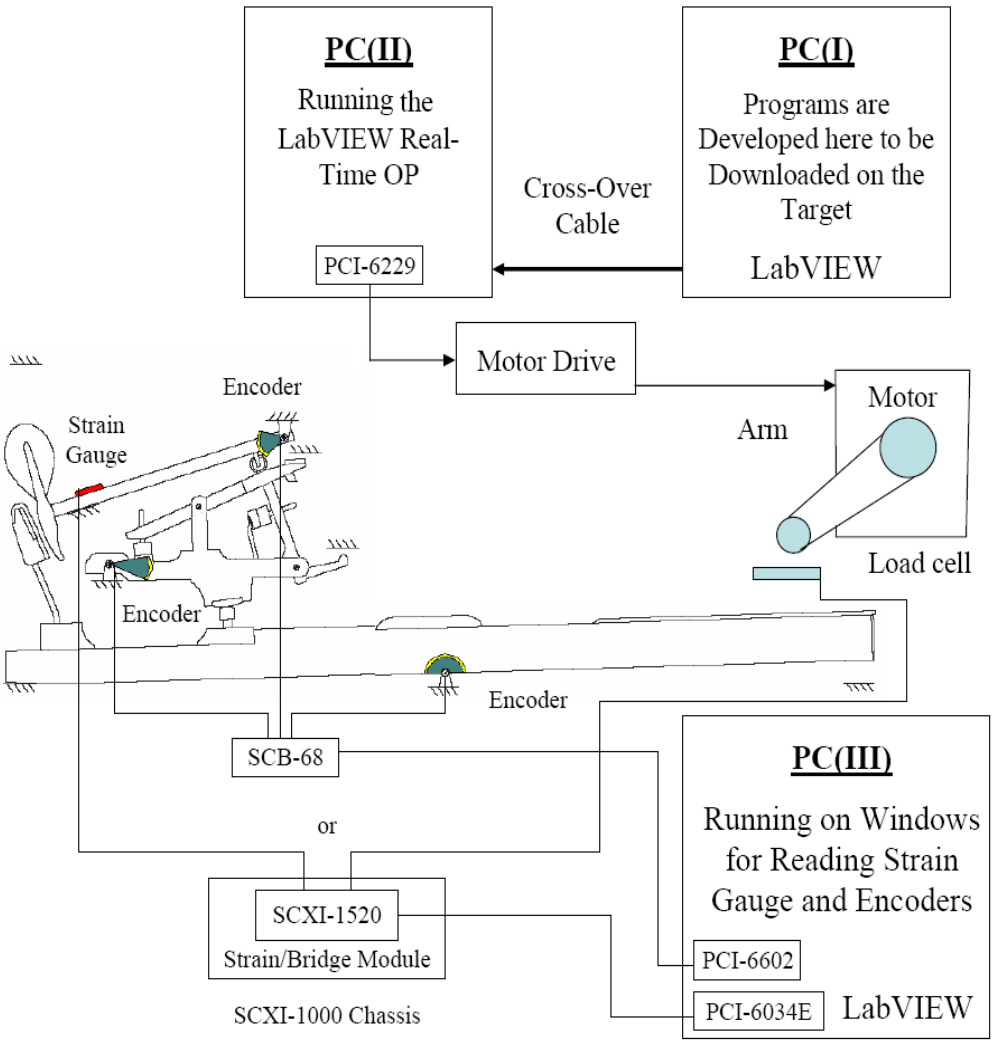

Figure C.1: The Wiring of the Experimental Setup used for Reading the Strain Gauge with 2 kHz Sampling Rate

Appendix D

Motor Torque Control

As it was mentioned in Section 2.8, to improve the performance of the open-loop torque control even further, the neural network technique and a few linear control methods were tried in this work. For this purpose, the CE03250 amplifier in Figure 2.2 b was used to run the motor, and the sub-miniature load cell in Figure 2.3 b was used as the feedback device. Before explaining the control methods that were tried, a few points should be mentioned:

1. The maximum of the non-linearity/hysteresis of the sub miniature load cell is $\pm 0.5\%$ of the full scale, and its maximum non-repeatability is $\pm 0.1\%$ of the full scale. Therefore, the maximum error in reading from the load cell is $\pm 0.6\%$ of the full scale (25 lb), which is 0.67 N. This imposes a limitation (0.67 N) to the amount of the maximum error reduction that can be obtained by any control method[1].

2. The fastest update rate at which the amplifier analog port can be written by using the real-time PC is 500 Hz, as explained in Section 2.5. The amplifier analog port is where the motor torque demand signal is sent. This means that the input force profile to the motor cannot contain any frequency faster that 500 Hz (the force profile cannot be sampled faster than 500 Hz).

3. The response of the motor to two different step inputs (with a 10 N magnitude) with the present amplifier is shown in Figure D.1. According to this figure, the motor takes approximately 25 ms to reach its final value, in response to the step function. Therefore,

[1]The research group has another load cell with the same brand. This load cell is capable of measuring the loads up to 1000 gr, and therefore it provides a higher precision of 0.059 N in reading a load.

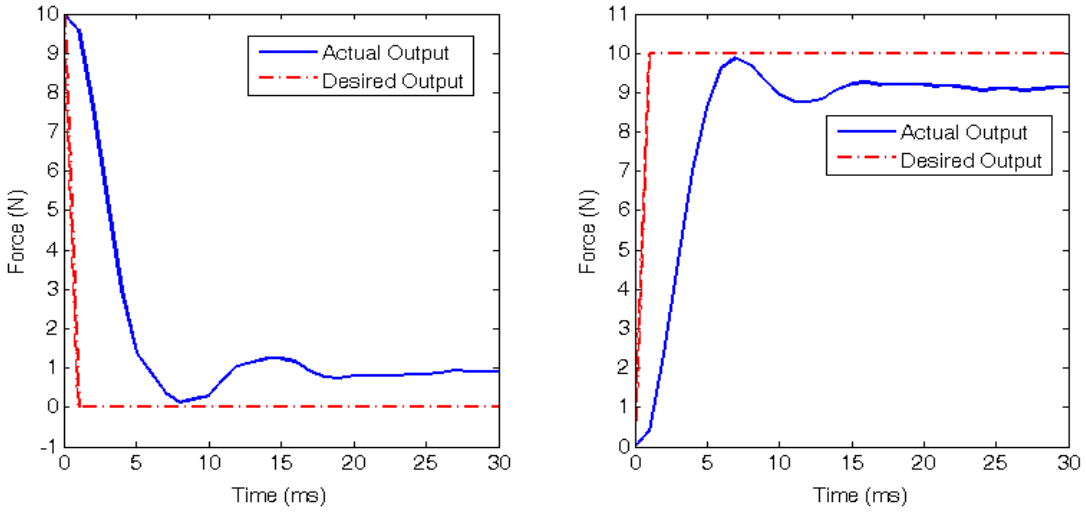

Figure D.1: Response of the Motor to Two Step Functions

assuming the system is linear, if a force curve with 2 ms sampling time is passed through the amplifier, then the motor always runs in its transient phase in each time interval of 2 ms (does not have enough time to reach its final force value in each 2 ms interval). However, by using some input/output data from the motor and analyzing them, it turns out that the motor does not behave quite linearly. Four step functions with different amplitudes are put through the amplifier, and then the response of the motor to them is measured.

Figure D.2 shows the step input curves and the corresponding motor response to each of them. Since the pattern of the system response changes for the step input functions with different magnitudes, it is concluded that the motor does not display a linear behaviour[2].

4. Figure D.3 reveals a typical measurement by the load cell before and after applying a 100 Hz low-pass filter. This 100 Hz low-pass hardware filter is embedded in the signal conditioning module. This filter is another source of inaccuracy in the system in the sense that it introduces a lag in the measurements, as shown in Figure D.3. Therefore, the 8 ms latency in the force curves in Figure 2.14 is not due to the motor inductance only. On the

[2]If the system is linear, then a linear transfer function like $G(s)$ exists for it. Therefore, with a step function with a magnitude of A as the input to the system, the system response will be $G(s)\ \frac{A}{S}$. It is obvious that for different values of A, the system response should keep its pattern and change linearly.

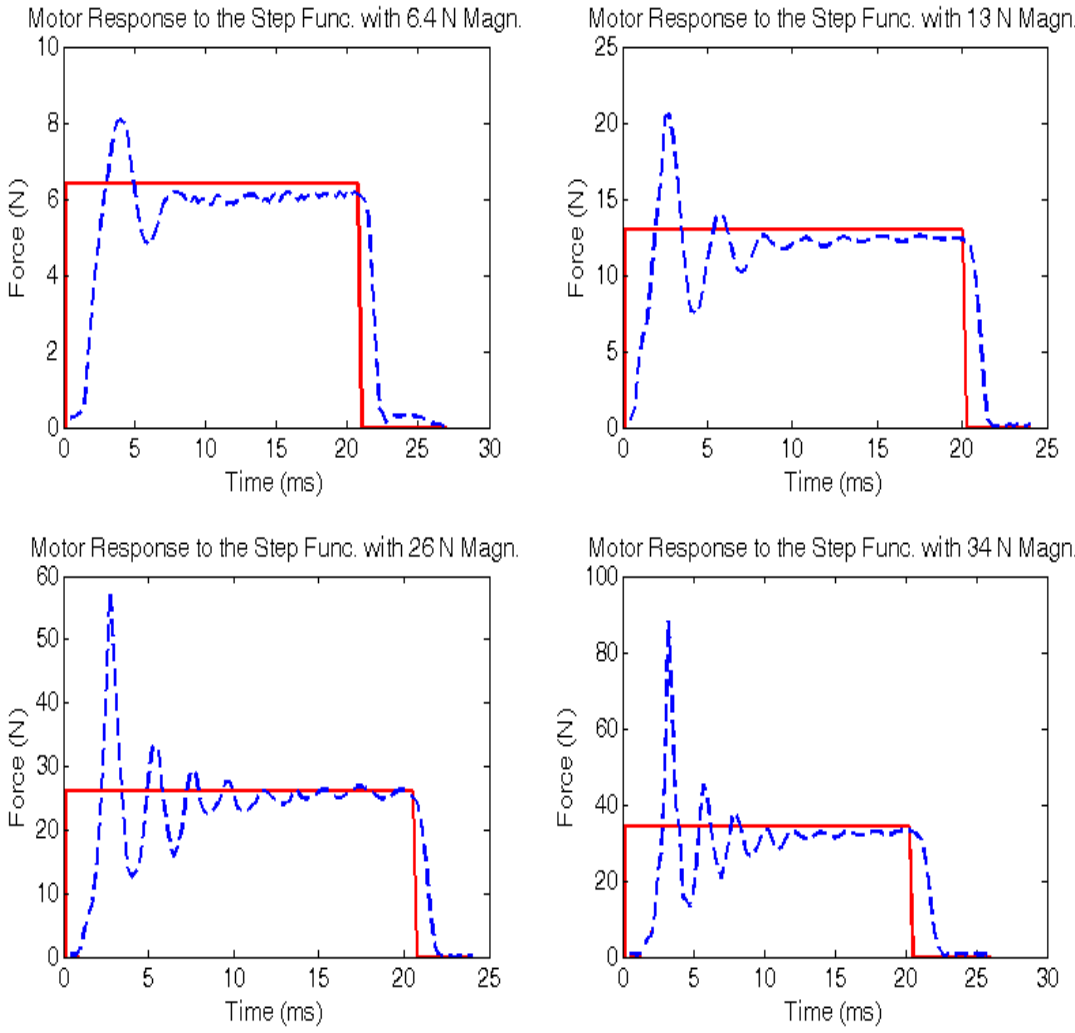

Figure D.2: Response of the Motor to Four Step Functions

other hand, as long as a load cell is used for measuring the force of the motor, the use of a low-pass filter cannot be ignored and therefore, this uncertainty always exists.

The following sections describe the control methods that are tried to improve the open-loop performance of the motor.

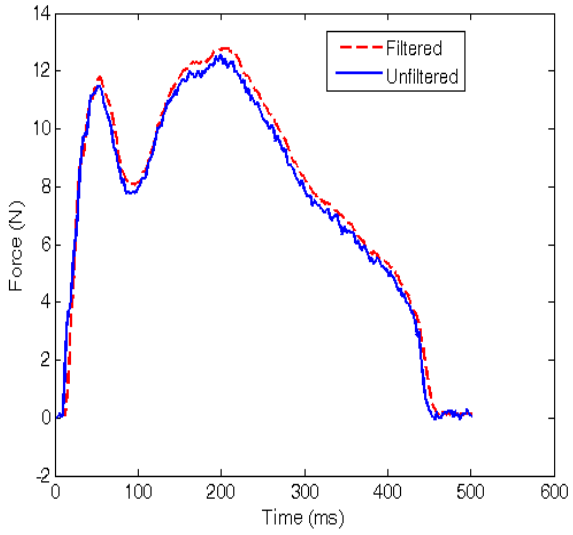

Figure D.3: Typical Measurements of the Load Cell before and after Filtering by a 100 Hz Low-Pass Filter

D.1 Neural Network

In order to increase the fidelity of the torque control, the neural network (NN) method was tried first. The approach here was to train an NN that took the actual force output of the motor as the NN's input and then set the desired force output as the NN's output. The idea is shown in Figure D.4. Ten different input and output normalized *forte* force profiles, each with approximately 600 points (5 of them are shown in Figure 2.14) and with just slightly different patterns, were used to train the NN. The real-time PC, in the configuration shown in Figure 2.8, was used to generate this data. One more input and output forte force profile, as shown in Figure 3.5, was used for validating the network output.

The NN was set up so that it had five inputs and one output. The inputs to the network were $Fout_i$, $Fout_{i-1}$, $Fout_{i-2}$, $Fout_{i-3}$, and $Fout_{av}$, and the output was Fin_i. This means that for any force input to the network, besides the current time step, the output of the network depends on the history of the force profile at the three time steps before and also the average of the force profile from the beginning of the force profile up to the current

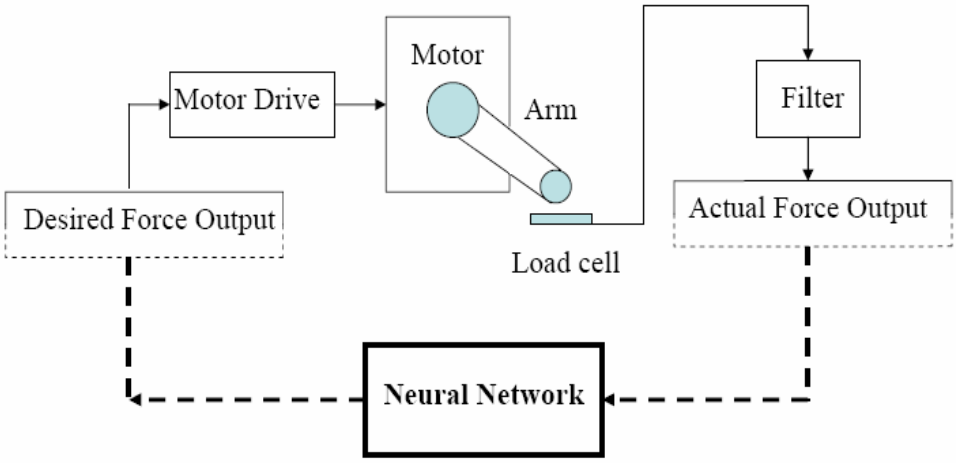

Figure D.4: Neural Network Input and Output

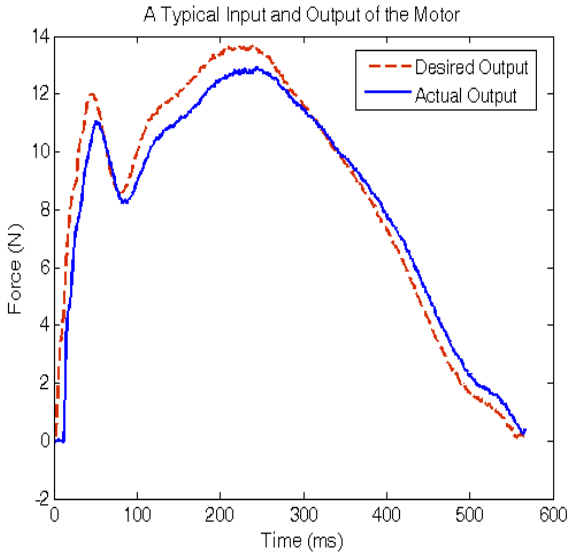

Figure D.5: Typical Desired and Actual Force Output of the Motor

time step. This is one of the most common NN forms, for such a problem.

Figure D.6 displays the performance of one of the best NNs obtained during the training process for predicting the desired force output in Figure D.5. The NN had one hidden layer

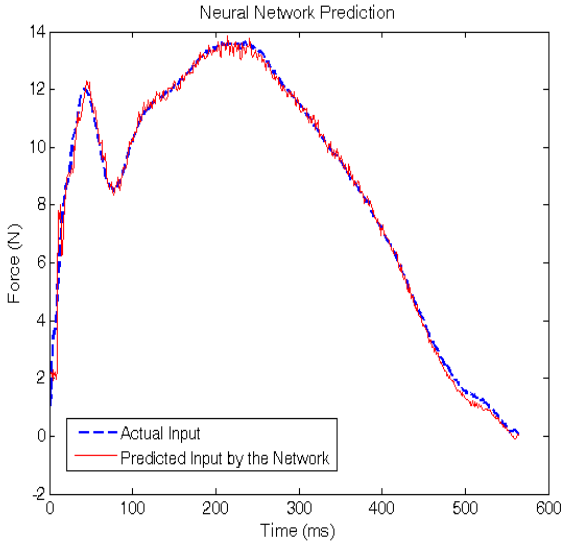

Figure D.6: Neural Network Prediction

with five neurons with the *Log Sigmoid*[3] transfer function, and the output layer had one neuron with the *Linear*[4] transfer function. Although the prediction of the NN was very close to the actual motor input, this method was not implemented, for the following reasons

- There is no guarantee that the NN method consistently gives a valid result for any forte force profile (cannot be proven).
- For this problem, an NN does not improve the performance of the open loop system, significantly.
- The output of the neural network is noisy and needs to be filtered by a low-pass filter before passing through the amplifier.
- Generally, an NN is good for the rough modelling of a system, but less appropriate for this *delicate control problem.*

[3]The equation of this transfer function is $f(x) = \frac{1}{(1+e^{-x})}$.
[4]The equation of this transfer function is $f(x) = x$.

D.2 Proportional-Integral-Derivative (PID) Controller

The PID controller works well for many applications, because it is based on the error between the actual and desired output and tries to minimize this error. The challenge in this method is finding good values for the K_p, K_i, and K_d parameters, and this, in turn, comes down to finding a good model of the system (motor + amplifier + load cell). Figure D.7 indicates how the PID controller can be used to run the motor.

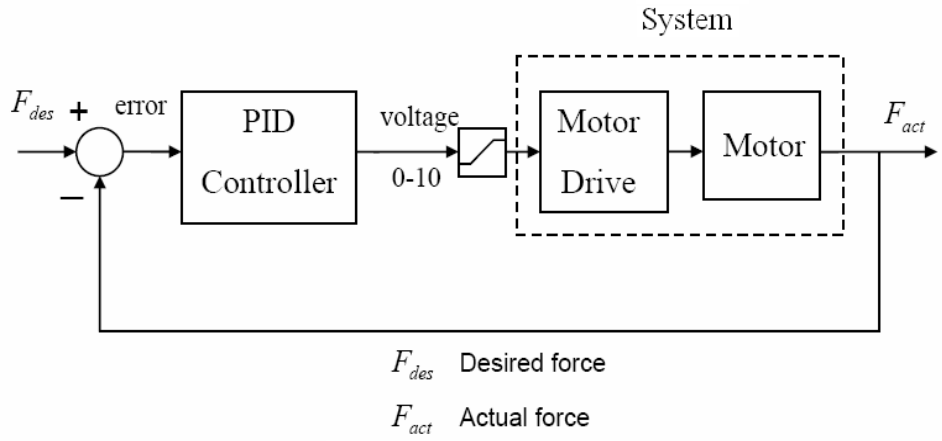

Figure D.7: Using the PID Controller to Run the Motor

The curves in Figure D.1 were used in the *MATLAB* system identification toolbox and with the *process models* method, a third order transfer function was found that matched those curves, quite closely[5].

$$G(s) = \frac{K}{(1 + 2\ Zeta\ T_w\ s + (T_w\ s)^2)(1 + Tp_3\ s)} \tag{D.1}$$

Three was the lowest order that matched the behaviour of the system very closely and

[5]The *process models* method results in a continuous-time model that is characterized by a static gain K, one or several time constants T, a possible zero T_z, a possible time delay (dead time) T_d, and a possible enforced integration.

also predicted the behaviour of the system in the curves of Figure 2.14 fairly closely. The values of the model parameters are as follows.

$$K = 0.9322 \text{ Newton}, \quad T_w = 1.5268, \quad Zeta = 0.3679, \text{ and } \quad Tp_3 = 2.3086$$

The curves in Figure D.8 show how well this linear model predicts the response of the actual system.

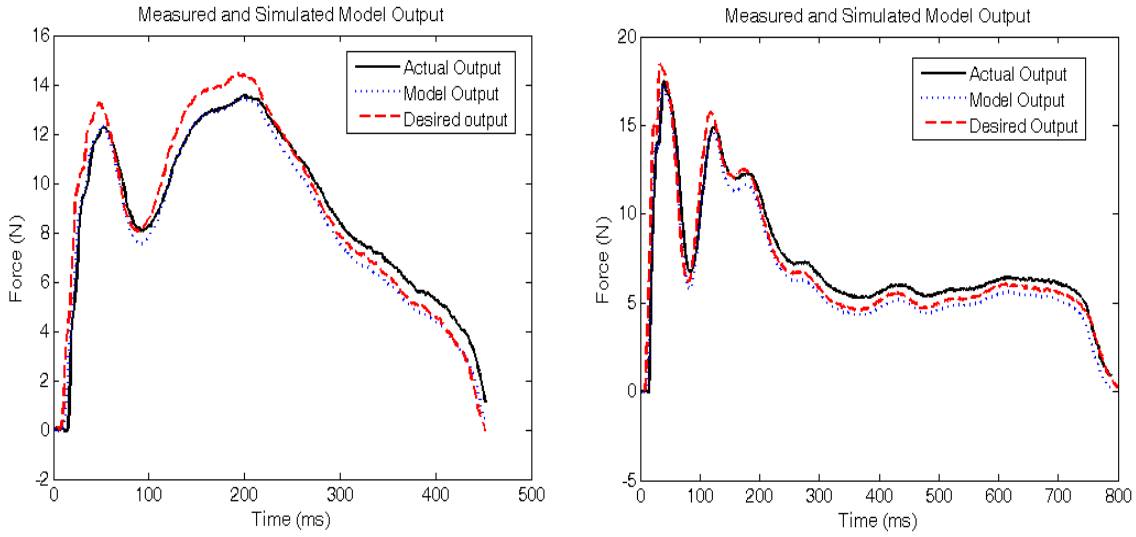

Figure D.8: Comparison between the Model and Actual Output

This model of the system (which does not perfectly match the behaviour of the system) was used in the *MATLAB* Simulink environment to find good values for the K_p, K_i, and K_d parameters. Many random combinations of values for K_p, K_i, and K_d parameters were tested but the rise time of the system for the step function input could not be reduced. Figure D.9 shows the model responses for the different values of K_p, K_i, and K_d parameters. The values of K_p, K_i, and K_d parameters in this figure, are the best that could be found by trial-and-error. As it is seen, the rise time of the system could not be reduced less than 1 ms.

On the other hand, by using the *gradient descent* optimization method in *MATLAB*, the values of K_p, K_i, and K_d parameters were varied to find the values that reduced the

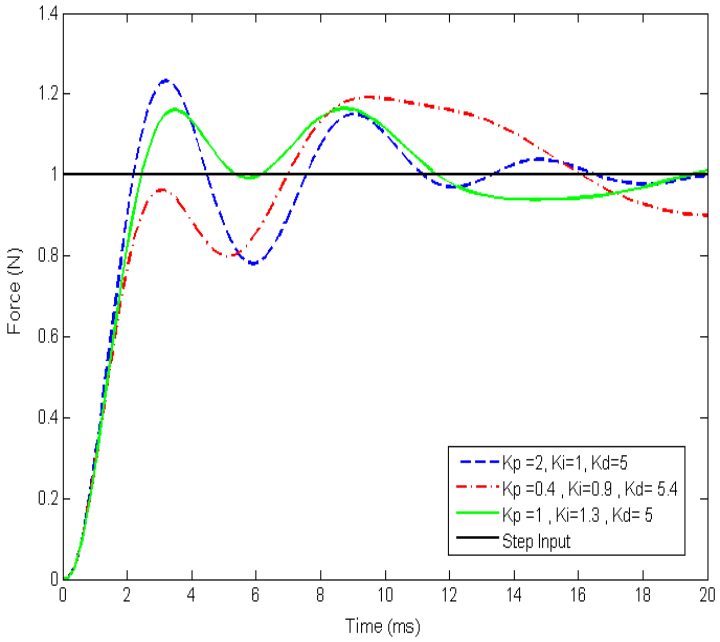

Figure D.9: Step Response of the Model for Different Values of K_p, K_i, and K_d

rise time of the system[6]. This was done by setting a few constraints on the step response of the model, as shown in red, in Figure D.10. The values used for the parameters of this optimization method are given in Table D.1.

Tolerance on the K_p, K_i, and K_d parameters	0.001
Tolerance on the constraints (shown in Figure D.10)	0.001
Maximum iterations	1000

Table D.1: Values of the Parameters used in the Gradient Descent Optimization Method

However, this method did not perform well, either. The results of this method are shown in Figure D.10.

[6] *Gradient descent* is an optimization algorithm that approaches a local minimum of a function by taking steps proportional to the negative of the gradient (or the approximate gradient) of the function at the current point.

In another attempt to find the system model, the $ARMAX$[7] method instead of the *process models* method in system identification toolbox in *MATLAB* was implemented. However, it turned out that this method does not result in a more accurate model for the system than that of the *process models* method.

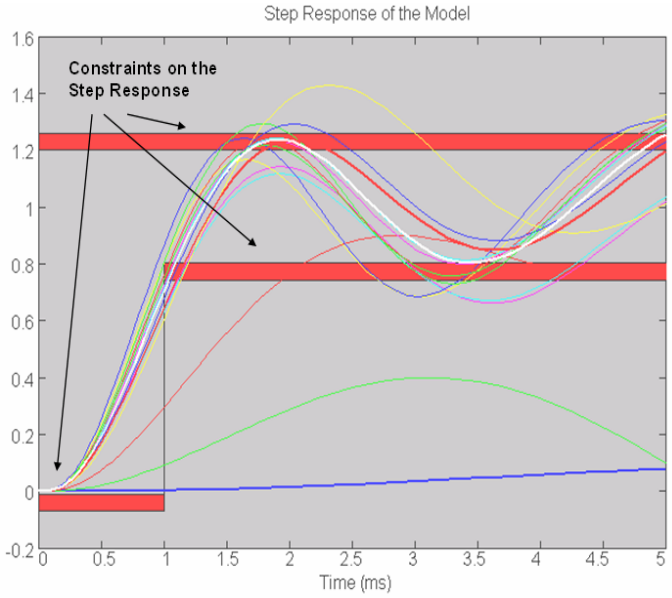

Figure D.10: Step Response of the Model for Different Values of K_p, K_i, and K_d Obtained by Implementing the *Gradient Descent* Optimization Method

Since the models of the system obtained from the $ARMAX$ and *process models* methods, cannot perfectly mimic the behaviour of an actual system, it could not be concluded that the PID controller cannot perform well for the actual system. Therefore, in the next step, another approach was considered to find a more accurate model for the system.

By taking a closer look at the curves in Figure 2.14, it is evident that in terms of latency, the response of the motor to an increasing demand torque (the derivative of the

[7]This method results in a discrete-time model in the form of $A(q)y(t) = B(q)u(t-nk)+C(q)e(t)$, where y is the system output, u is the system input, q is the delay operator, and e is the generalized error. The terms $A(q)y(t)$, $B(q)u(t-nk)$, and $C(q)e(t)$ are called autoregressive, exogenous, and moving average, respectively.

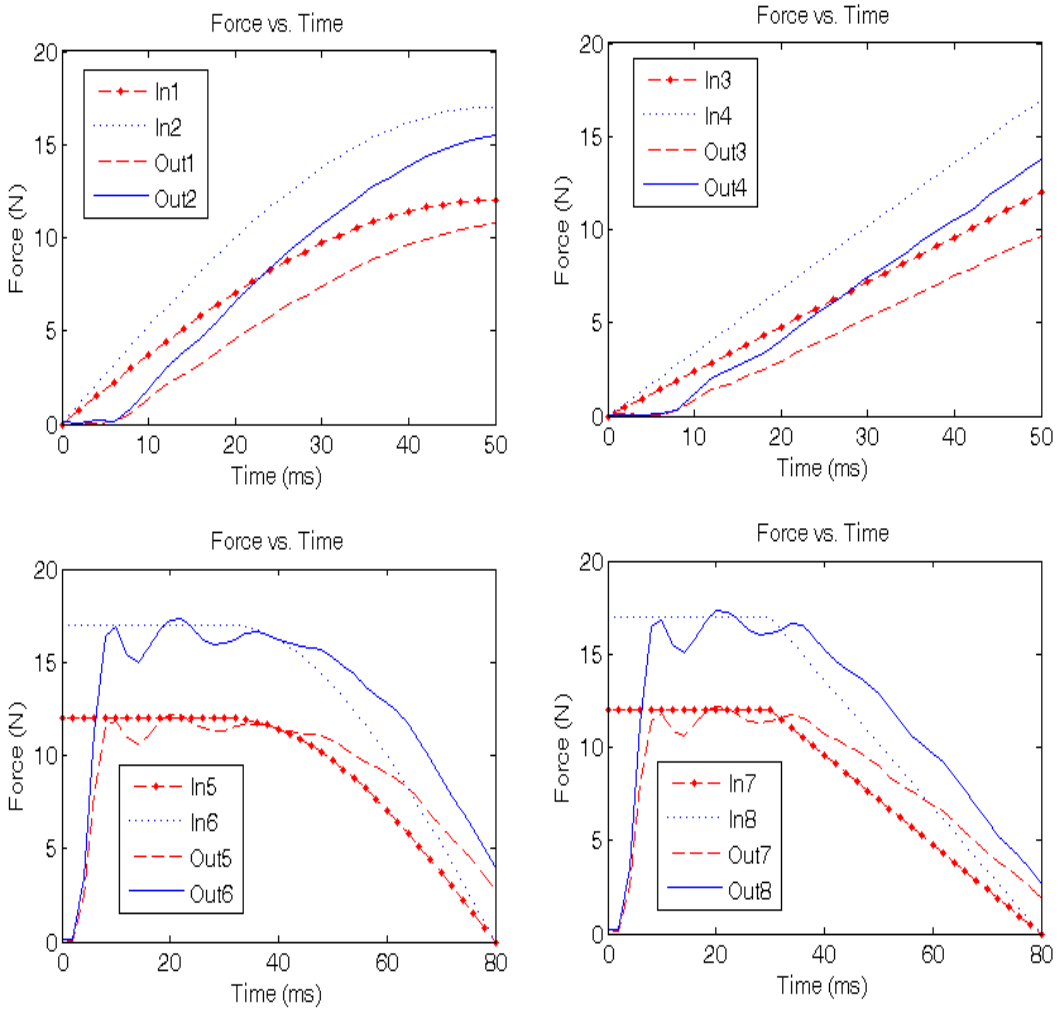

Figure D.11: Different Increasing and Decreasing Force Profiles used for Identifying the Motor Model

torque profile is positive) is different from the motor's response to a decreasing demand torque (the derivative of the torque profile is negative)[8].

Based on this observation, it was planned to find two different models for the motor to represent the behaviour of the motor to increasing and decreasing input torque profiles.

[8]This might be due to the hysteresis in the motor or the load cell.

Then, it was possible to split a given force profile into increasing and decreasing sections, and use the corresponding transfer function for each section, to determine the appropriate K_p, K_i, and K_d variables for the PID controller, as the motor runs over the entire force profile.

A few types of increasing and decreasing force profiles (the ramp and quarter sine curve) were chosen and by running a few tests, the response of the motor to them was determined. The input curves to the motor and the response of the motor to them are shown in Figure D.11. The slopes of these curves are carefully chosen to be in the same range as the slopes of the actual pianist finger force curves in Figure 2.14. Since the motor has a latency to reach its steady state response for the decreasing force profiles in Figure D.11, 30 ms were allowed to attain its steady state response. For the system identification process, the portions of these force profiles after t=30 ms are used. Because the motor has already reached the steady state response at this moment, and starts to respond to the decreasing force profile.

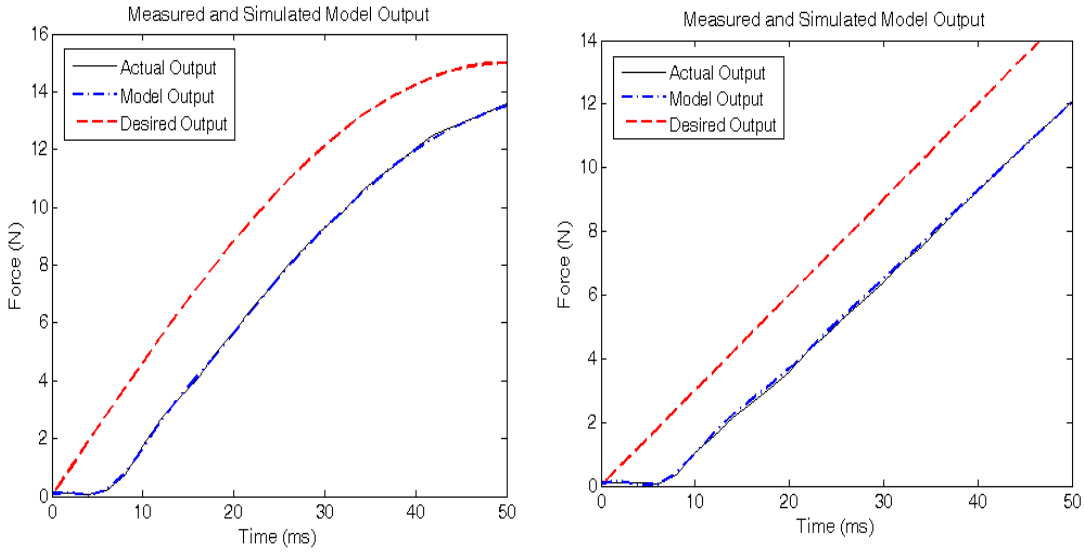

Figure D.12: Comparison between the Model and Actual Output for the Standard Ramp and Quarter-Sine Curves

Next, by using the data in Figure D.11 and the *process models* method, the response of

the system to the increasing and decreasing force profiles were identified and two third order transfer functions obtained. Three was the lowest order that predicted the behaviour of the system well for the increasing and decreasing force profiles. The values of the parameters of the transfer function, Equation (D.1), for the increasing force profiles are

$$K = 0.9267 \text{ Newton}, \quad T_w = 1.9800, \quad Zeta = 0.2496, \text{ and } \quad Tp_3 = 4.6276$$

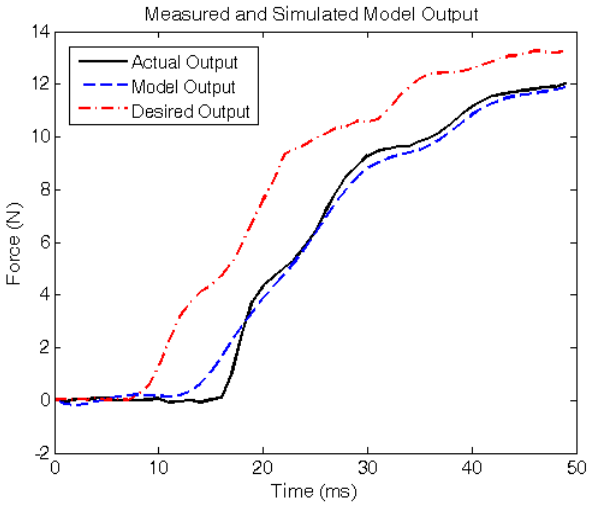

Figure D.13: Comparison between the Model and Actual Output for a Non-Standard Curve

Figure D.12 shows how well this transfer function predicts the behaviour of the system to the increasing ramp and quarter-sine profiles. Figure D.13 reflects a non-standard increasing force profile and the response that this model predicts for this.

The values of the parameters of the transfer function, Equation (D.1), for the decreasing force profiles are

$$K = 0.9407 \text{ Newton}, \quad T_w = 7.6406, \quad Zeta = 0.2569, \text{ and } \quad Tp_3 = 2.2222$$

Figure D.14 shows how well this transfer function predicts the behaviour of the system to the decreasing ramp and quarter-sine profiles. Figure D.15 exhibits a non-standard decreasing force profile and the response that this model predicts for that. According to

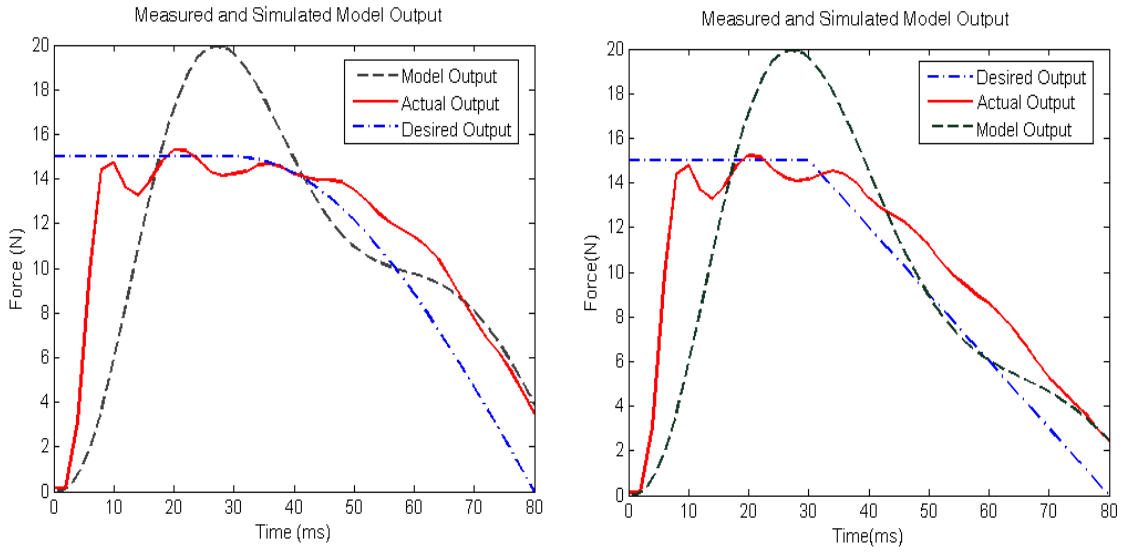

Figure D.14: Comparison between the Model and Actual Output for the Standard Ramp and Quarter-Sine Curves

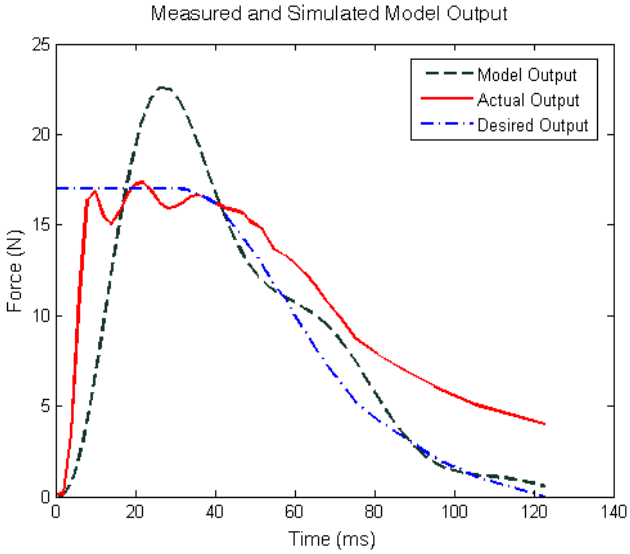

Figure D.15: Comparison between the Model and Actual Output for a Non-Standard Curve

these figures, it is obvious that the model does not predict the actual response of the system well.

Using two transfer functions, compared with having a single transfer function for both increasing and decreasing force profiles, did not increase the fidelity of the model in predicting the actual behaviour of the system, for a typical force profile that has both increasing and decreasing sections. Figure D.16 shows the result of using these two transfer functions to predict the actual response of the motor for a typical force profile. It can be seen that the performance of the transfer function for the increasing force profiles, at the increasing sections A and B of the force profile is fairly good. However, the performance of the transfer function for the decreasing force profiles, at the decreasing sections A and B of the force profile is discouraging.

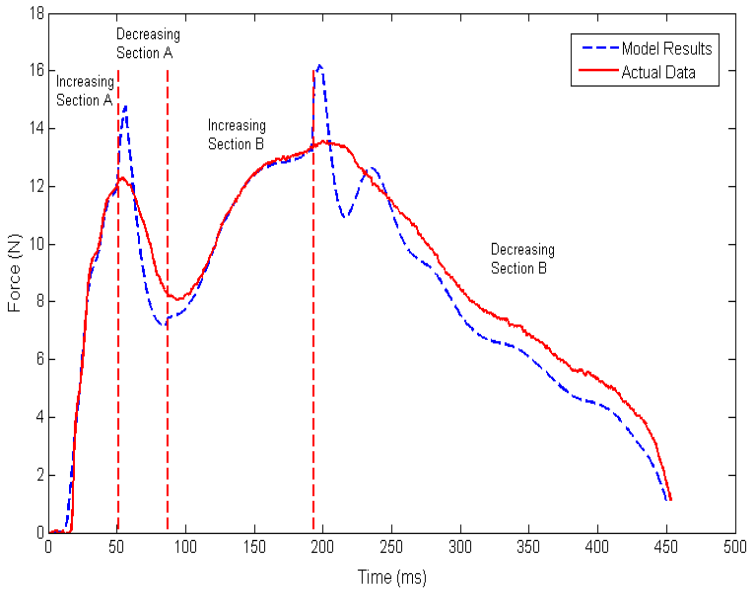

Figure D.16: Predicting the Actual Output of the Motor by Using Two Transfer Functions

Finally, regardless of a precise model for the system, using the *LabVIEW* software[9] a PID controller was established for the system. The feedback from the load cell was

[9]The *LabVIEW* software is a platform and development environment for a visual programming language from *National Instruments*. It is commonly used for data acquisition, instrument control, and industrial automation.

connected to the PID controller in the *LabVIEW*, and the controller output was sent to the motor drive. Some actual tests were accomplished by using this controller. Although many combinations of the different values for the K_p, K_i, and K_d parameters were tried, none of them resulted in a stable controller that improved the open-loop performance of the system. Based on these results, the feedforward method, along with a PID controller, was tried in the next step.

D.3 Feedforward plus PID Control

In the feedforward method, shown in Figure D.17, the desired output of the system is passed through the inverse transfer function of the system, and then, this result is fed through the system as the input. The performance of this method depends on the accuracy of the inverse transfer function of the system. To improve the performance of the system even further, a PID controller can be added to the system, as depicted in Figure D.18. If the feedforward section of the control loop works well, the PID controller can minimize the remaining errors from the feedforward part of the control loop.

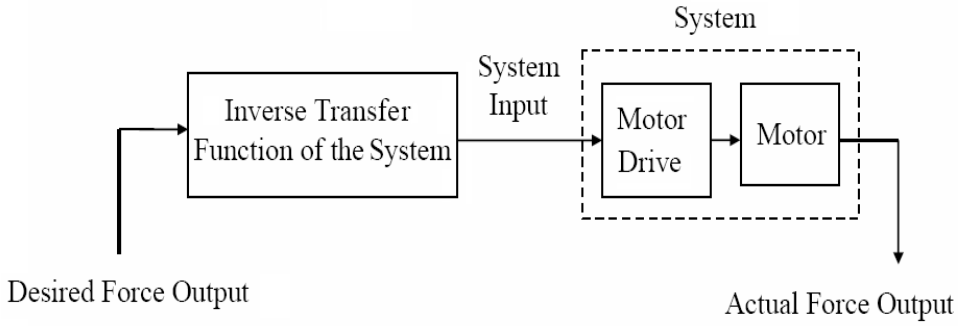

Figure D.17: Feedforward Method for Running the Motor

To find an inverse transfer function of the system, by using the *process models* method in the system identification toolbox of *MATLAB* and the two curves in Figure D.1, a reverse system identification (i.e., from the output to input) was done. The same third order transfer function given in Equation (D.1) with the following values for its parameters was obtained

$$K = 1.0770 \text{ Newton}, \quad T_w = 1611.7, \quad Zeta = 224.18, \text{ and } \quad Tp_3 = 0.0725$$

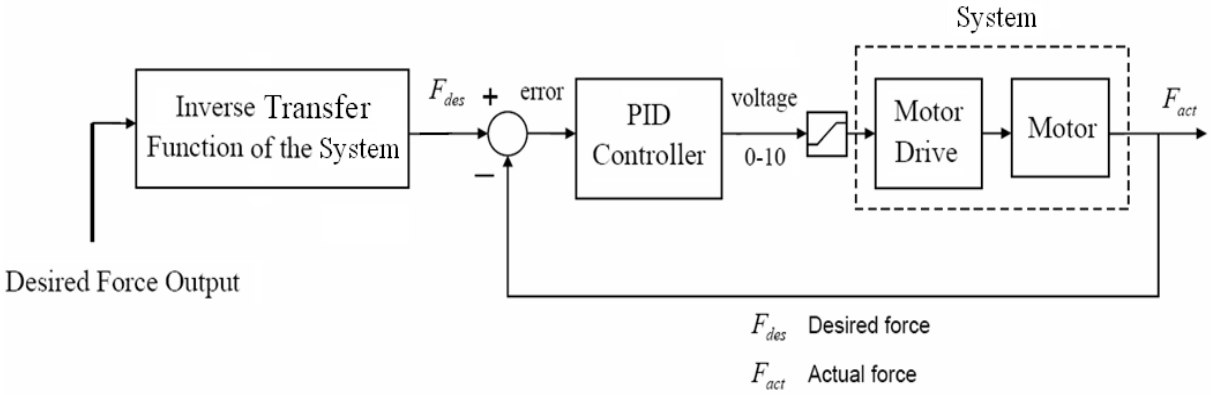

Figure D.18: Feedforward Method along with the PID Controller for Running the Motor

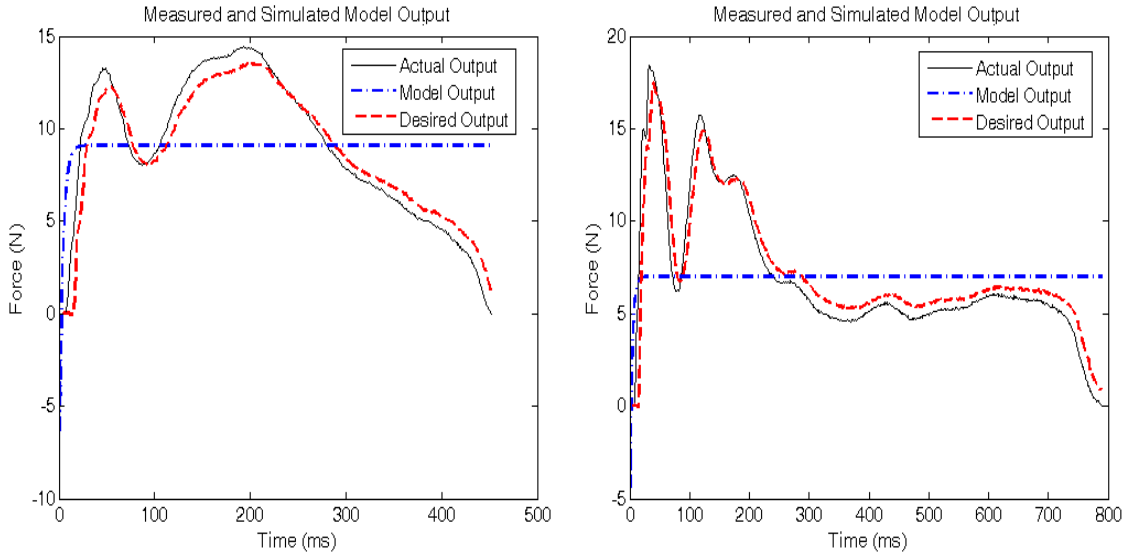

Figure D.19: Comparison between the Model and Actual Output

This inverse transfer function can closely predict the inverse response of the system for the force profiles in Figure D.1; however, as shown in Figure D.19, it cannot predict the

inverse response of the system to the typical pianist force profiles shown in Figure 2.14, well.

Since the inverse transfer functions did not even improve the open-loop performance of the system, it was pointless to add a PID controller to the system, as suggested in Figure D.18. Therefore, the feedforward method, along with a PID controller, was not incorporated.

D.4 Conclusions and Suggestions

The system is nonlinear, i.e., by analyzing only the response of the system as an impulse input, the transfer function of the system cannot be found. Even two separate transfer functions for the increasing and decreasing force profiles cannot predict the behaviour of the system, well. Two factors, the 0.67 N error in the load cell (according to the manufacturer specifications sheet) and the latency caused by the signal filtering, do not allow to reduce the error (i.e. the difference between the actual and desired force). None of the methods that were tested (the NN and linear controllers) could improve the open-loop performance of the system.

Based on these results, in the future, the efficiency of the non-linear control methods to control the torque output of the motor can be investigated. The other matter that can be tested is replacing the pianist finger force as the input to the piano model by the position of the last bone of the pianist finger. In this case, in the experimental setup, instead of controlling the torque output of the motor, the position of the motor shaft should be controlled. Controlling the position of the motor shaft might be easier than controlling the torque output of the motor. However, in this case an appropriate material representing the fingertip pulp should be attached to the motor arm and to complete the piano model, a precise model of the corresponding fingertip pulp should be added to the piano model. The reading from the key optical encoder should be used as the position feedback.